RICE UNIVERSITY

Evidence of Electron Impact Ionization in the Magnetic Pileup Boundary of Mars--Observations and Modeling Results

by

Dana H. Crider

A THESIS SUBMITTED
IN PARTIAL FULFILLMENT OF THE
REQUIREMENTS FOR THE DEGREE

Doctor of Philosophy

Approved, Thesis Committee:

_____
Paul A. Cloutier, Chair
Professor of Space Physics and Astronomy

_____
Richard A. Wolf
Professor of Space Physics and Astronomy

_____
Reginald J. Dufour
Professor of Space Physics and Astronomy

_____
Peter J. A. Nordlander
Professor of Physics

Houston, Texas
May, 1999

Evidence of Electron Impact Ionization in the Magnetic Pileup Boundary of Mars--Observations and Modeling Results

by

Dana Hurley Crider

Abstract

We analyze the solar wind interaction with Mars through examination of Mars Global Surveyor Magnetometer/Electron Reflectometer (MGS MAG/ER) data. We focus on data in the postshock, dayside plasma flow, especially the Magnetic Pileup Boundary (MPB.) First, we present the data to characterize the features of the MPB. Next, we argue the evidence that the MPB is formed through a series of processes, beginning with electron impact ionization of planetary neutrals in the exosphere of Mars. These new ions form an unstable population of energetic ions in the post-shock flow. Ion cyclotron waves are established to scatter the ion distribution into one more stable. This removes thermal pressure from the ions. In order to maintain a constant total pressure in the flow, the magnetic field intensifies, transferring the lost ion thermal pressure into magnetic energy.

Also, we develop a model of the electron impact ionization process in the martian exosphere. This model calculates the evolution of the electron distribution function as the flow encounters exospheric planetary neutrals. It reproduces the electron spectrum observed by the ER in the MPB very well. Therefore, we conclude that electron impact ionization is the process responsible for the onset of magnetic pileup in the postshock flow at Mars.

Acknowledgements

First, I'd like to express my appreciation to Paul Cloutier for being an excellent advisor. He has provided me with much guidance throughout the years in all aspects of my graduate work. I, especially, am grateful that he introduced me to all the facets of conducting scientific research, including being part of an active research group and science team. Of course, hard work is always rewarded by the Cloutier Annual Watersports Spectacular (and science meeting.)

I also owe a lot to Mario Acuña and Jack Connerney for supporting my work through a NASA Traineeship. Colin Law has been very generous with all of his help, support, games, and artistic abilities. Thanks to the MGS MAG/ER science team for many useful discussions, especially Mario Acuña, Dave Mitchell, Dave Brain, and Christian Mazelle. Thanks to Dave Mitchell and Mike Powell for supplying the data I used. Bernard Lindsay also provided pertinent information on atomic processes.

Umbe and Maria--you are such great friends. My entire experience at Rice would not even come close to being the same without you! Thanks to Norma, Big Bob, and the many incarnations of Little Bob at the lunchtime bridge and Scrabble group. You helped me keep a healthy perspective on life's priorities and a cheery outlook. Also, those yummy Tuesday cheesesteak sandwiches deserve a mention.

My parents and my in-laws have been great helps. Thank you for offering their eternal support and having unending patience. Without them, I would have never finished this work and retained my sanity! We'll celebrate at graduation. But most importantly, I thank my husband. Tony--you have always been there for me, even when I've been a bear or brain-dead. Especially, I thank you for giving us our Sundays. The Magic will always be there for us. (We might even have to step through the Portal now that we are Ph.D.'s.) Love forever.

Contents

1. Introduction

1.1 History of Mars Missions

Thirty-seven years since the beginning of Mars spacecraft missions, scientists had not found conclusive evidence of whether Mars has an intrinsic planetary magnetic field. In fact, the magnetic fields of all the planets except Pluto and Mars had been determined. Although Mars is close to Earth and has been the destination of many spacecraft, several missions to Mars were short-lived, produced inconclusive results, or did not carry the appropriate instrumentation for detecting magnetic fields. Since the first attempt to send a probe to Mars by the Soviets in 1960, there have been 29 (through the 1996 launches) attempts [*NSSDC*, 1998; *Snyder and Moroz*, 1992]. A summary of attempted missions by decade appears in figure 1.1. Figure 1.2 presents the degree of success of the missions, by decade. Only nine successfully completed their missions, with one still pending. Three others did not achieve their missions, but had limited success. It was the pair of American spacecraft launched to Mars in late 1996, namely Mars Pathfinder and Mars Global Surveyor, that finally reversed the luck of Mars missions. Table 1.1 lists a summary of some relevant Mars missions.

Initial studies of the Mars space environment consisted of radio occultation experiments [*Kliore et al.*, 1972] and/or primitive *in situ* experiments placed on fly-by trajectories, *e.g.* Mariners 4, 6, and 7 [*NSSDC* 64-00942; *NSSDC* 69-014A; *NSSDC* 69-030A]. The next step was to insert a spacecraft into martian orbit. The Russian spacecraft series, Mars 2, 3, and 5, accomplished that and increased the cumulative bow shock crossing database with their orbital missions in the early 1970's [*NSSDC* 71-045A; *NSSDC* 71-049A; *NSSDC* 73-049A]. However, these spacecraft did not approach close enough to the planet to detect

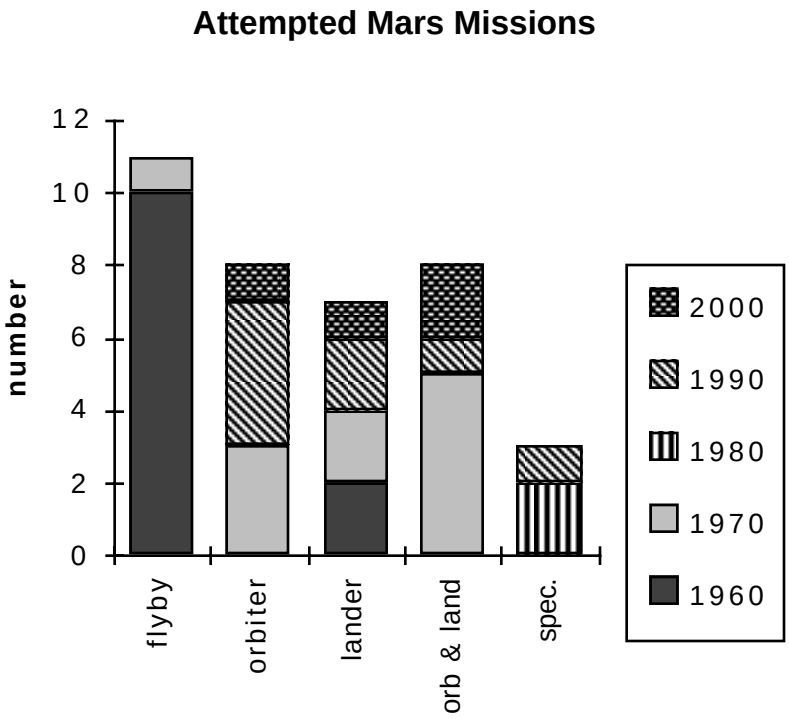

Figure 1.1. Attempted Mars mission type by decade. Early on, most Mars missions were flybys. As technology progressed, orbiters and landers replaced the flyby mission.

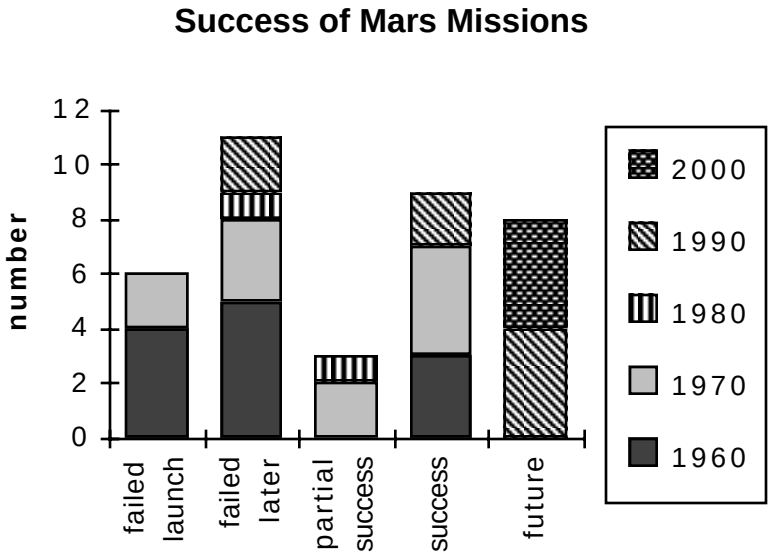

Figure 1.2. Degree of success of Mars missions by decade. Failures outnumber successes by far. Success seems to be evenly distributed by decade and seems proportional to number of trials.

Mars Spacecraft Missions Summary

Selected Spacecraft	Date	Closest Approach	Instrumentation					
		(km)	*magnetic fields*	*electron density*	*ion comp-position*	*plasma waves*	*e-/ion temp.*	*neutral density*
Mariner 4	Jul 65	9846	yes	yes	x	x	x	x
Viking 1	Aug 75	surface	x	yes	yes	x	yes	yes
Viking 2	Sep 75	surface	x	yes	yes	x	yes	yes
Mars 2	Nov 71-May 72	1380	yes	yes	yes	x	yes	x
Mars 3	Dec 71-May 72	1100	yes	yes	yes	x	yes	x
Mars 5	Feb 74	1300	yes	yes	yes	x	yes	x
Phobos 2	Feb 89-Mar 89	860	yes	yes	yes	yes	yes	x
Mars Observer	DOA (Aug 93)	pre-insertion	yes	yes	x	x	yes	x
Mars Global Surveyor	Sep 97-?	~100	yes	yes	x	x	yes	x
Mars 96	(Nov 96)	Earth orb.	yes	yes	yes	yes	yes	yes

Table 1.1. Summary of some relevant Mars missions.

the presence of an intrinsic magnetic field, if Mars had one. In 1975, the two Viking landers successfully descended to the Martian surface. The Vikings each measured ionospheric and atmospheric properties during the descent, but they were not equipped with magnetometers to detect a planetary magnetic field [*Hanson et al.*, 1977].

After a hiatus of over a decade, the Russians returned to Mars orbit with Phobos 2 (see *Zakharov* [1992] for a summary.) In its first four elliptical orbits, Phobos 2 reached as low as 860 km altitude. After four passes, the orbit was circularized at the distance of Mars' moon Phobos. Although the spacecraft did not enter the ionosphere of Mars, its data was very valuable. Phobos 2 was also lost prematurely after over one month in orbit.

The next attempts to Mars were also plagued with misfortune. NASA's Mars Observer lost contact prior to insertion into Mars orbit in 1993 [*Travis*, 1993]. The Russian Mars 94 spacecraft suffered from many delays. In fact, problems with the spacecraft persisted, delaying delivery until just before the

1996 launch deadline. Unfortunately, Mars 96 still was unable to make it out of Earth orbit. The booster misfired on an attempted burn. The spacecraft reentered the atmosphere, incinerated, and crashed in the Pacific Ocean [*James,* 1997].

Fortunately, the two NASA spacecraft in the 1996 launch window were both successful. Mars Pathfinder was launched from Cape Canaveral on December 7, 1996 and landed on Mars July 4, 1997 [*Golombek et al.*, 1997]. Although it had no particles and fields experiments, it investigated the magnetic nature of airborne dust and found the dust to be very magnetic [*Hviid et al*., 1997]. Mars Global Surveyor (MGS) was launched November 4, 1996 and reached Mars September 11, 1997 [*Albee et al.*, 1998]. Immediately, MGS answered the question about the intrinsic Martian magnetic field. There is no significant planet-wide magnetic field at Mars; instead, there is a patchy remanent field in the crust [*Acuña et al.*, 1998]. MGS attained its circular mapping orbit at 378 km in March 1999 after a period of aerobraking and phasing orbits. In this work, we use data from MGS to further investigate the magnetic environment of Mars induced by its interaction with the solar wind.

1.2 Studying Solar Wind Interactions

The solar wind is a supersonic, super-Alfvenic plasma flow [*Parker*, 1958]. As the flow encounters an obstacle, it must be diverted. A bow shock forms upstream of the obstacle. As the flow passes through the shock front, the parameters of the flow change abruptly. The shocked plasma is slower, denser and hotter than the unshocked plasma. The resulting plasma environment produced by the combination of the solar wind and the obstacle depends on the nature of the obstacle. In addition, the environment will evolve with changing solar wind conditions.

This near-planet plasma environment produced by the interaction plays an important part in several processes of interest. For example, every mission is affected by the space environment the spacecraft encounters [*Hastings and Garrett*, 1996]. The plasma environment determines spacecraft charging, affects instrument measurements, and reduces some materials' integrity. Therefore, it is essential for the proper functioning of a spacecraft that the basics of its local plasma environments are understood. For this reason, the communications industry and military both support the study of the Earth's interaction with the solar wind to protect their investments in Earth orbiting satellites.

Also, the structure of magnetic fields near a planet is affected by the planet's interaction with the solar wind. The magnetic field, in turn, affects the motion of charged particles. Studying solar wind interactions gives vital information about where charged particles can easily penetrate into the atmosphere, or for bodies lacking a thick atmosphere, penetrate to the surface. This, in turn, increases our ability to properly shield astronauts from radiation.

Another tangible benefit of studying solar wind interactions is that it progresses numerical modeling techniques to handle more complicated sets of coupled differential equations in three dimensions. Adding electric and magnetic fields to the gas dynamic problems of fluid mechanics stretches the limits of computational methods developed for those purposes. Many groups, like Spreiter and Stahara, the Rice University group, and the University of Michigan group, have expanded the frontiers of computational physics with their solar wind interaction codes [*e.g. Spreiter et al.*, 1970; *Harel et al.*, 1981; *Bauske et al.*, 1998; etc.].

Some of the most important scientific discoveries are ones that are not predicted. For the magnetometer (MAG) experiment on MGS, there are already several exciting results that either the instrument was not specifically intended to

find or the experts in the field could not have predicted. For example, at a magnetometer team meeting during MGS's first periapsis pass around Mars, Mario Acuña, the principal investigator of the instrument, held a contest to see who in the team could come closest to predicting the highest magnetic field that the spacecraft measured. Predictions fell mostly in the range of 25-100 nT, but ranged from 8 nT to 250 nT. Some scientists scoffed at predictions that were severe outliers. The highest prediction of 250 nT was made by the principal investigator who did not really think it was possible, but wanted to test the full range of the instrument. The results came in and the answer was 65 nT. However, over the course of the next several weeks, it became obvious that anyone in the room could have been correct on another day. There was an orbit in which the maximum field measured was almost 400 nT, when the spacecraft passed over its first magnetic anomaly! There was also an orbit where the field did not exceed 15 nT when the IMF was particularly low. So although the instrument was designed to map out crustal magnetic fields, even the experts in the field were surprised by the results. The work done in this thesis will discuss many results that were not in the original scope of the proposed research for the instrument.

1.3 Mars' Place in the Solar Wind Interaction Spectrum

Though we have demonstrated some of the benefits of studying solar wind interactions, why does one study the solar wind interaction with Mars in particular? First of all, as mentioned in section 1.1, studies of Mars lag behind those of other solar system objects due to a lack of data. Here, we attempt to bring the knowledge of Mars up to the same level as Earth's other near neighbors. Second, Mars is one of a few obstacles to the solar wind that lacks a strong intrinsic magnetic field. Due to the rarity of this class of object, we study

Mars because it is one of the few available "laboratories" equipped for such studies.

Another reason to study the solar wind interaction with Mars is that it is a prime candidate for human exploration. Besides the Moon, only Mars has both a climate tolerable to humans and the proximity required by the current level of technology. Present materials are incapable of withstanding the enormous heat and pressure of the atmosphere of Venus for extended periods of time. Some moons of the outer planets might have tolerable climates, but are infeasibly far away for manned missions. Mars is cold, but not too cold for materials to last and function for a many years. NASA has been investigating facets of human missions to Mars for decades. However, no mission has been approved for post-conceptual development. In preparation for human exploration of Mars, we study the space environment of Mars. The communications relays that are needed for constant contact must be designed for reliable performance in the Mars space environment. Likewise, spacecraft charging conditions need to be understood in order for safe rendezvous in Mars orbit. In addition, understanding the patchy magnetic field on the surface of Mars gives pertinent information about radiation shielding for astronauts on Mars. Therefore, studying the space environment and the solar wind interaction with Mars contributes valuable knowledge that can be utilized when planning for human exploration of Mars.

1.4 Goals of Research

In this thesis, we investigate the physics that results in a special feature of the solar wind interaction with Mars. The Magnetic Pileup Boundary (MPB) is detected in the data on most orbits. We analyze this data to get an understanding of the form of the boundary. Then, we infer the physical processes responsible for the formation of the boundary. Constructing a model

using the physics, we attempt to reproduce the observations. Upon success, we discuss the implications of the physics of the MPB to the martian environment. Further, we suggest how our work can be used to confront other Mars models.

2. The Solar Wind Interaction with Non-magnetic, Conducting Obstacles

First of all, we must outline the solar wind interaction with this class of obstacle. We begin describing it in general with a global perspective. We explain the macroscopic form of an interaction of the solar wind with a conducting body. Then, we enumerate the microprocesses that become important. Afterwards, we introduce the features encountered in the high mass (Venus-like) limit of this class of interactions. Similarly, we describe the special effects caused by the low mass (comet-like) limit of obstacle in the interaction. Mars, having an intermediate mass, exhibits some features of both extremes.

2.1 Description of the Solar Wind Interaction

Unlike the Earth, objects in this class have no global magnetic field capable of withstanding the solar wind pressure. However, unlike moon-like objects, which also lack a significant intrinsic magnetic field, these objects do have conducting ionospheres substantial enough to generate and sustain electrical currents. Therefore, in this type of interaction, it is the conducting ionosphere that acts as the obstacle to the supersonic solar wind. The ensuing discussion describes the interaction as it follows the flow of the solar wind past the obstacle as displayed in figure 2.1.

As the supersonic solar wind encounters the obstacle, it must be slowed to subsonic speeds so that the flow can be diverted. A bow shock forms upstream of the obstacle. In figure 2.1, the bow shock is the thick dashed line labeled "bow shock." Notice in figure 2.1 that upstream of the bow shock, the solar wind is unaffected. Magnetic field lines are not changed until they reach the shock. However, inside the bow shock, all of the flow parameters are greatly modified. As the flow reaches the bow shock, it is slowed, heated, and compressed.

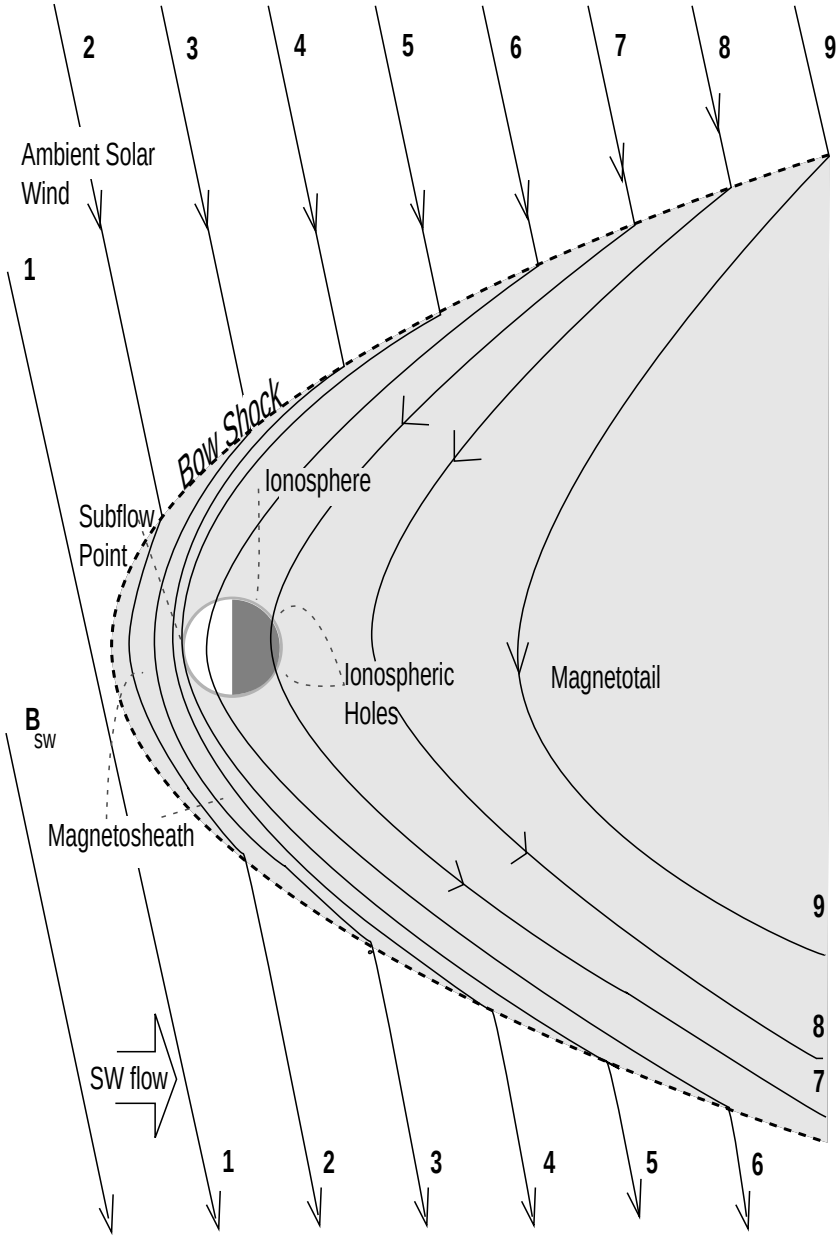

Figure 2.1. Cartoon of the solar wind interaction with a non-magnetic conducting obstacle. The figure shows a time series of what happens to a magnetic field line in the solar wind as it passes the obstacle. The regions of interest are labeled.

There is a magnetic field accompanying the solar wind plasma impinging on the obstacle. Because a conductor, like the ionosphere, wants to exclude an external magnetic field, currents flow in the ionosphere and along the shock to prevent the magnetic field from penetrating the conducting ionosphere. The sense of the currents is to produce a magnetic field to cancel the external

magnetic field inside the conductor. Outside of the conductor, however, the magnetic field is amplified. This produces a draping of the Interplanetary Magnetic Field (IMF) around the planetary body as is shown in the magnetosheath in figure 2.1, lines 2-4. The draping can also be explained from the perspective of considering the magnetic field to be tied to the plasma. As the solar wind velocity slows in front of the planetary body, the motion of the magnetic field lines also retards. But because the field lines are continuous through the bow shock, the part of the field line outside of the shock continues to fly past at the solar wind speed. The resulting geometry is a draping of the magnetic field proportional to the change in local flow speed. In figure 2.1, the closer to the nose of the planet one looks, the slower the bulk plasma velocity is and the more the magnetic field piles up.

If the ionosphere were a perfect conductor, it would completely prohibit the IMF from penetrating the ionosphere. *Spreiter and Stahara* [1992; 1980; *Spreiter et al.*, 1970] have modeled the velocity, pressure, temperature, density and magnetic field within the bow shock for the case of a hard obstacle. Their results fit the observations in the magnetosheath very well for Venus and Mars. Figure 2.2a shows the Spreiter and Stahara results for contours of density and figure 2.2b for contours of velocity and temperature. Their results are the standard to which other work is compared. However, the real objects are not perfect conductors and this effect is not included in the magnetosheath model. Due to their finite conductivity, a small amount of the field permeates the ionosphere and influences the dynamics of the region. It is through the small fraction of IMF that enters the ionosphere that the solar wind's momentum is transferred to the planetary body. Therefore, it is important that we learn the physics of the interaction in the ionosphere in order to understand the mechanisms of momentum transfer.

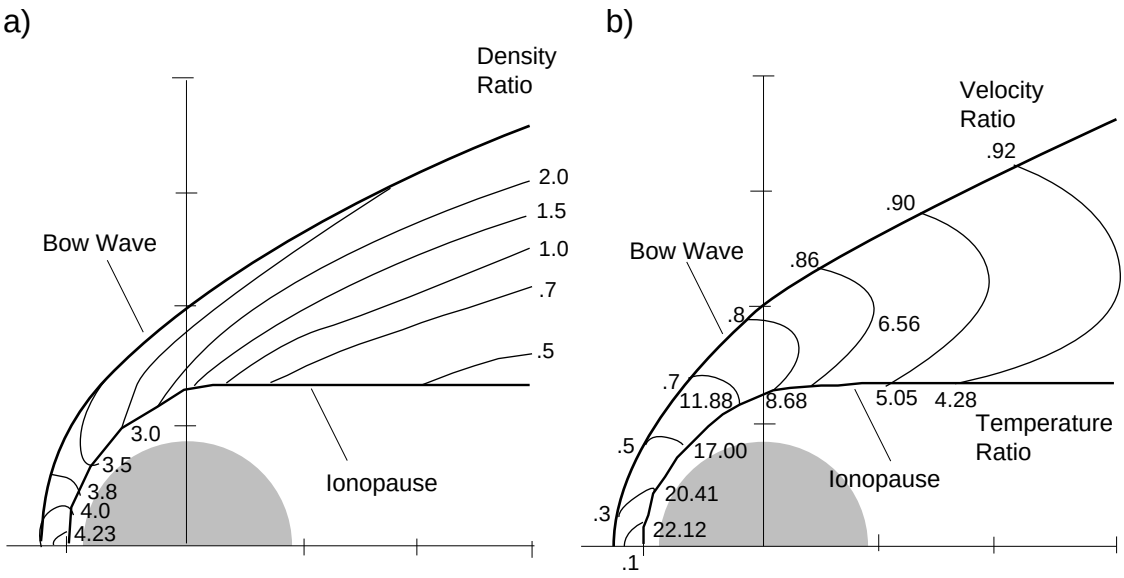

Figure 2.2 (from *Spreiter et al.*, 1970). Contours of a) density and b) temperature (bottom) and velocity (top) in the magnetosheath of a Venus-like solar wind interaction. The numbers give the ratio of the value to the upstream, pre-shock solar wind value calculated from the *Spreiter et al.* [1970] model. In the model, the ionopause is a hard obstacle to flow.

The planetary ionosphere (or cometary coma) consists of heavier ions that are born from photoionization of planetary neutrals and subsequent atmospheric chemistry. At Venus and Mars, the primary ionospheric constituents are O^+, O_2^+ and CO_2^+ [*Nagy et al.*, 1990; *Shinigawa and Cravens*, 1989; *Ip*, 1988; *Kim et al.*, 1998]. For comets, the water group ions prevail [*Reinhard*, 1986; *Krankowsky et al.*, 1986]. In all cases, the ions are far heavier and slower than the solar wind ions, which are mostly protons. The boundary at the top of the ionosphere is called the ionopause. It is defined as the region where the ion scale height turns from the steep gradient observed at onset to the typical ionospheric scale height. At the same location, the magnetic field rotates to align itself with the local day to night flow direction [Law and Cloutier, 1995]. The exobase defines where the ionospheric scale height equals the mean free path. Below the exobase, collisions begin to dominate.

In a Chapman layer ionosphere [*Chapman*, 1931], electron density increases until the optical depth of photoionizing photons reaches unity. For Mars and Venus, CO_2 is the main atmospheric constituent at low altitudes. Also present are atomic oxygen neutrals. Both species have ionization potentials very near to each other, 13.77 and 13.6 eV, respectively. Therefore, there is only one Chapman peak in these ionospheres in contrast to Earth, which has several layers. So, the point within the ionosphere that the optical depth for ionizing photons is unity is defined as the ionospheric main peak. Below the main peak, the photoionization rate begins to decrease.

As the flow carrying the magnetic field enters the planetary ionosphere, it is slowed further. Therefore, the magnetic field lines bend as their different portions enter the ionosphere. This effect was discovered by *Law and Cloutier* [1995; 1997.] Figure 2.3 shows the progress of the field line labeled "5" in figure 2.1 once it first makes contact with the ionosphere. As this field line becomes successively more imbedded in the ionosphere, it bends into the pattern given in figure 2.3. One important property displayed here is that the magnetic field begins rotating at the ionopause. Another interesting point is that the magnetic field tends to align itself with the local day to night flow direction within the ionosphere. For a more detailed discussion of this, see *Law* [1995] and *Law and Cloutier* [1997].

As the solar wind passes the obstacle, the flow is reaccelerated. The field lines that enter the ionosphere are pulled around to the nightside and are released from the planet. In figure 2.1, the line labeled "7" is the last line to be contact with the ionosphere. It has the characteristic of being primarily radial at the ionopause, in contrast to the magnetic field lines being mostly horizontal elsewhere within the ionosphere [*Marubashi et al.*, 1985]. By the time the field lines pass by the obstacle, the portion of the field line outside of the bow shock

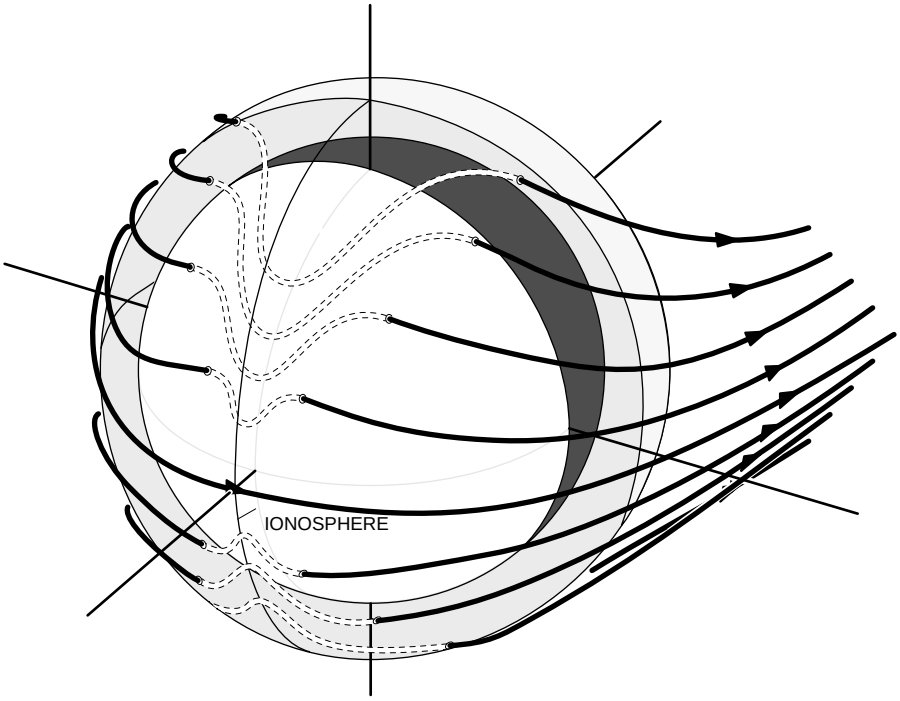

Figure 2.3 (from *Law*, 1995). The weathervaning of magnetic field lines in the ionosphere. The progress of a field line over or under the obstacle is shown. As the field line becomes more imbedded in the ionosphere, the degree of weathervaning increases.

has moved considerably down range. The stretching of the field lines is evident in the magnetotail region of figure 2.1 in field lines 5-8. However, as the lines pass the obstacle, magnetic tension pulls on the straggling parts and accelerates them far down the tail. Eventually, the field lines straighten out, leaving little evidence of the interaction upstream.

2.2 Nuances of the Interaction

Generally, the time evolution enumerated above is a valid description of the interaction. In reality, however, there are other factors. For example, mass loading of the plasma flow occurs, in which the solar wind picks up heavy planetary ions as it passes the obstacle. Planetary neutrals are ionized by

several mechanisms. The dominant processes are photoionization, electron impact ionization, and charge exchange.

Photoionization (PI) occurs when a solar UV photon with energy greater than the neutral's ionization potential hits the neutral. The photon kicks off an electron from the particle. The resulting ion approximately retains its initial momentum. The electron has the energy equal to the photon energy, $h\nu$, less the ionization potential, χ_A. The reaction and energy go as:

$$A + h\nu \rightarrow A^+ + e^-$$
$$E_{e^-} = h\nu - \chi_A$$

with A as an arbitrary neutral particle, and h as Planck's constant. The reaction rate of this process is proportional to the cross section of the reaction and the ionizing flux. The photoionizing flux drops as r^{-2}, thus the photoionization rate scales as inverse square of solar distance from object to object. The rates used here are scaled from those given for 1 A.U. in *Banks and Kockarts* [1973].

Electron Impact Ionization (EII) is the process in which an energetic electron impacts a neutral and ionizes it. The reaction goes as:

$$A + e_i^- \rightarrow A^+ + e_i^- + e_e^-$$
$$E_{e_i^-} + E_{e_e^-} = E_o - \chi_A$$

where the energy of the incident electron distributes itself between the ionization potential of the neutral and the resulting kinetic energy of both the incident and emitted electrons. Laboratory measurements indicate that the typical energy distribution between electrons is one-sided [*Shyn*, 1992]. The secondary electron is under 15 eV 72% of the time for an incident electron of 100 eV. For a 250 eV incident particle, the secondary electron has under 15 eV 69% of the time. The reaction rate for this reaction is calculated by integrating the product of the flux of incident electron and the energy dependent cross section for the reaction over all relative velocities:

$$\nu_{ei} = \int_0^\infty (v\, f(v)\, \sigma(v))\, 4\pi v^2 dv$$

where v is the relative velocity, $f(v)$ is the distribution function of the electrons, and $\sigma(v)$ is the cross section. The integral assumes spherical symmetry in velocities. The cross sections are dependent on the relative velocity of reactants and are taken from the experimental values of *Thompson et al.* [1995] for oxygen, *Shah et al.* [1987] for hydrogen, and *Straub et al.* [1996] for carbon dioxide.

Charge exchange (CE) is a process in which an electron is stripped from a neutral by a passing ion. The net effect is the neutral becomes ionized and the ion is neutralized, but both particles retain their momenta. In the magnetosheath, this is an interesting process because the solar wind ions are faster moving and less massive relative to the planetary neutrals. As charge exchange occurs, the ion population becomes heavier and slower. The reactions occur as:

$$A^+ + B \rightarrow A + B^+$$

The reaction rate comes from the convolution of the incident ion flux and the energy dependent cross section for the reaction. *Stebbings et al.* [1964] and *Lindsay et al.* [1996] measure charge exchange cross sections for protons with O. Although charge exchange between protons and neutral H does not change the mass of the flow, we consider this reaction as well due to the change in momentum to the flow. The $H^+ + H$ cross sections are from *Banks and Kockarts* [1973].

Regardless of how it forms, a newborn planetary ion is suddenly very hot with respect to the incident flow. The planetary neutrals are relatively slow moving in the planetary frame of reference. However, in the co-moving solar wind frame, the newborn ion has a large velocity perpendicular to the magnetic field. In the solar wind frame, the ion will begin to gyrate around the magnetic

field lines with a radius proportional to the local solar wind speed. In the planetary rest frame, the ion begins to **E** x **B** drift with a large radius of curvature. After only a few gyration radii, the ion has completely cleared the obstacle and is assimilated into the flow. The momentum of the flow residing in the new ion is much larger than average. Therefore, after accumulating many ions "picked-up" in this way, the flow as a whole must slow down to conserve momentum.

Related to the mass loading issue, upstream of the ionosphere, populations of superthermal planetary ions are sometimes seen. At times, these are in discrete "clouds" [*Brace et al.*, 1982]. The presence of such a plasma affects the details of the interaction. Magnetic field rotations, like those observed at the ionopause, are detected at cloud boundaries [*Law*, 1995]. These clouds detach and are ejected down the ionotail. At comets, it is a continual process of mass loss over a large distance.

Another complexity arises because the solar wind is not in steady state. Because the solar wind can remain relatively steady for periapsis pass, one can often treat the solar wind as a steady source for statistical analyses and in some other applications. However, variations in the solar wind parameters are reflected in the interaction as the changes propagate through the system. Therefore, it is extremely important to always consider an unsteady solar wind as the cause for features observed in the data.

Finally, waves are prevalent in the interaction, but have been neglected in the discussion above. Wave activity increases upstream of the bow shock [*e.g. Sagdeev et al.*, 1986; *Russell et al.*, 1990] and continues to varying degrees in all regions of figure 2.1. Virtually every plasma instability and every wave mode can be detected somewhere in the interaction between the solar wind and these objects. As the IMF orientation, solar wind pressure, solar EUV flux, and outgassing rates change, new configurations occur and give rise to new wave

modes. Therefore, these interactions provide a plethora of data for those interested in instabilities and waves (see [*Tsurutani*, 1991]). An in depth description of the waves and their functions as seen by MGS is presented in chapters 4 and 5.

The above exposition introduces some of the fine points of the solar wind interaction with a non-magnetic, conducting obstacle. Coupled with the general description in section 2.1, these sections provide a overview of this brand of solar wind interaction. However, the specifics of the interaction vary depending on the properties of the obstacle, *e.g.* its mass, atmosphere, and distance from the Sun. The following sections present the differences of the solar wind interaction in certain extremes. Venus represents the high mass, high solar wind pressure case. Comets, in contrast, have a low mass and a varying distance from the Sun.

2.3 Venus--The High Mass Limit

More is known about the solar wind interaction with Venus than with Mars or comets due to the volume of particles and fields data acquired by the Pioneer Venus Orbiter (PVO) mission [*Colin*, 1980]. PVO was in orbit around Venus for 14 years. For studies of the solar wind interaction, the spacecraft was equipped with a magnetometer, electric field detector, plasma analyzer, ion mass spectrometer, Langmuir probe, retarding potential analyzer, neutral mass spectrometer, and radio science investigation. Most of the conventional knowledge described above are a direct result from this mission. For a review of the results, see the paper by *Russell* [1992]. We now focus on a few issues that are specific to the solar wind interaction with Venus.

Many characteristics specific to the solar wind interaction with Venus result from the planet's high gravity. One such effect is that the atmospheric

scale heights are reduced. The scale height is defined as the e-folding altitude of a quantity like pressure or density. For example, in an isothermal atmosphere, the gas pressure as a function of altitude, h, can be expressed by:

$$p = p_o \exp\left(-\frac{mgh}{kT}\right)$$

where p is the pressure, p_o is a constant, m the mass of the species, g is the gravitational acceleration, k is Boltzmann's constant, and T is the temperature. One can define the scale height, $H \equiv \frac{mg}{kT}$, leaving the pressure as:

$$p = p_o \exp\left(-\frac{h}{H}\right)$$

Higher gravity reduces the scale height.

A smaller scale height produces several effects. First of all, boundaries that depend on density or pressure appear sharper than they would with larger scale heights. For example, the thickness of the ionopause is typically on the order of the O^+ scale height. At Venus, this tranlates into a well defined, distinct boundary. Second, the atmosphere does not extend out as far as it would if gravity were reduced. The exospheric population, though containing more atoms than at, *e.g.*, a comet is held to lower altitudes. Essentially, the planet is better equipped to retain its atmosphere. Therefore, in the magnetosheath and upstream of the bow shock at Venus, there are not many planetary particles. Third, Venus has enough gravity to retain a substantial ionosphere, even on the nightside. As a whole, the ionosphere can be considered to be gravitationally bound to the planet. Although some atmospheric escape does occur, it is not visibly obvious like at a comet.

2.4 Comets--The Low Mass Limit

Now we turn to the specifics of the solar wind interaction with a comet. For a good review, see the paper by *Coates* [1997]. As a comet moves inside of

~5 A.U., sublimation produces a supply of neutrals flowing outward from the nucleus. The outflow is estimated to be around 1 km/s [*Krankowsky et al.*, 1986]. Solar UV photons ionize the gas. But this happens over a large distance, around 10^6 km. The ionized particles mass load the solar wind flow, forming a bow shock upstream. This shock is usually a weak shock, although some data indicate the shock is more of a shock wave than a standing discontinuity [*Smith et al.*, 1986]. Inside the bow shock the cometary material continues to mass load the flow.

Interior to the bow shock is the magnetic pile-up boundary (MPB). The MPB was first identified in Comet Halley[*Neubauer et al.*, 1986] by a tangential discontinuity in the Giotto magnetometer data. The discontinuity was detected at a position of 1.35×10^5 km above the nucleus, both inbound and outbound. This feature was seen strongly in the inbound pass. Presumably the boundary in the outbound pass was weak due to the changed orientation of the shock to the magnetic field [*Neubauer et al.*, 1986]. This feature was not seen by other spacecraft at Halley because they did not cross close enough to the comet to reach the boundary. Only Giotto was close enough to see this. Giotto continued on to see the MPB again as it encountered comet Grigg-Skjellerup.

In association with the magnetic signature, the Johnstone Plasma Analyzer detected a sharp drop in electron fluxes. The 80-300 eV fluxes dropped by 25% very abruptly [*Mazelle et. al.*, 1989]. A smooth decline in 10-40 eV electron fluxes of about 30% was also observed. However, inspecting the pressure tensor, the plasma pressure stayed constant in the direction parallel to the mean magnetic field. The electrons cooled in the perpendicular direction across the boundary. The electron fluxes never recover to their pre-MPB values after the boundary [*d'Uston et al.*, 1989]. *Glassmeier et al.* [1993] found a change in the nature of ultra-low frequency waves in conjunction with the MPB.

Whereas upstream of the MPB, the magnetic field and electron density variations are correlated, downstream, they are anti-correlated.

The magnetic cavity is the inner region of a comet into which the magnetic field does not penetrate. This is the object boundary to the interaction. Only Giotto came close enough to penetrate the magnetic cavity. It crossed the contact surface at a distance of ~4600 km from the nucleus [*Neubauer et al.*, 1986].

As the flow passes the comet, large amounts of the cometary plasma and particles are swept back and carried out down the tail. Observations indicate that portions of the tail detach and escape, especially in conjunction with changes in the IMF direction.

Although many telescopic observations of comets have been made, only a few flyby spacecraft missions provide the limited *in situ* data for the solar wind interaction with a comet. The first comet spacecraft encounter was the ICE experiment, which flew through the tail of comet Giacobini-Zinner on Sept. 11, 1985. This was followed by the international armada to Halley in 1986. Giotto crossed in front of Halley on March 13, 1986 at 610 km minimum altitude [*Reinhard*, 1986]. The two Vega spacecraft passed on the order of 8000 km in front of Halley separated in time by 3 days [*Sagdeev et al.*, 1986]. Suisei and Sakigake, the Japanese contributions, probed the far reaches of the solar wind interaction with a comet at distances of 151,000 and 7×10^6 km, respectively on March 8 and 11 [*Hirao and Itoh*, 1986]. After the Halley encounter, Giotto continued to pass comet Grigg-Skjellerup in 1992.

3. Mars Global Surveyor

The MGS spacecraft is equipped with several instruments to be used in the primary Mars mapping mission: Mars Orbital Camera; Thermal Emission Spectrometer; Mars Orbital Laser Altimeter; Radio Science Experiment; and Magnetometer/Electron Reflectometer (MAG/ER). In this work, we look at only the MAG/ER data. The Magnetometer and Electron Reflectometer instrument complement provides a wealth of information on the plasma environment around Mars. And due to the varying orbits of the spacecraft, MAG/ER is able to sample most local times and solar zenith angles. Below are descriptions of the instruments and their capabilities, the spacecraft orbit, and the data available. A more detailed description of the MAG/ER exists in *Acuña et al.* [1992].

3.1 The Magnetometer

The Magnetometer experiment consists of twin triaxial flux-gate magnetometers. The instrument has a full scale dynamic range of ±4 nT to ±65,536 nT. The automatic range finder selects the optimum range for the instrument to operate in as the ambient magnetic field changes. MAG has a 12 bit digital resolution of the magnetic field [*Acuña et al.*, 1998].

The MAGs sample the magnetic field at a rate of 32 samples/s. The resolution of the data that is returned depends on the assigned telemetry rate. In the highest telemetry rate, the full 32 samples/s can be relayed. In this case, the data is formatted as a 12 bit average and a series of 6 bit difference fields, which can be added to the average field to regain the measurement. The high data rate is used in the time closest to periapsis. Using the best resolution is essential when doing a wave analysis of high frequency waves. However, the size of a data file containing the full detailed data is enormous. Analyzing this data when

the high time resolution is not required is quite cumbersome. Therefore, most of the data used for other purposes neglects the difference data and is averaged to 2/3, 1/3 or 1/6 samples/s.

The MAGs are positioned on the ends of the solar arrays of MGS [*Acuña et al.*, 1998.] Because they are not magnetically isolated from the spacecraft, the spacecraft field must be known and subtracted from the data. This is the primary source of uncertainty in the data. The spacecraft field is on the order of 3 nT. This spacecraft field is determined for the spacecraft's nominal configuration to within .5 nT. In comparison, the estimated instrument noise is around .006 nT [*Acuña et al.*, 1992]. Further complications and errors arise due to the positioning of the solar arrays during aerobraking which increases the error, as discussed below.

3.2 The Electron Reflectometer

The Electron Reflectometer is based on the symmetric hemispheric electrostatic analyzer. It has a field of view of 360° in a plane with 1.4° of resolution [*Acuña et al.* 1992; 1998; *Larson* 1993.] The out of plane coverage is a ±7° field. The instrument sweeps through a series of steps in voltage, selecting out different electron energies in the range of 10 eV to 20 keV. The electron flux at the selected energy is then recorded as a function of angle. In addition, the ER can operate in a Langmuir probe mode. The instrument sweeps through ± 10 V and uses the case as a swept bias collector. The Langmuir probe detects the presence of very low energy electrons (about 1 eV.) The ER gives a time resolution that varies according to energy bin and ranges from 1 to 6 samples per packet. At the high telemetry rate, we get 1-6 samples every 12 seconds.

The ER is an innovative method to measure planetary magnetic fields remotely. The ER measures the flux of electrons received at the instrument

through a range of energies by angle. Coupled with information about the local magnetic field direction, the pitch angle distribution of the electrons can be established. Because charged particles can be reflected from regions of higher magnetic field, examining the pitch angle distribution of electrons returning from the planet determines the magnetic field at the point of reflection. In this way, the ER not only provides information on the electron plasma *in situ*, but also measures the magnetic field remotely.

There is an important note about the ER data. Analysis has shown that the readings in electron fluxes under 30 eV are severely contaminated by locally produced photoelectrons [*Mitchell*, private communication.] Therefore, data from the Langmuir probe mode can not be used at all, and the lowest 4 energy bins of the ER should be taken with a grain of salt.

In addition, in order to be able to handle the high electron fluxes after the shock, the ER has an attenuator built in that essentially ignores other electron counts as it is processing any one given electron. The actual electron flux can be estimated by scaling the counts detected by a timing factor. When the correction factor exceeds 1.25, we consider the measurement to be saturated. This data must be discarded. Generally, the 115 eV energy bin is most likely to saturate. Much of the data from that bin is lost.

3.3 The Orbital Geometry

The intended orbit for MGS for its primary mapping mission is a circular, near-polar, sun-synchronous orbit at 2 p.m. local time at an altitude of about 378 km. This orbit was chosen to maximize planetary coverage, maintain lighting angle for the camera, and preserve the instruments from damage due to the atmosphere. The spacecraft achieved the mapping orbit in late February, 1999. This orbit is not ideal for solar wind studies due to the lack of variation in regions

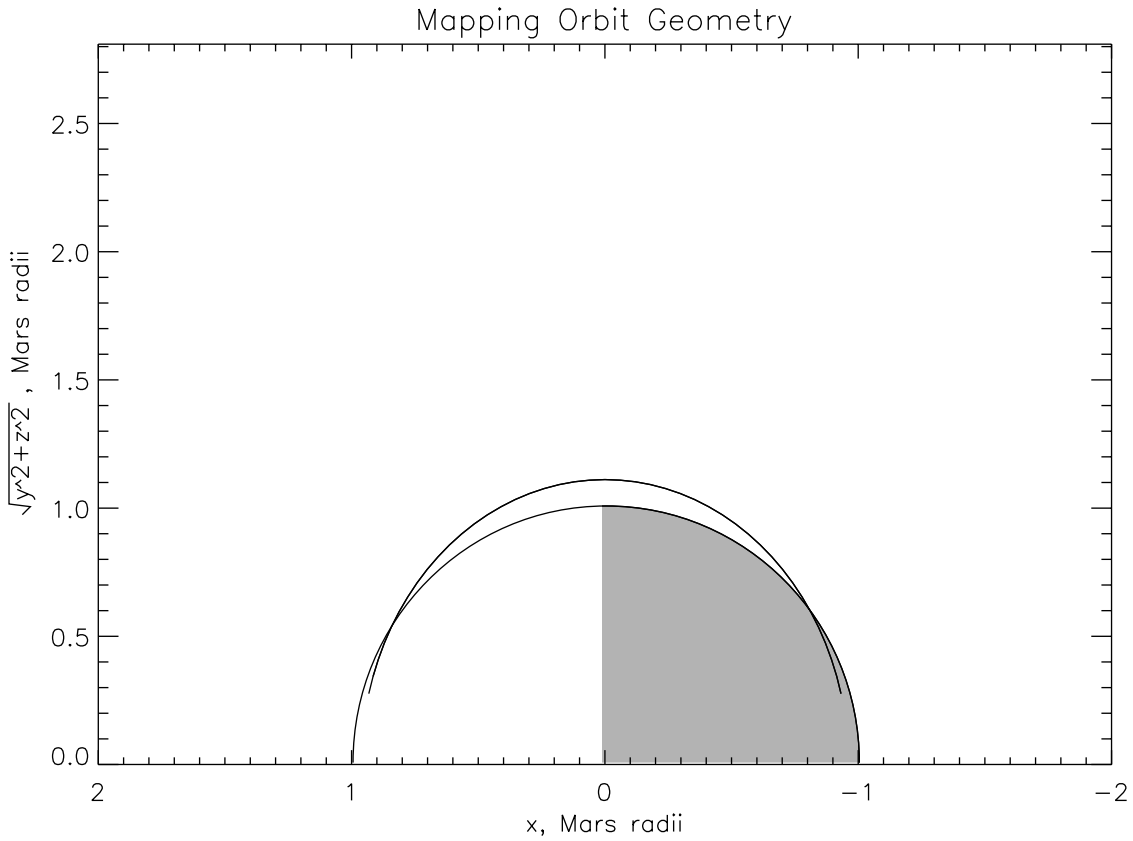

Figure 3.1 The MGS mapping orbit in cylindrical coordinates. The Sun is to the left on the x axis. The orbit is a 2 a.m. near-polar, sun-synchronous circular orbit at 378 km altitude.

sampled. At most, the spacecraft sees the ionopause height fluctuate vertically in the mapping orbit. This information is not very useful without accompanying upstream solar wind information. Figure 3.1 is a plot of this orbital geometry in cylindrical coordinates. The Sun is in the +x direction on the abscissa. The spacecraft position relative to the Mars-Sun line ($\sqrt{y^2+z^2}$) is plotted on the ordinate axis.

However, due to NASA's "faster, better, cheaper" policy, MGS did not carry the propellant needed to perform a burn to go directly into the mapping orbit. Instead, the spacecraft attained its mapping orbit after a series of aerobraking maneuvers, in which it used the drag of the atmosphere on the spacecraft to slowly decrease the period of the orbit and the altitude of apoapsis.

In fact, upon insertion into Mars orbit on September 11, 1997, MGS initially had a period of 45 hours and an apoapsis of 50,000 km. This is quite distant from the 2 hour period of the mapping orbit.

The aerobraking orbits were configured such that the periapsis was sufficiently low for the spacecraft to dip into the martian atmosphere. The average atmospheric pressure for aerobraking orbits was .2 N/m^2 [*Albee et al.*, 1998]. This called for periapsis altitudes just over 100 km. At such low altitudes, the spacecraft was well below the main peak of the ionosphere. As a result of the highly eccentric orbit, during most of the aerobraking orbits, the spacecraft sampled altitudes from the pre-shock region, through the bow shock, to the mantle, the pile-up region, the ionosphere and below. This invaluable data contains much information pertinent to the study of the solar wind interaction. It is interesting to note that this data would not have been available if it were not for the "faster, better, cheaper" demand for aerobraking!

During periapsis pass number 15 (P15) there was a problem with one of the solar arrays. Engineering data implies that one solar panel had moved beyond the maximum possible extent of the array. Analysis determined that a joint on the array had bent. The total pressure on the solar arrays during aerobraking would need to be decreased to insure the integrity of the spacecraft. While this analysis was being performed, the spacecraft paused from aerobraking. Therefore, this set of orbits is called the "hiatus orbits." The periapsis altitude rises to about 175 km [*Albee et al.*, 1998] for 14 orbits. The orbital configuration is shown in figure 3.2 in cylindrical coordinates. Local time for the spacecraft is 5:30 p.m. and the spacecraft period is 35 hours for these orbits.

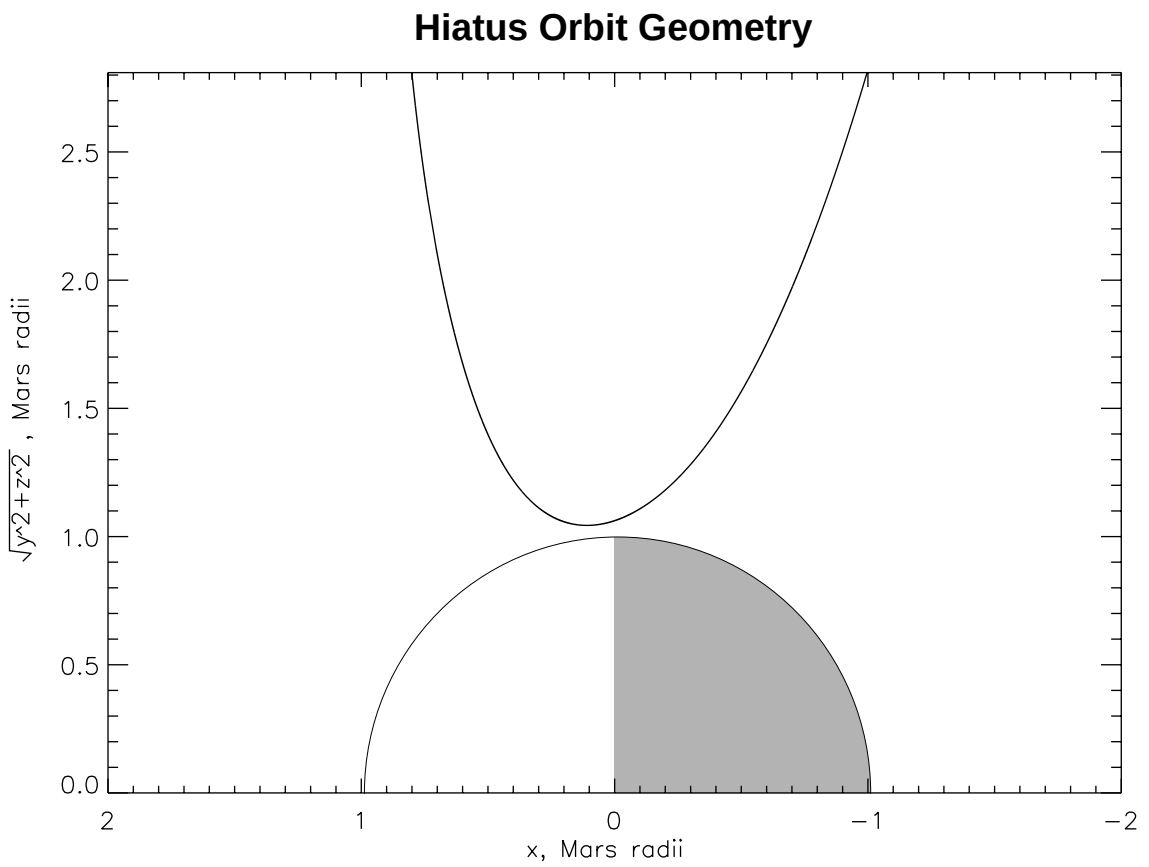

Figure 3.2 The MGS hiatus orbit in cylindrical coordinates. The Sun is to the left on the x axis. The local time of orbit is approximately 5:30 p.m. with a periapsis altitude of 175 km and apoapsis well off of the plot.

Due to the hiatus in aerobraking followed by a less aggressive aerobraking program, the spacecraft was not able to establish the intended mapping orbit. The local time of orbit passed the desired 2 p.m. before the period of the orbit had decreased enough. Therefore, the project decided to take another break from aerobraking in order to allow the local time of the orbit to phase to 2 a.m., a similar configuration to the planned 2 p.m. orbit. The set of orbits during this 5 month period is called the Science Phasing Orbits (SPO.) Similar to the hiatus orbits, the altitude of periapsis is raised to about 175 km in SPO, a high enough altitude to cease aerobraking. The period of the SPO orbits remained constant at 11.6 hours with an apoapsis of 17,865 km. From the initiation of SPO on March

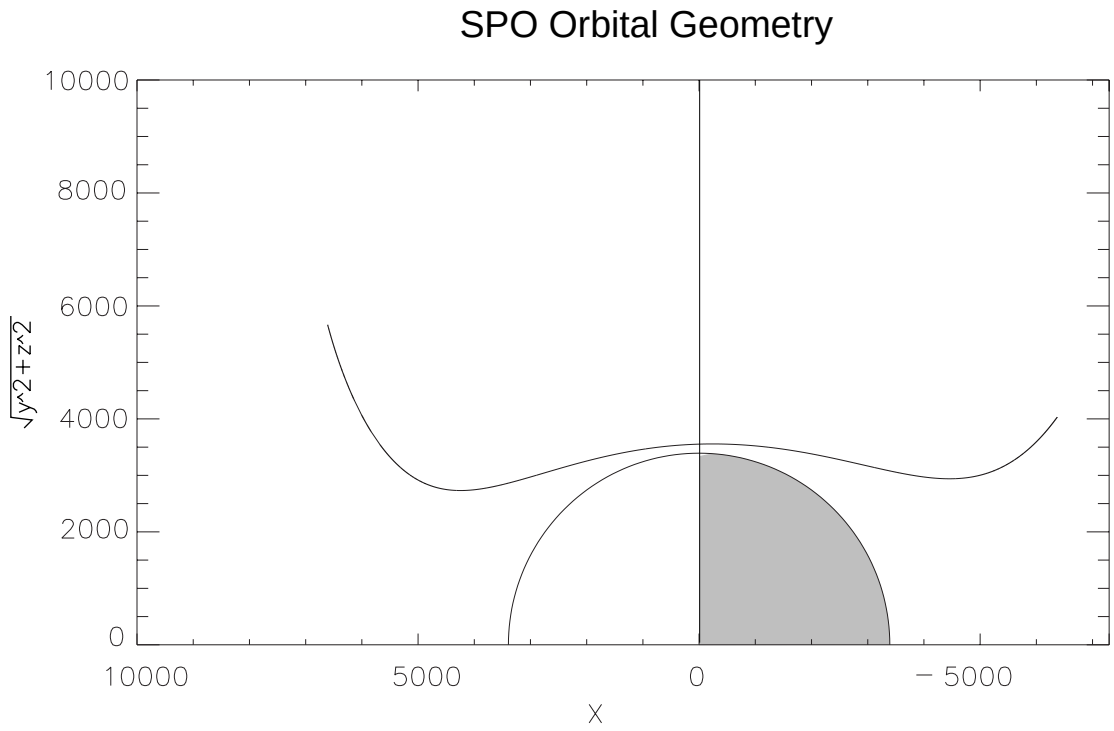

Figure 3.3 The MGS SPO orbit in cylindrical coordinates. The Sun is to the left on the x axis. The local time of orbit ranges. The periapsis altitude is around 175 km.

27, 1998 to the end of SPO on September 23, 1998, the local time of periapsis moved from noon to pre-dawn and the latitude of periapsis traversed 60-85°N. The SPO orbits are P202-P573 with data from several orbits throughout the month of May 1998 missing due to solar conjunction. Figure 3.3 displays the orbital geometry of an example SPO orbit, P231.

Figure 3.4 from *Albee et al.* [1998] summarizes the orbital periods, local time of periapsis, and operation mode as a function of time. The flat regions in period are the hiatus and SPO orbits. The regions with changing period indicate aerobraking is occurring. The shaded region around 10 a.m. spacecraft local time shows the loss of data due to solar conjunction. Also, notice the change in slope of orbital period after the hiatus as aerobraking was reduced to a slower rate.

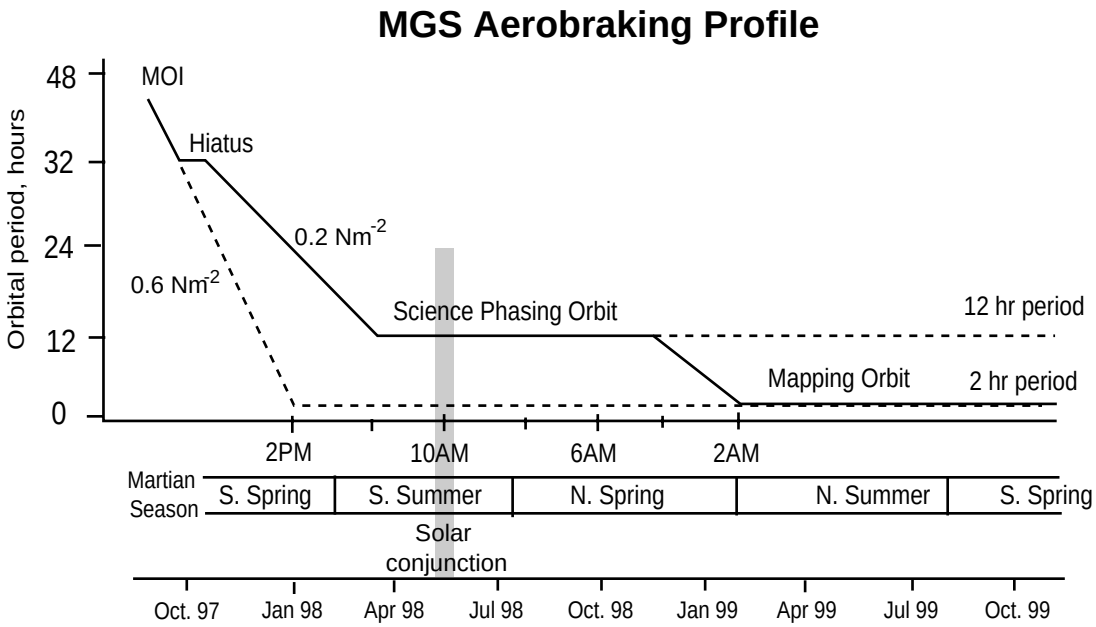

Figure 3.4 (from *Albee et al.*, 1998) Schematic of the change in MGS orbital period to achieve the mapping orbit from Mars Orbital Insertion (MOI). The topmost markings on the x axis indicate the local time of orbit. The next labels show the Martian Season corresponding to the dates on the lowest axis. The Nm^{-2} marking give the target pressure for aerobraking under the intended scheme (dashed line) and the actual scheme (solid line.)

3.4 The Selection of Data

Although the low altitude of periapsis in the aerobraking orbits is desirable in the study of ionospheric phenomena and crustal anomalies, we do not use this data in our analyses. Aerobraking requires the presence of an atmosphere. The electrostatic analyzer operates at a high voltage. The high density of neutral species provides a medium to facilitate electrical arcing in such a large potential difference. Because of the risk of damage from electrical arcing, the high voltage of the ER must be turned off during the periapsis pass in aerobraking. During the periapsis pass, the ER operates in Langmuir probe mode instead. Therefore, the aerobraking orbits lack the full spectral and angular data for the electrons that is available during the SPO and hiatus orbits. Because of the availability of

complementary ER data to corroborate the MAG data, we focus on the SPO and hiatus data in this analysis.

In addition, the MAG data from the aerobraking orbits is complicated by their location on the ends of the solar arrays. The solar panels are rotated and angled to facilitate aerobraking. Also, the pressure of the atmosphere on the solar arrays cause them to flutter in an unpredictable manner. The motion of the solar arrays relative to the spacecraft change the spacecraft magnetic field detected by the magnetometers. Deconvolving the changing spacecraft field is timely and still uncertain. The solar arrays remain relatively steady in the SPO and hiatus configuration, leaving the MAG data far cleaner for these orbits. It is interesting to note that if aerobraking had proceeded according to plan, the hiatus and SPO data would have not been available.

4. The Magnetic Pile-Up Boundary

Upon looking at the MAG/ER data of most of the passes in the hiatus and SPO databases, we discover a feature in the dayside sheath of Mars that is present for most of the orbits. This feature is the magnetic pileup boundary (MPB.) It has several signatures in both the MAG and ER data. We first examine one orbital pass in detail, studying the whole dayside region with MAG/ER data. Then, we present several other examples and discuss the similarities and differences of the features from orbit to orbit.

The orbital geometry of a typical orbital pass, P231, is shown in figure 4.1 in solar-cylindrical coordinates. The spacecraft periapsis is at 175 km. Figure 4.1 is marked with convenient time stamps to relate the spacecraft position to the time series plotted in Figure 4.2. The top panel of figure 4.2 shows the electron flux at the 18 energy bins on a *log* scale. The highest energy electrons have the lowest flux and vice-versa. The bottom panel shows the time series magnetic field magnitude data.

4.1 The MPB in ER Data

Examining the ER data in figure 4.2 from right to left, we see signatures of the solar wind interaction with Mars as described in Chapter 2. Because the orbital geometry is such that the spacecraft comes over the nightside of the planet on the inbound pass and leaves through the dayside on the outbound pass, it makes more sense to follow the spacecraft backwards in time. That corresponds to proceeding forward with the flow (*i.e.* downstream.) Therefore, we follow the time series data from right to left.

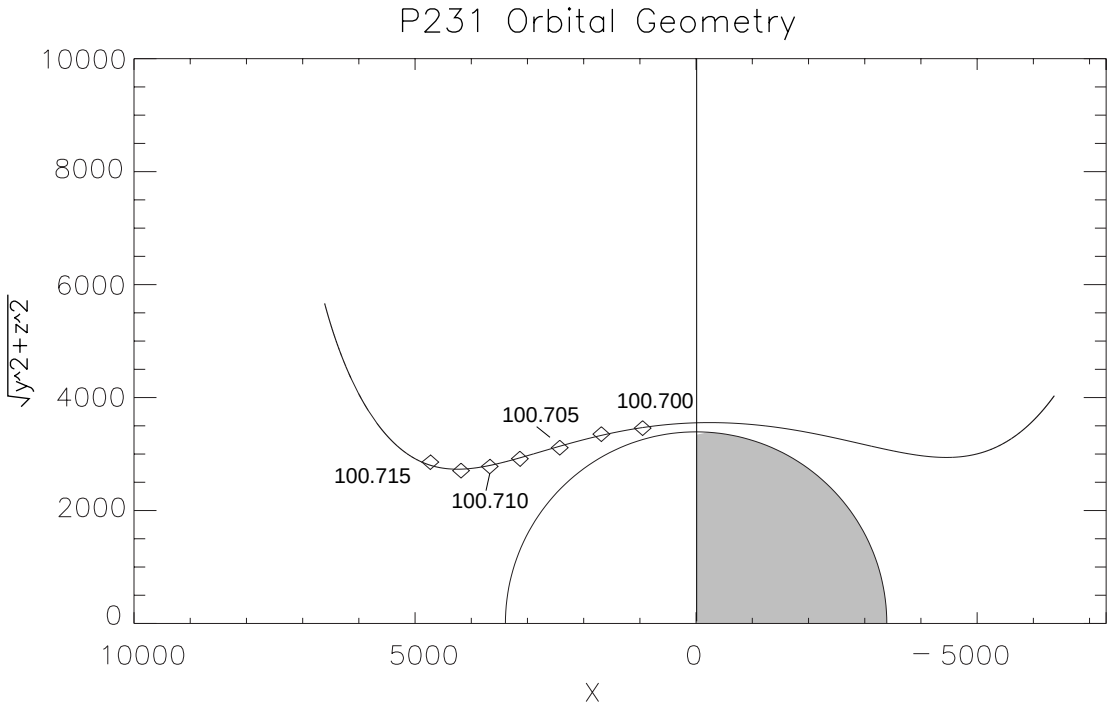

Figure 4.1 The orbital geometry for orbit P231. The time stamps are given for comparison with the time series given in the next figure.

The bow shock is identifiable in the ER data as a jump in the low and mid-range energy fluxes between decimal day 100.712 and 100.713. Upstream of the bow shock there is evidence of a shock foot. The electron fluxes ramp up slightly and wave activity appears from 100.713-100.717. The shock is marked by the amplification of wave structure. In the case of a quasi-perpendicular shock, in which the magnetic field lines are perpendicular to the shock normal, the electron fluxes jump decisively to an elevated level over a short distance. Waves are observed in the electron fluxes, but the dominant feature is the jump to a larger average count rate at the low and mid-energy bins. In the case of a quasi-parallel shock, in which magnetic field lines are parallel to the shock front normal, the wave activity dominates the shock. No single sharp jump of electron fluxes is observed in the midst of large amplitude waves. P231, as shown in figure 4.2, is of the quasi-perpendicular variety of shock front crossings. For the

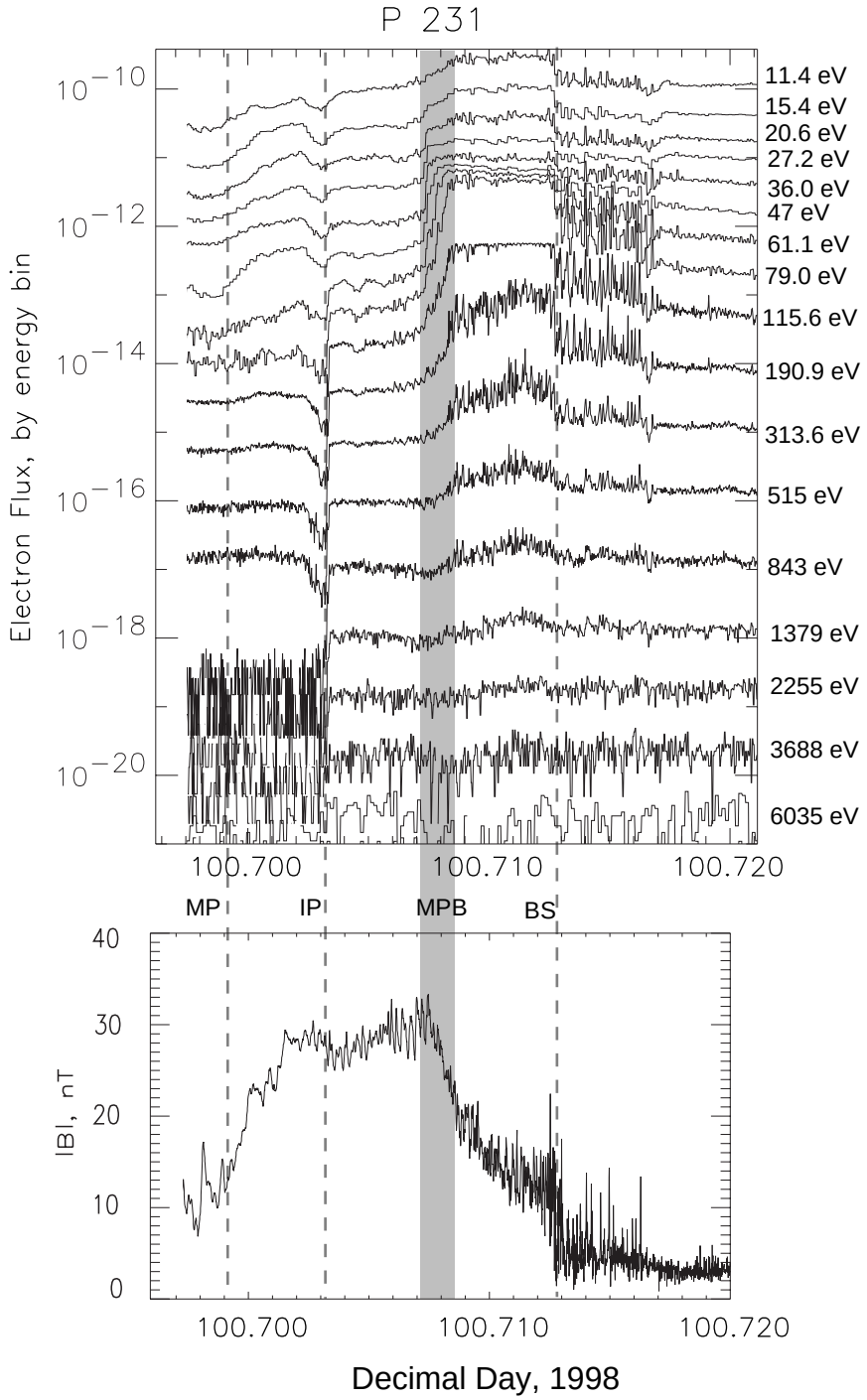

Figure 4.2 The ER (top) and MAG (bottom) data from the outbound pass P231. The distribution function of the electrons is plotted verses time by energy bin. The energy corresponding to each line is provided at the right hand side of the figure. Some plasma boundaries are marked with dashed vertical lines for reference. The leftmost line, marked 'EB,' is the exobase. The line labeled 'IP' represents the ionopause. The right-hand line (BS) demarks the location of the bow shock. The shaded region highlights the magnetic pileup region. The MAG data is shown below simultaneously.

.004 decimal days (around 5 min.) upstream of the shock, waves are present. But there is a distinct jump to the post-shock distribution, and that distribution is more or less maintained afterwards.

The electron flux keeps a steady level throughout the sheath from the bow shock until the MPB is reached. At higher energies, the MPB is a slow, steady decline in the electrons after the bow shock. Referring to the 190.9, 313.6, and 515 eV bins on figure 4.2, ones sees the slow loss of electron flux from 100.707 to 100.711 on the time axis. The total loss ranges from 1.5 orders of magnitude in the 190.9 eV bin to as little as a factor of 2 at higher energy, *e.g.* 1379 eV. But the most dramatic attenuation is seen in the 47, 61.1 and 79 eV bins. Between the time of 100.707 and 100.708, the fluxes quickly drop approximately 2 orders of magnitude. Continuing up to the lowest energy bins, there is still attenuation in conjunction with the magnetic pileup boundary. Below 20 eV, however, the drop is slighter and slower. The signature described above is typical of the electrons in the MPB for most periapsis passes.

Another way to inspect the electrons in the MPB is to plot their distribution as a function of energy at different times. Here, the changing shape of the distribution is evident. In figure 4.3, we plot one electron spectrum measured by the ER for several spacecraft altitudes between 800 and 1050 km. Those altitudes cover the entire MPB for this orbit. At the highest altitude, the spectrum is that of the post-shock electrons. This distribution is approximately the same shape from orbit to orbit and retains its shape over a large spatial extent in one orbit. The lowest altitude plot is the post-MPB spectrum. From the lowest energy to ~1000 eV, the post-MPB spectrum is roughly power law and stays constant until the spacecraft enters the ionosphere or a high altitude superthermal cloud.

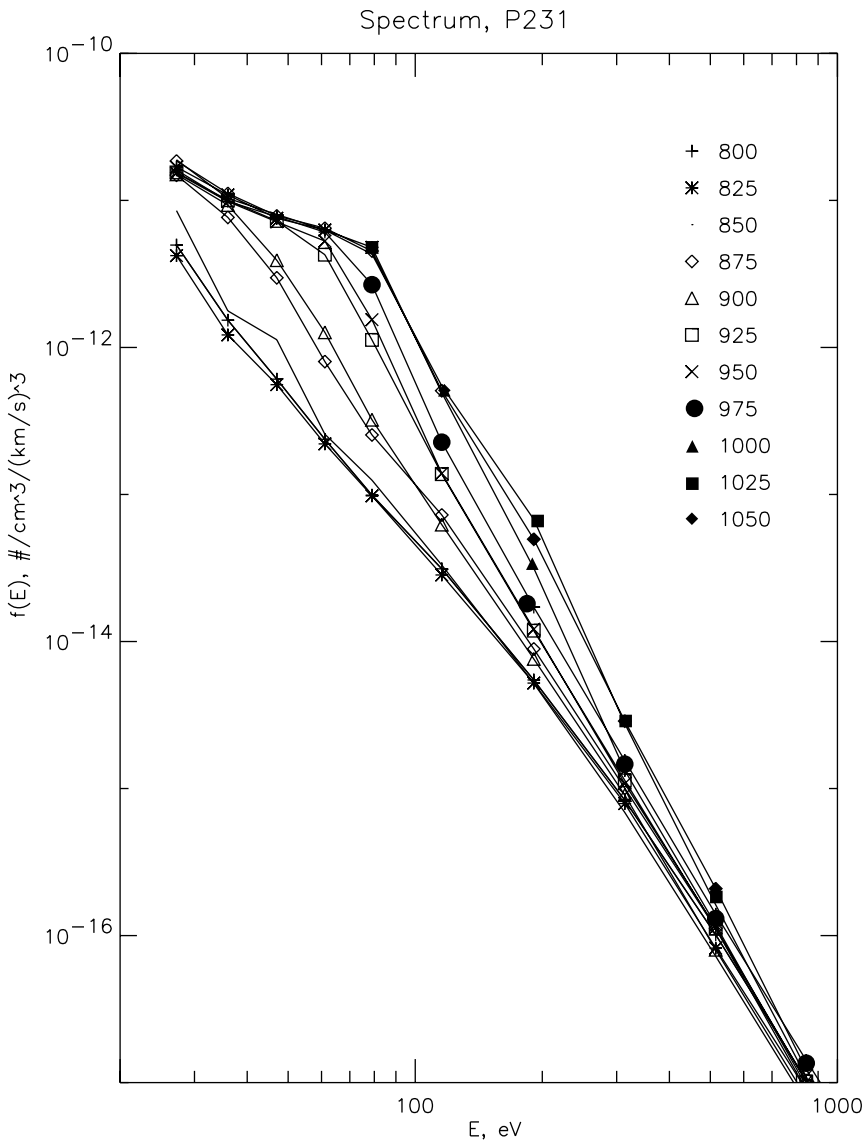

Figure 4.3 Electron spectra for several altitudes between 800 and 1050 km for P231. The spectrum evolves rapidly in space. From the bow shock until the first line plotted here, the spectrum remains relatively constant. However, one can observe the manner in which electrons lose energy as the flow progresses. First, small amounts of flux drop at high energy. When the attenuation begins at the 50-100 eV range, the evolution hastens. The resulting spectrum remains relatively constant until the ionopause.

However, the order in which the attenuation proceeds in energy through the MPB is the interesting feature of this plot. In figure 4.3, the distribution function first declines at the highest energy. The 1000 km spectrum (▲) first peels off from the post-shock distribution near 200 eV. By 975 km altitude, the

spectrum has separated at 79 eV. At this altitude, there is little effect of the attenuation at lower energy. Then, there is a large, sudden drop in the energy bins between 50-150 eV. The spectrum deflates by the bulk of the total amount over a small altitude range. In P231, it occurs between 850 and 925 km. For reference, 75 km is on the order of the typical exospheric scale height at Mars. From this signature in the evolution of the electron spectra, we conclude that some process is selecting electrons in the 40-150 eV energy range and cooling them.

Referring again to figure 4.2, we continue to follow the time series towards periapsis. After the shaded MPB region, there is a period where the electron fluxes maintain a constant level. In fact, there is very little variation in the fluxes from the bottom of the MPB until the spacecraft crosses the ionopause. The ionopause is marked by the sharp drop in >100 eV electrons. Within the ionosphere, the electrons are bound to the plasma, which is primarily of planetary origin. In P231, one can see the ionopause at energy $\geq$ 61.1 eV at 100.7032.

The lowest boundary detectable by the ER is the ionospheric main peak. Because the ionospheric main peak is the point where the optical depth for photoionization reaches one, it appears in the electron data as the bottom of the ramp in low energy electron flux. The low energy electron flux drops as a result of the loss of photoelectrons. In P231, the main peak is marked by the dashed line labeled "MP" at 100.688.

4.2 The MPB in MAG Data

Although the MPB stands out in the ER data, it was named for its signature in the magnetic field data. Indeed, there is a recurring feature observed in the magnetic field data simultaneous with the abrupt drop in electron flux. In figure 4.2, the magnetic field for P231 is shown as a function of time.

Like in the ER data, one should follow the data from right to left, as this corresponds to moving forward in space although it is backward in time.

The bow shock appears in the MAG data in figure 4.2 as a sharp jump in magnitude just before 100.713. The ambient magnetic field strength shifts from 3.5 nT before the shock foot at 100.718 to about 13 nT at 100.712. The shock jump in the magnetic field is fairly clean, indicating this is more of a quasi-perpendicular shock than a quasi-parallel shock in agreement with the interpretation from the electrons in the bow shock. A quasi-parallel shock would appear as a series of high amplitude waves in the magnetic field without a distinct jump in the ambient field strength. The jittery nature of the magnetic field is due to waves prevalent in the foreshock, shock and post-shock regions. In figure 4.2, wave activity arises in the magnetic field data upstream of the bow shock at the same time as waves appear in the electron measurements, from decimal day 100.713-100.716.

The wave activity continues inside the bow shock in the sheath region, usually persisting right up to the MPB. Detailed analysis of the wave structure after the shock shows that the waves have a large amplitude and a period near the local proton cyclotron period. Also, the waves are left handed circularly polarized. The wave polarization is determined by first calculating a mean magnetic field for a selected time interval and subtracting the mean field from each field vector in the time interval. The resulting magnetic field vectors represent the 3-D wave magnetic field.

Although the waves are prevalent in all data sets, we focus our attention on an orbit that very readily elucidates the nature of the waves, P456. In P456, the wave field has a magnitude greater than 5 nT. Using only the perpendicular component, we define an arbitrary zero angle and find the angle of the perpendicular wave field with respect to the zero such that a decreasing angle

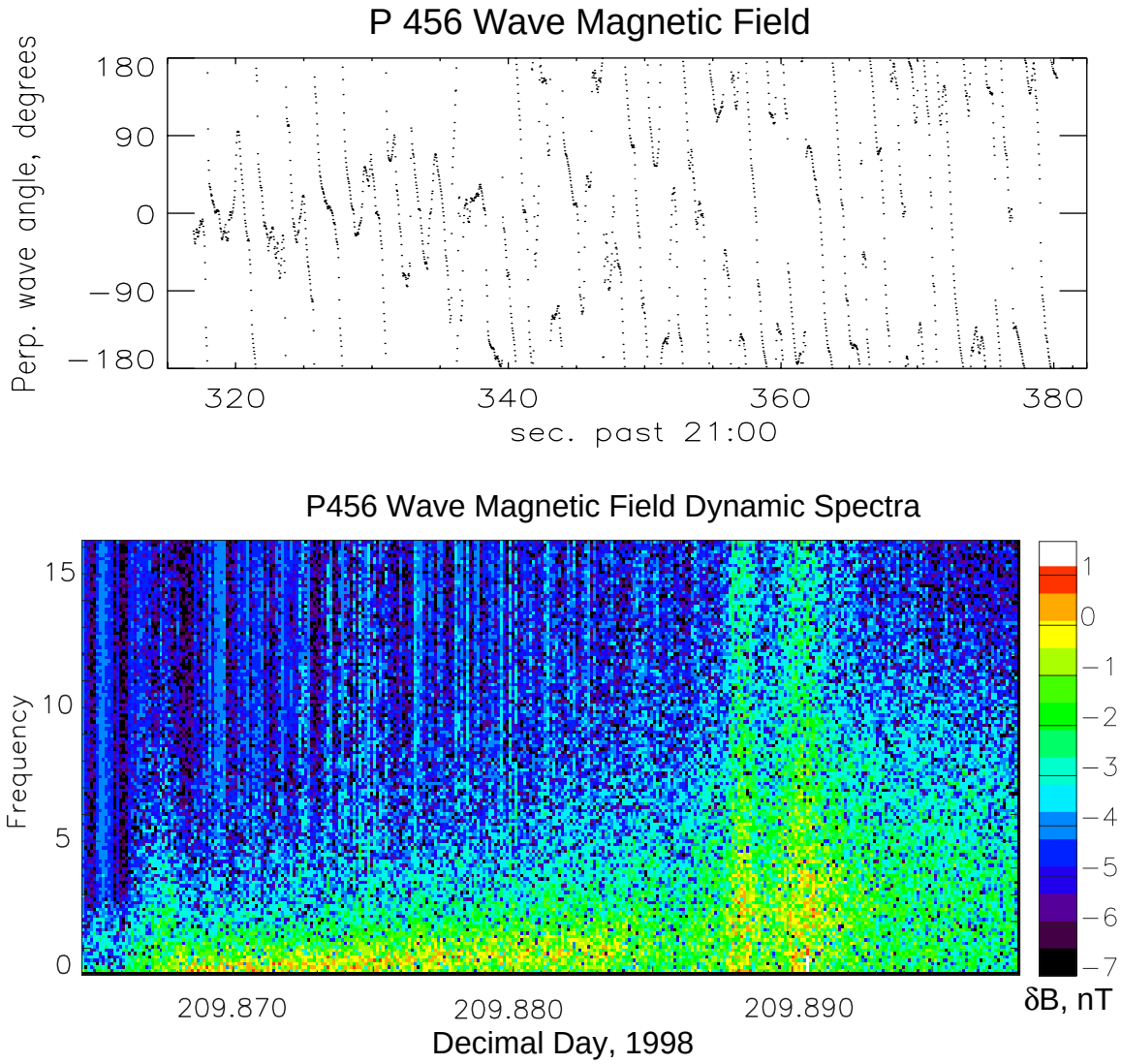

Figure 4.4 Rotation and dynamic spectra of wave magnetic field. The high resolution MAG data are taken from the post-shock, pre-pileup region. The top panel here is the angle of the wave magnetic field in the plane perpendicular to the mean field direction. It is left handed, circularly polarized. The dynamic spectra show power in the wave magnetic field at ~.5-1 /s.

corresponds to left handed polarization. A plot of the angle of the wave field in the plane perpendicular to the mean field direction, in figure 4.4, shows the direction of the wave clocking around with time. The angle decreases with time indicating left-handed polarization. An estimate of the frequency of rotation is 3.5 s^{-1}. With the mean magnetic field magnitude of 34 nT, the proton gyrofrequency is 3.3 s^{-1}.

Next, shown in figure 4.4 are the dynamic spectra of the wave magnetic field. Dynamic spectra show the evolution of power in magnetic field frequency by time. A Fast Fourier Transform (FFT) of magnetic field data for 512 point intervals is performed and displayed as a vertical stripe. Each successive time segment is then placed next to the previous, giving a composite image of the power in different frequencies of the field. In this example, most of the power is in the low frequency field, but no one line stands out. In a few other cases, distinct frequencies do appear and persist over extended periods in the dynamic spectra [*Brain*, *Acuña*, private communication]; however this seems to occur only upstream of the bow shock when the spacecraft is magnetically connected to the bow shock. It is interesting to note that although the FFT's do not, in general, single out one frequency, the eye does. The rotational pattern in the angle plot exists over tens of minutes of data, corresponding to hundreds of cyclotron periods and a spatial extent of thousands of kilometers.

The MPB is marked in the MAG data by two characteristics. First, it is the point where the magnetic field increases in the sheath. In P231 (see figure 4.2) the jump in field strength is steep. The field rises over 10 nT to ~30 nT between 100.707 and 100.709. In comets, the MPB was originally thought to be a discontinuity in the magnetic field. Although the ramp can be steep at Mars, MGS offers no evidence of the MPB being a rotational or tangential discontinuity in the field. The pileup in magnetic field occurs simultaneously with the sharp signature in the electrons.

Figure 4.5 shows the orbital geometry for P231 in magnetic coordinates from a top down perspective. Magnetic coordinates are the logical choice for viewing a feature associated with the solar wind. Rotating the Mars-Sun coordinates by 3.5° around the z-axis, we correct for the abberation angle of the solar wind flow velocity at Mars. Now, the y=z=0 line represents the stagnation

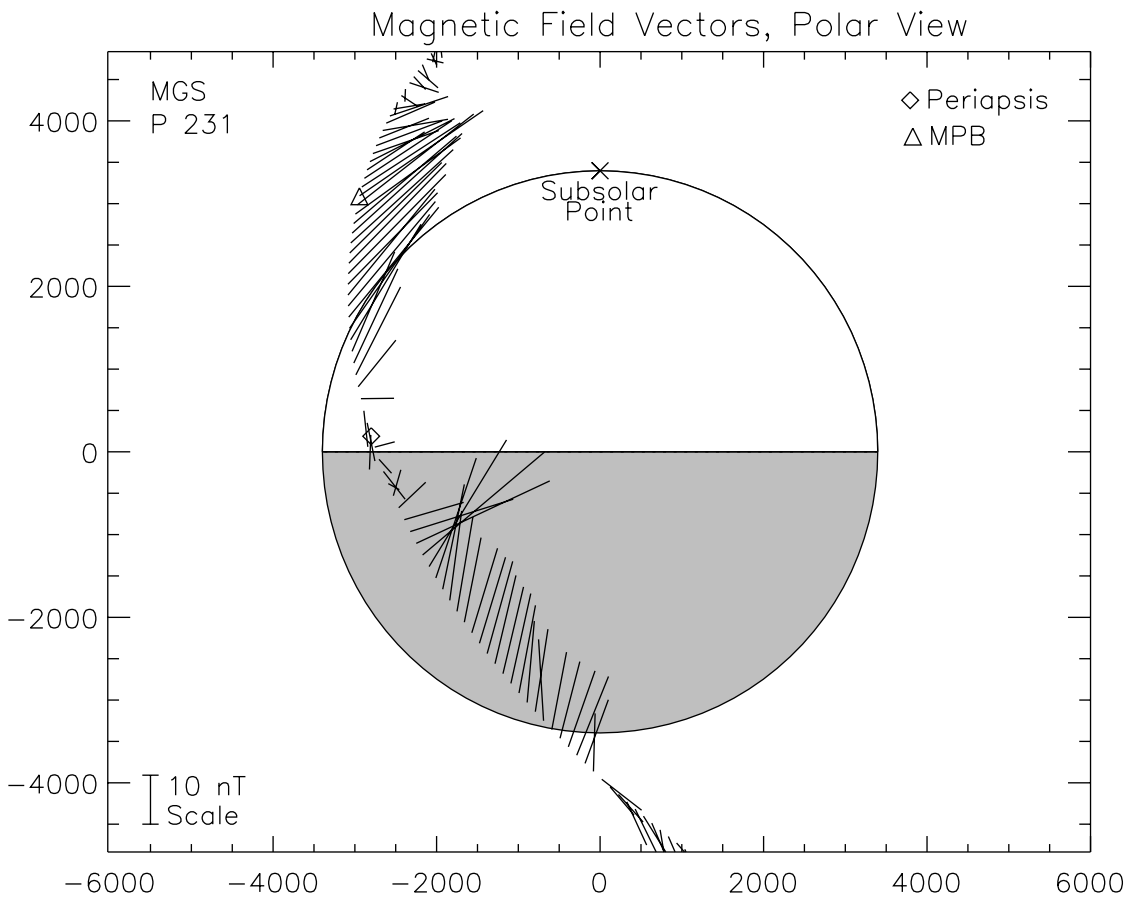

Figure 4.5 Magnetic field vectors projected into the magnetic ecliptic plane for P231. The vectors are plotted along the projection of the spacecraft trajectory. The size of a 10 nT field is given in the lower left corner for reference. Locations of spacecraft periapsis and the MPB crossing are also given.

line of the incident flow. Then, we rotate the data around the new x-axis such that the upstream solar wind has no z component. In this way, we largely remove the effects of the changing IMF from orbit to orbit. In magnetic coordinates, the sign of the x component of the magnetic field in the tail should change near y=0.

In figure 4.5, the location of the magnetic pileup boundary is marked along the spacecraft trajectory by a triangle. The magnetic field vectors are plotted along the trajectory of the spacecraft demonstrating the draping of the magnetic field on the dayside and the extension of the tail field on the nightside. For reference, the size of a 10 nT vector is given in the lower left corner. In this view,

it is also noticeable that the magnitude of the magnetic field increases at this point. However, the increase appears sharper here than the boundary actually is because only 1 in 25 low resolution vectors are shown here. Perhaps it was the sparse coverage in the cometary data that first suggested that the MPB might be a discontinuity.

It seems from the study of many orbits that the MPB coincides with the place where the waves in the magnetic field cease. Although this is not always the case, it is the norm. In P231, the waves persist after the MPB. During the build up, no waves are observed, but any waves present would be difficult to detect over the signal of the amassing field. However, as will be shown in the next section, the waves do tend to dampen out inside of the MPB. P231 is not the norm in this case.

4.3 More Examples of the MPB in MAG/ER Data

More examples of the MPB, in the form of figure 4.2, are shown in figures 4.6, 4.7, 4.8, and 4.9. Four more periapsis passes, P236, P253, P257, and P456, demonstrate the range of pileup boundaries seen at Mars.

P236

P236, in figure 4.6, has the same orbital geometry in magnetic coordinates as our original example, P231. The MPB is close to the magnetic equator at a solar zenith angle of near 45°. Here, the magnetic pileup occurs from decimal day of 1998 103.1349 to 103.1365, where the altitude ranges from 839-1063 km. The wave activity is seen to diminish immediately upon magnetic field build up, which is coincident with the gradient in electron flux in the energy bins from 61.1-843 eV. The electron fluxes at E < 61.1 eV do not decline over the entire MPB, as shown in the shaded box. In the MPB, the magnetic field mounts from 16 nT

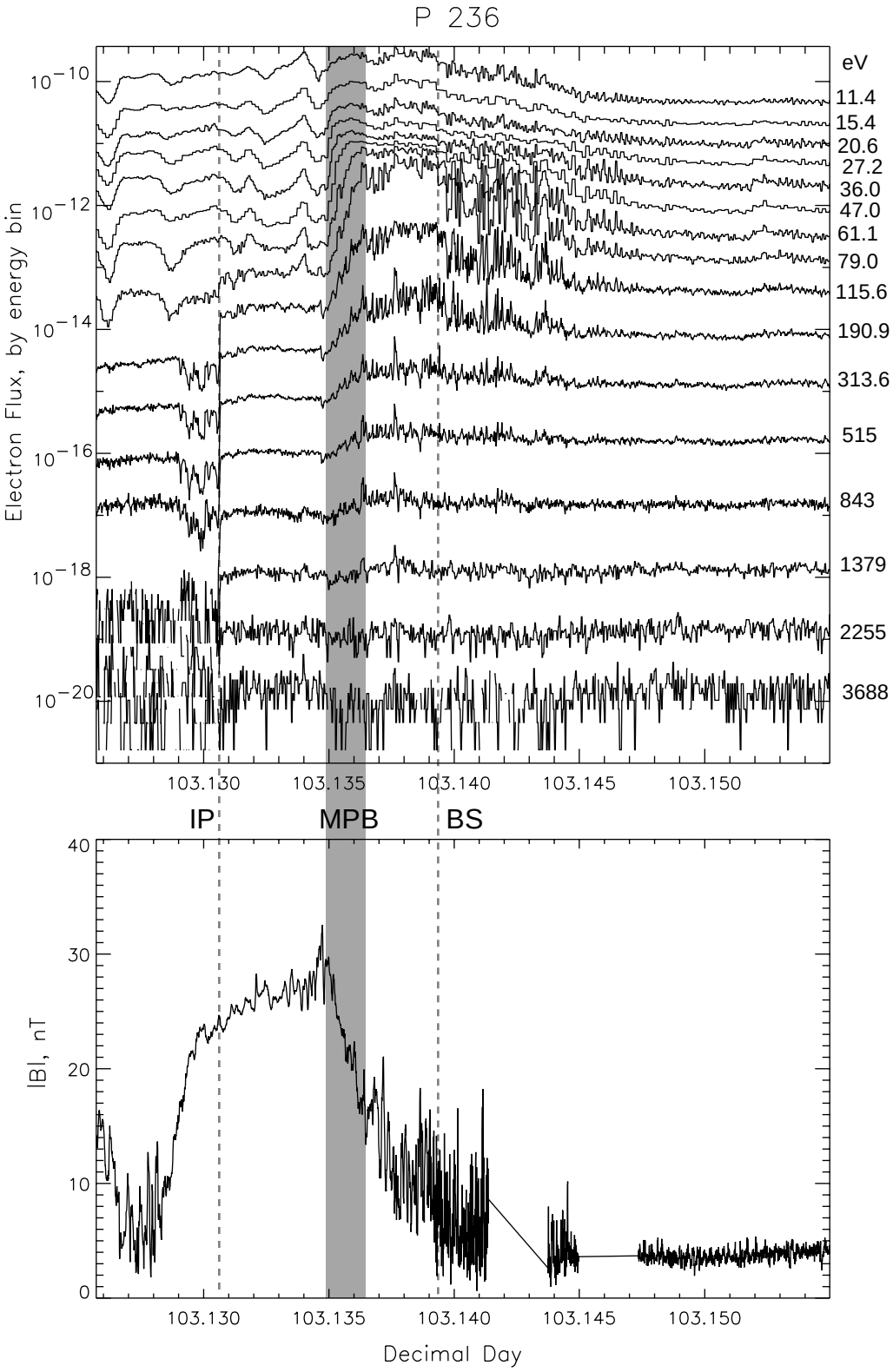

Figure 4.6 ER and MAG time series for P236 in the same format as figure 4.2.

to 29 nT. That corresponds to the magnetic field accounting for 3 times more of the incident solar wind ram pressure.

The spacecraft does not cross the ionopause until an altitude of 402 km. At the ionopause crossing, the spacecraft is located at 8 a.m. local time and a SZA of 61°. Notice, however, how constant the electron distribution function is for E > 61.1 eV between the MPB and the ionopause. This is the cooled electron spectrum and commonly is seen as steady as in P236.

P253

The MPB in P253 (figure 4.7) shows how abruptly the pileup can occur. However, it is hard to determine the rotation into magnetic coordinates for this orbit. The direction of magnetic field in the tail does not coincide with the direction expected when looking at the dayside draping. Therefore, it seems that the IMF is not steady during this orbit. Although we can not place this orbit on the magnetic map, it is still worthwhile to study some of its features. The wave activity is strong in the post shock, partly due to the quasi-parallel alignment of the shock. But that wave activity ceases at the MPB, which covers the time period of 111.387±.0005.

The MPB is located at an especially low altitude, from 708 km to 776 km as demarcated on figure 4.7. Looking at the altitudes where the high energy fluxes decline, the MPB extends to altitudes only as high as 1032 km. This is the most condensed altitude range in the examples we present here. The altitude of the ionopause is especially low for this orbit however. Whereas the other examples have the ionopause at or above 400 km, the ionopause for P253 is down at 285 km. When accounting for the solar zenith angle of the ionopause measurement, this translates to a sub-flow ionopause at 160 km. However, immediately below the MPB, the spacecraft encounters an ionospheric cloud.

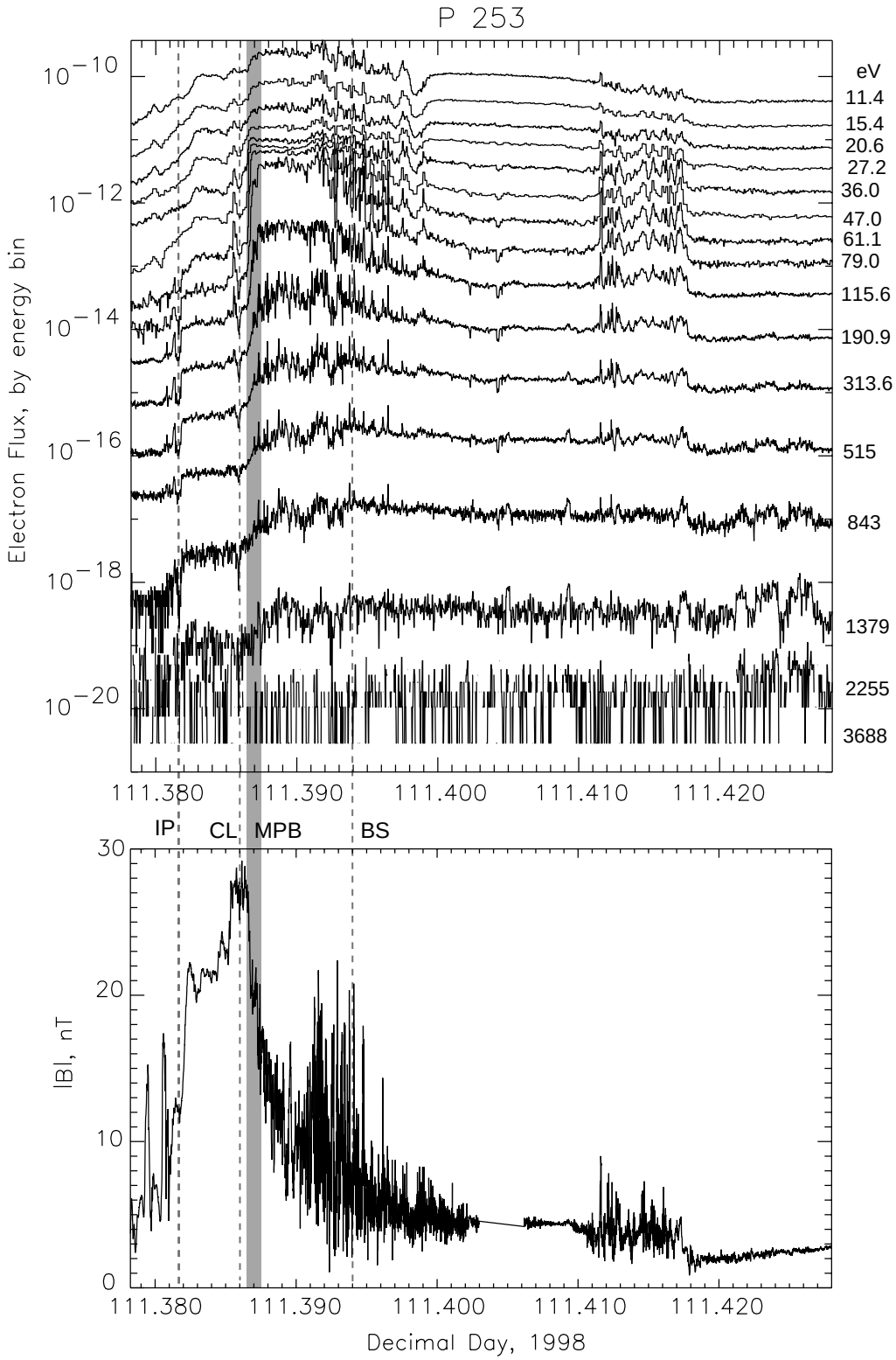

Figure 4.7 ER and MAG time series for P253 in the same format as figure 4.2. Here, the location of an ionospheric cloud is also included as the dashed line marked "CL."

The reduced fluxes in all energy bins around 111.389 indicate that colder, ionospheric plasma is present.

An interesting feature to note in P253 is the wave packet in both the MAG and ER time series between 111.411 and 111.418. These packets are not uncommon. In fact, the circular polarization of the waves returns in these packets, although at a new frequency. It is thought that these regions are simply places where the magnetic field lines are connected to the bow shock [*Acuña, private communication*.] Sometimes the regions persist upstream for an extended time period. Other times they are a patchy phenomena, turning on and off very abruptly over short distances.

P257

During P257 (figure 4.8), the IMF is considerably out of the plane of the ecliptic. Rotating around the abberated x axis by -80.9° brings the orbit into magnetic coordinates. In these coordinates, the MPB appears at SZA of 47-49°. The local time of the MPB is 2:30 p.m. The magnetic latitude of the MPB is considerably higher than for P231 and P236, which occur at the magnetic equator. In P257, the MPB covers 26-29° N.

No obvious ionopause crossing is detected on P257. The ionopause is defined as the location where the spacecraft detects a drop in 100-1000 eV electrons. But, an ionospheric spectrum at Mars contains a peak near 500 eV from Auger electrons resulting from the K shell ionization of oxygen [*Mitchell, private communication*.]. This peak does exist for P257 at altitudes below the MPB. Therefore, we believe that the spacecraft does not detect the ionopause crossing because it is disguised by the proximity of the MPB flux signature.

The MPB in this orbit is a more subdued version of the others. It only covers 150 km altitude at low energy and in the magnetic field. The time of onset

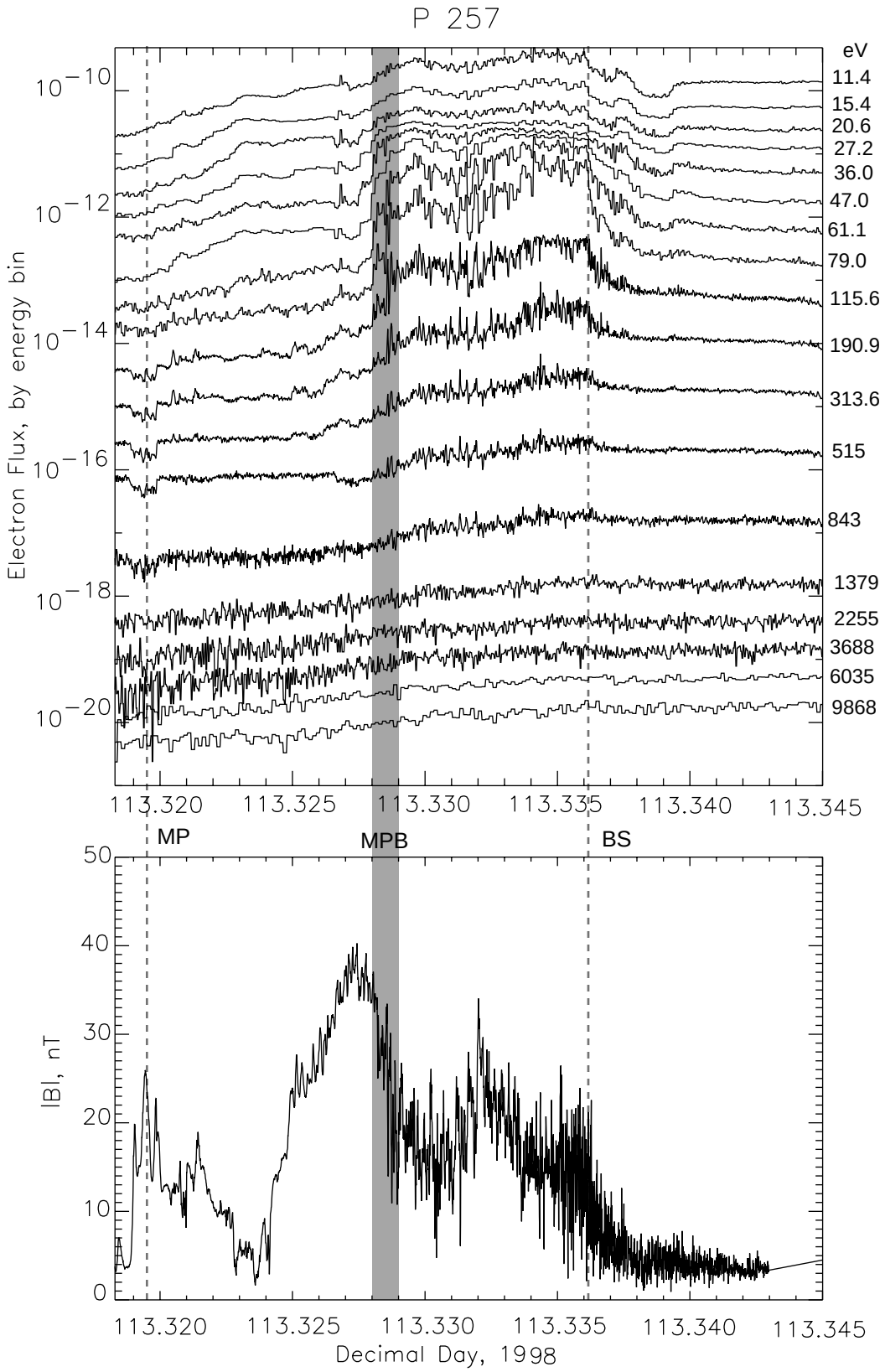

Figure 4.8 ER and MAG time series for P257 in the same format as figure 4.2. No obvious ionopause is detected in this orbit.

for high energy is not as easy to determine. However, in general, the fluxes do not lose as much in the MPB of P257 as in the other examples. This is especially intriguing because one might expect the combination ionopause/pileup boundary to produce a larger overall drop in electron fluxes.

P456

P456 is known among MGS scientists as the "high field case." The upstream IMF has a magnitude of about 16 nT, as shown in the bottom panel of figure 4.9. The typical IMF at Mars is less than 5 nT. Electron fluxes are also elevated in the solar wind. So, as the stronger solar wind passes the planet, we observe the characteristics of an interaction with increased upstream pressure. The magnetic field trace is much closer to those normally seen in a orbital pass around Venus than at Mars. The bow shock is a strong shock with an obvious discontinuity in the magnetic field and electron fluxes. Wave activity persists in both data sets from the bow shock to the MPB. Partially up the magnetic field ramp, the waves subside. This is the orbit used for the wave analysis discussed in section 4.2. From 209.879 to 209.888, the left handed polarization pattern is easily seen in a wave angle plot.

The MPB is especially spread out in this case. In fact, the attenuation in the separate bins in the ER is almost simultaneous. There is no disparate onset time depending on energy, making this a unique orbit. While the high energy fluxes decline at a constant slope throughout the shaded region in figure 4.9, the gradient in the low energy fluxes steepens towards the planet. But the electrons are cooling at all energies throughout the MPB. The total attenuation is about the same as for other orbits. In this orbit, fluxes are higher due to the unusual solar wind conditions. But the largest drop is two orders of magnitude in the 79 eV bin,

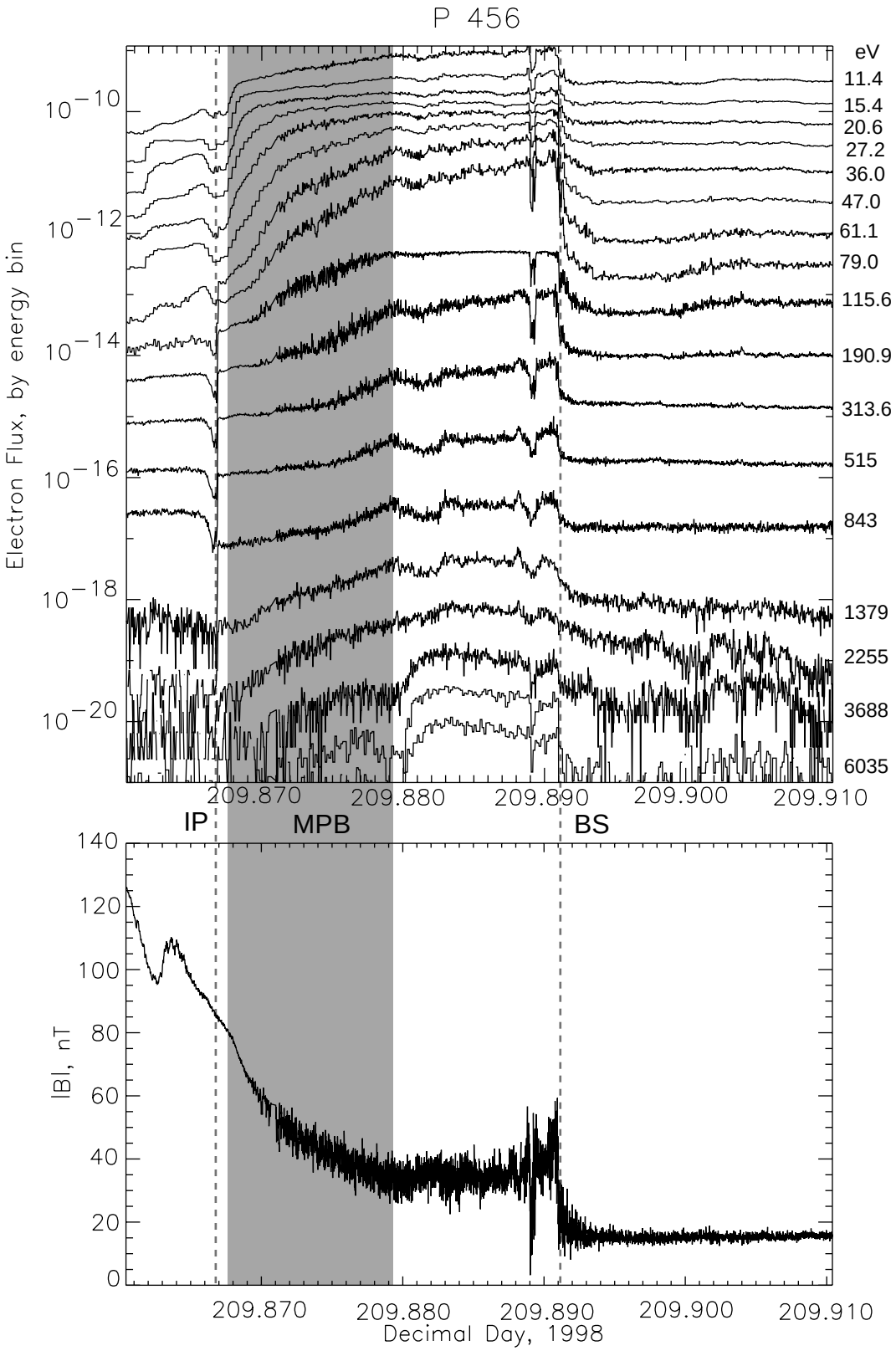

Figure 4.9 ER and MAG time series for P456 in the same format as figure 4.2.

similar to P231. The elevated fluxes do allow the MPB signature to rise above the noise level even in the highest energy bins.

However, the way in which the magnetic field piles up in P456 is intrinsically different than in our other examples. Here, the gradient is slow and smooth. In other examples, the magnetic field gradient is sharper. Further, the magnetic field continues to mount after the spacecraft enters the ionosphere. In all of our previous examples, the magnetic field strength levels off when the attenuation of the electrons stops. Here, there is only a short distance from the bottom of the MPB to the ionopause. The magnetic field continues to pile up only at a lightly reduced slope than in the MPB.

Discussion

Electron distribution plots for 4 other periapsis passes appear in figure 4.10. Clockwise form the top left panel, these are the spectra for P236, P253, P456, and P257. Notice that although the absolute fluxes, the distance over which the attenuation occurs, the altitude of onset/offset, and the final configuration vary somewhat from orbit to orbit, the general qualitative features remain the same. All begin with a post-shock spectrum that is decisively non-Maxwellian. The post shock spectrum has a thermal bump at 79 eV, but the fall off does not match the slope of a Maxwellian distribution. Though it is not demonstrated in this plot, referring to the plots in figure 4.2 and 4.6-4.9 will reveal that the post-shock spectrum is constant in any one orbit for $E < 115$ eV from the bow shock to the MPB.

On the onset of the MPB, many properties vary from orbit to orbit, but the manner in which the attenuation sets in is common to all these orbits. Like in P231 (see figure 4.3,) the electrons first peel away from the post shock spectrum at the higher energies. A very dramatic decrease in low energy electrons is

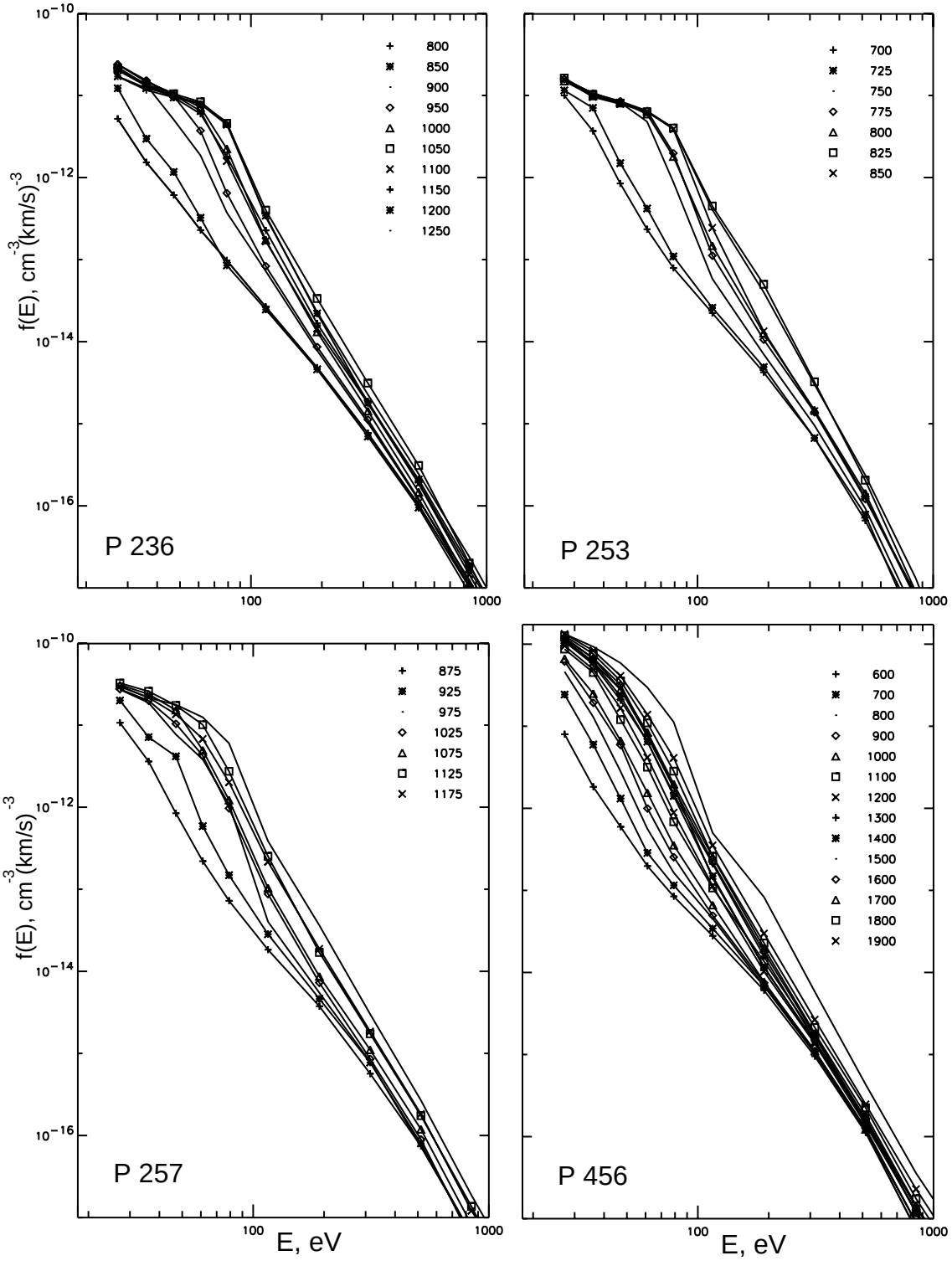

Figure 4.10 Several more orbits form MGS exhibiting the MPB. The format is the same as in figure 4.3. The periapsis number is listed in the lower left corner for each panel.

seen, with a gap forming between 36 eV and 115 eV in all examples except P456.

Now, notice the altitude ranges covered by the plots. P236 shows spectra from 800-1250 km. The spectrum changes over the altitude range of 800-1100 km. This is typical of very many orbits, including P231 discussed earlier and P257 in this plot. In contrast, the distribution evolves over only 150 km altitude in P253. P456 has the other extreme where the spectrum continuously develops over 1500 km altitude.

The magnetic field magnitude for several outbound passes is included in figures 4.6-4.9. The build up in magnetic field is variable in its rate, size and altitude. However, it always coincides with the attenuation in electron flux. Where the MPB is a gradual transition in the electrons, it is also gradual in the magnetic field. Likewise, where the electrons drop as a steep gradient, the magnetic field mounts quickly too.

Vignes et al. [1999] have performed a fit to observed MPB crossings to determine the geometry of the boundary. Preliminary results indicate that the MPB follows the conic section:

$$r = L \big/ (1 + \varepsilon \cos\theta)$$

where r and θ are coordinates measured with respect to a focus located at (.98 R_m,0,0) and with the parameters:

$$\varepsilon = 0.94$$
$$L = 0.83 R_m$$

where ε is eccentricity and L is the conic parameter. This equation is plotted in cylindrical coordinates in figure 4.11. At the solar zenith angles sampled by MGS in SPO, this places the MPB at altitudes of around 800-1200 km. That agrees with the location of the MPB in our analysis. However, Vignes et al. predict a subsolar location that is much higher than we expect. This is the result, we propose, of their extrapolation of the data. MGS has very little coverage of low

solar zenith angles. It has even less MPB crossings at low solar zenith angle. Therefore, there is no data for MPB crossings below 30° solar zenith angle in the SPO data set. We believe that the fit does not give the correct results at low solar zenith angle, and has a lot of spread at high solar zenith angles.

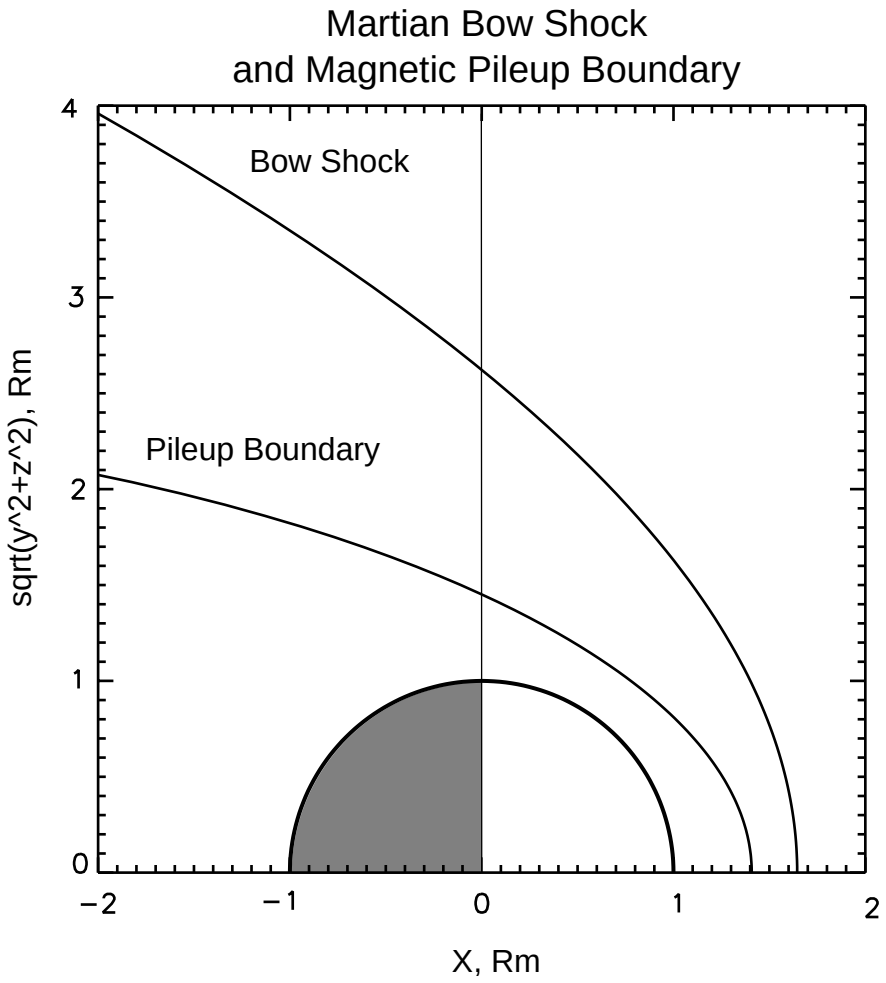

Figure 4.11. The positions of the magnetic pileup boundary and bow shock as determined by a fit of MGS MAG data to conic sections by *Vignes et al.* [1999]. The planet is shown as a circle at R_m=1 for reference. The Sun is to the right in this plot.

5. Modeling the Electrons in the Pileup Boundary

There are two major pieces of evidence suggesting the physics behind the formation of the magnetic pileup boundary. One sign is the behavior of the electrons. The other clue is the appearance (and termination) of waves consistent with ion-cyclotron waves. We first use the argument of *Cloutier et al.* [1999] to explain the waves in the magnetic field and relate them to the presence of the MPB. Then we dissect the signature in the electrons and determine the physics of the formation of the MPB. Afterwards, we present a model that reproduces the electron spectra in the pileup region.

5.1 Physical Explanation of the Observations

Referring once again to the figures in chapter 4, we examine the wave structure in the magnetic field. The waves are consistent with ion cyclotron waves at the proton gyrofrequency. Ion cyclotron waves are left handed circularly polarized and propagate parallel to the magnetic field. These qualifications are met by the data, as seen in figure 4.4.

One possible mechanism for producing these waves is an unstable ion population. In the post-shock region of Mars, it is very easy to produce such an unstable population. Exospheric neutral atoms and molecules exist at high altitudes all around the planet. The planetary neutrals are analogous to the cometary coma. Any one of a number of chemical processes can cause the ionization of these neutrals. Most of the ionization processes, as discussed in chapter 2, give the newly formed ion very little kinetic energy. The neutrals are originally at rest in the planetary rest frame, so the new ions are as well. Therefore, once the neutral is ionized, it suddenly sees the incident magnetized plasma flow with a very large relative velocity. This translates to a large motional

electric field that in turn accelerates the ion to a very large velocity perpendicular to the magnetic field direction. Such a distribution function with a large population with high perpendicular energy is unstable to the growth of circularly polarized waves at the ion cyclotron frequency (*i.e.* ion cyclotron waves.). Referring to figure 5.1, the pick-up ions form a high energy population that is separate from the drifting "thermal" distribution of the incident flow.

These waves must be in phase with the gyrating ions to scatter some of the perpendicular energy into the parallel direction. Therefore, these waves have the ion cyclotron frequency of the high energy ions and a left-handed circular polarization. The wave accomplishes the scattering by redirecting the velocity from the perpendicular to parallel direction. It is similar to the pitch angle scattering process occurring in the Van Allen belts at Earth [*Kennel and Petschek*, 1966]. As the ions interact with the wave, the perpendicular velocity

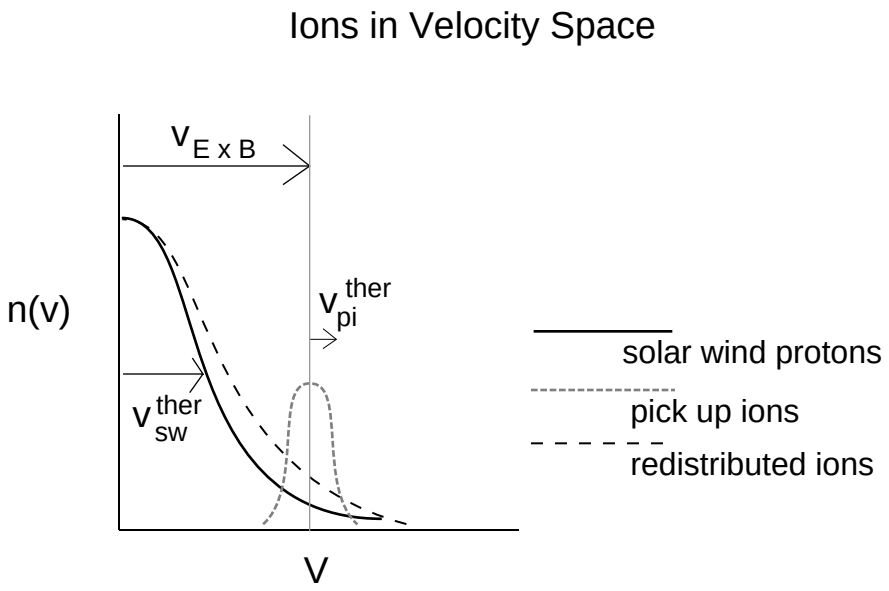

Figure 5.1 Sketch of the ion velocity distribution function of pickup ions in the solar wind flow around Mars. The solid line represents the shocked solar wind plasma (wide distribution) and the short dashed line is the pickup ions (narrow distribution). They have very high velocities and create an imbalance in the total distribution function. Ion cyclotron waves can be established to correct this distribution, forming the long dashed line distribution.

distribution is driven to a more stable configuration. Therefore, one mechanism for the waves observed in the MAG data is an unstable population of pick-up ions in the sheath. The data is consistent with a population of newborn ions produced by the ionization of exospheric neutrals.

The placement of the waves is also a clue to the physical processes involved in the MPB. Everywhere between the MPB and the bow shock, these waves consistent with ion cyclotron waves are observed. The waves usually cease at the MPB, according to MAG measurements, while the magnetic field strength increases dramatically. Therefore, it is upstream of the MPB that the unstable population exists. However, downstream of the MPB, the problem has been rectified. Either the population has been properly scattered into a stable configuration by this point or nature finds another way to treat the problem.

Now we turn to the electron fluxes to see if we can determine what process is ionizing the neutrals. Charge exchange does not affect electron energies because the reaction does not involve free electrons. Photoionization produces new electrons as solar UV ionizes neutrals. The energy of the photoelectron depends on the energy of the incident photon, but photoelectrons tend to be low in energy. The average photoelectron has 15 eV. Therefore, a signature of PI in the electron data is an increase in the number of cool electrons. Electron impact ionization (EII), on the other hand, has a large effect on the electron distribution. With each EII reaction, one electron loses at least the ionization potential of kinetic energy. Also, new electrons are being added to the plasma with a small kinetic energy. Because these three ionization processes are so different with respect to electrons, the dominant process for creating pick up ions in the dayside sheath of Mars should be evident in the signature in the electron spectra.

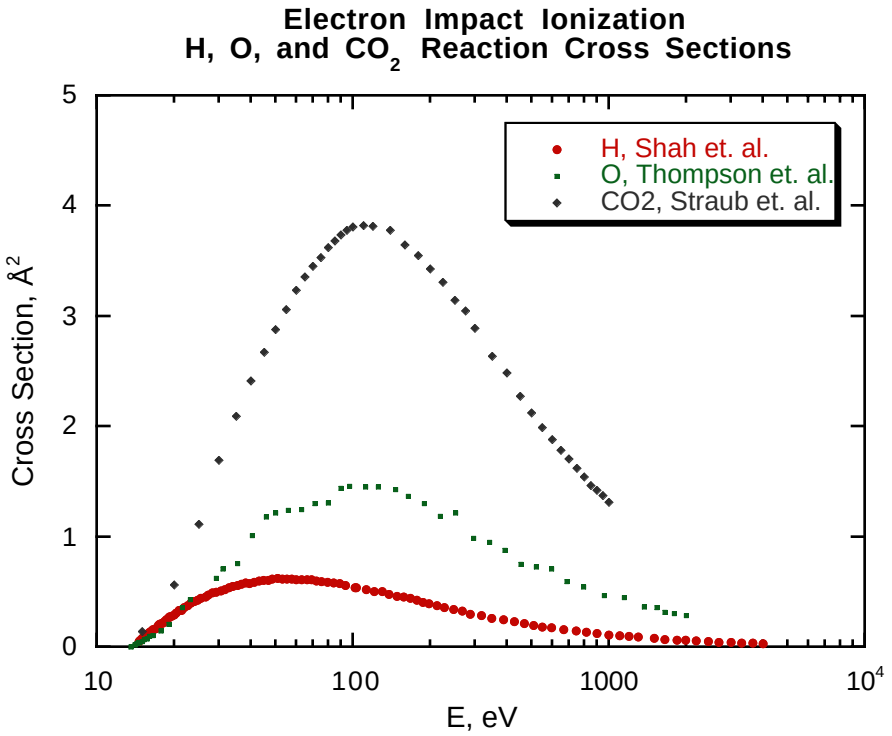

Figure 5.2 The experimental cross sections for electron impact ionization of neutral *H* (•), *O* (■), and CO_2(♦) as a function of energy. The sources for the data are in the top right corner.

The electron spectrum measured by the Electron Reflectometer shows evidence of preferential attenuation of electrons in certain energies at certain distances from the planet. The signature is constant from orbit to orbit (refer again to figure 4.10.) The high energy electrons have a slow attenuation that begins at higher altitudes. The mid-range (50-79 eV) electrons display a much sharper drop, closer to the planet. The lowest energy electrons show little to no attenuation. Looking at the cross section for electron impact ionization of *H*, *O*, and CO_2 in figure 5.2, we notice that these cross sections peak in the range of 50-80 eV. Because the electrons of those energies are affected the most, it is reasonable to suggest that electron impact ionization may be the process behind the signature.

As electron impact ionization proceeds, the distribution of electrons evolves. Impact ionizing electrons lose kinetic energy to the ionization potential of the atom and the kinetic energy of the ejected electron. The resulting distribution function reflects this by shifting electrons downward in the energy bins. High energy electrons slowly cascade down to lower energy bins as subsequent reactions cool the electrons. The reaction rate for high energy electrons is not very high, but each electron has the ability to react many times before falling below the threshold energy for reaction. That makes EII at high energy a slow, but sustainable process. On the other hand, where the cross section is the highest, there are many reactions and many electrons lost from the bin. However, the mid-range energy bins are being repopulated with the high energy electrons cascading down as well as by some secondary electrons joining the plasma. The reaction rate in this energy range is high, so the population is lost very quickly countered only by slow repopulation by cascading electrons. At the lowest energy, close to the ionization potential, the loss rate of electrons reacting out of the energy bins comes close to balancing the rate of repopulation of the low energy bins by cascading and secondary electrons. This explains the limited change in distribution in these bins. Based on EII cross sections and reaction rates, we expect that EII would affect electron distribution functions exactly as seen in the ER data.

Therefore, we hypothesize that EII is the primary physical process involved in the formation of the MPB, as seen in MAG/ER data. EII of planetary neutrals produces an unstable population of ions in the post-shock solar wind flow. The pickup ions are scattered into a stable distribution by ion cyclotron waves that are established upstream of the MPB. Evidence in the electron distribution of the EII is observed at the MPB as an attenuation of electron fluxes, especially in mid-range energy bins. As the ions and electrons cool, the thermal

pressure of the flow drops. In order to conserve total incident pressure of the solar wind, the magnetic field magnitude rises to increase the magnetic component of the pressure balance.

5.2 Model of the Electrons in the Magnetic Pileup Boundary

Now we construct a model to reproduce the electron spectra observed by the MGS ER based on electron impact ionization of a model planetary exosphere. We start with a post-shock spectrum typical of the data. Then we follow the change in the distribution of electrons due to EII of the neutral atmosphere as a flow element travels up and over the planet. Then we input the geometric considerations that determine the distribution measured at the spacecraft location.

First, we assume a form for the electron distribution function. We use the ER data for P231 to determine 18 points on the distribution function, namely, the electron distribution function calculated from the measured electron fluxes in the 18 ER energy bins. Ideally, one would use an piecewise exponential function to interpolate between these points since our 18 ER bins indicate that an exponential function or power law is apt. However, these functions must be integrated and we must later solve for coefficients in the exponential. Mathematica™ objects to this process because it "seems to use transcendental functions in an essentially non-algebraic way." Therefore, we opt for a slightly less accurate, but solvable distribution function. We subdivide the energy range into much smaller bins and approximate the distribution as piecewise constant within the bin. This requires reducing the bin size by a large amount to retain accuracy. The initial values in the new bins are chosen by assuming a piecewise exponential function between ER bins and calculating a starting value for each of

the small bins. All calculations are performed on the small bin size functions. They are only rebinned to the ER bins for plotting.

We follow a flow element along its streamline around Mars. We choose the flow elements that start north of the magnetic equator and follow the magnetic noon line. The flow velocity must be assumed. We begin with the flow given by the Spreiter and Stahara model [*Spreiter and Stahara*, 1980] (see figure 2.2). This model does not include any velocity shear close to the ionosphere. Instead, the model uses a hard obstacle as its lower limit. Realistically, though, there is a large shear in the velocity field at the ionopause. Typical flow velocities above the ionopause are > 50 km/s. However, the flow velocity in the ionosphere is under the escape speed, ~5 km/s.

As the flow element progresses, we determine the evolution of the electron distribution function. The reaction rate for all electron impact ionization reactions is calculated for each step along the flow for each energy bin for each neutral constituent. The reaction rate, ν, is given by a convolution of the cross section for interaction and the electron flux:

$$\nu = \int_0^\infty 4\pi v^2 \sigma(v) f(v) v \, dv$$

where $f(v)$ is the distribution function, $\sigma(v)$ is the cross section, and v is the relative velocity. Using the piecewise constant basis functions, the reaction rate by energy bin, *j*, is:

$$\nu_j = \pi \sigma_j f_j \left({v_{1j}}^4 - {v_{0j}}^4 \right)$$

In this calculation, the distribution function is given. The relative velocity should be the superposition of the electron thermal velocity and the local flow velocity. However, the thermal velocity of the electrons is much higher than the local flow velocity which is much higher than the neutral velocity in the planetary exosphere. Therefore, we can substitute the thermal velocity for the relative velocity. Finally, we need the EII reaction cross sections for the different neutral

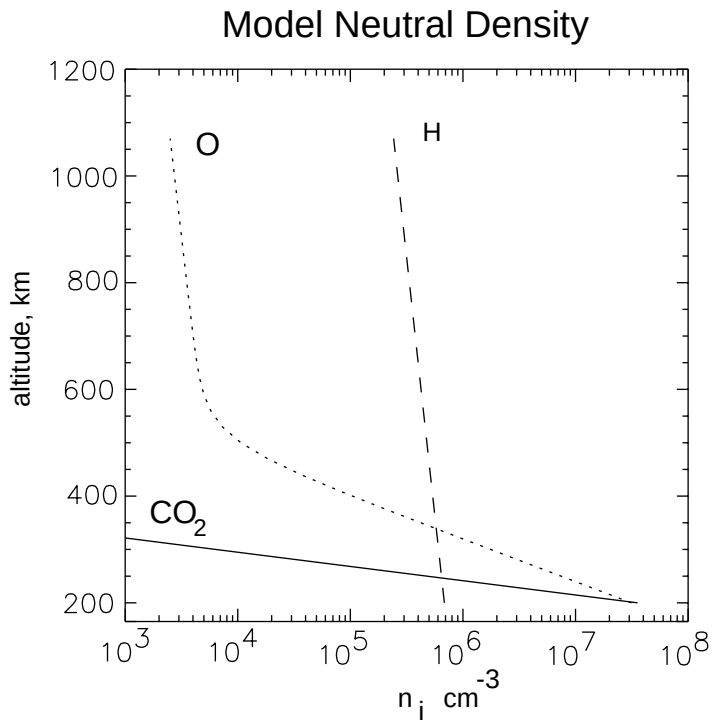

Figure 5.3 The model neutral atmosphere used to calculate ion production rates. These values are generalized from the different conditions presented in *Kim et al.* [1998] and *Shinigawa and Cravens* [1989].

atoms and molecules. They are taken from experimental data. Cross sections and fractional cross section for daughter ions from $e^- + CO_2$ are from *Straub et al.* [1996]. Cross sections for $e^- + O$ are from *Thompson et al.* [1995] and those for $e^- + H$ are from *Shah et al.* [1987].

The ion production density then is found by the product of the reaction rate, the effective neutral density, and the time step:

$$P_n dt = n_n dt \int_0^\infty 4\pi v^2 \sigma_n(v) f_n(v) v \, dv = n_n \nu_n dt$$

where n_n is the neutral density of species n and dt is the computational time step. For this step, we must make an assumption about the neutral density. We use a conglomeration of the neutral exosphere of the Michigan group [*Kim et al.*, 1998; *Nagy et al.*, 1990] and the low altitude model of *Shinigawa and Cravens* [1989] as a foundation for the neutral atmosphere. Our model is presented by altitude in figure 5.3. However, the atmosphere at Mars has proven to be highly

variable [*Keating et al.*, 1998]. We expect that one set of atmospheric conditions will fit one orbital pass, but not all passes. Therefore, we allow hefty departures from the model atmosphere in our calculations. This is another parameter that we find our model is capable of constraining. Although we currently have no ion data with which to compare our results, we hope that future Mars missions, *e.g.* Planet B, will provide ion data for comparison.

Next, the amount of energy lost from the electrons is counted. Regardless of how the kinetic energy of the incident electron is divided between the resulting electrons, only the ionization potential energy is lost. However, the total energy is spread over more electrons due to the production of electrons by impact ionization.

Then, the new distribution function is calculated by redistributing electrons. Using a piecewise constant $f(v)$, this calculation is trivial. We know the number of electrons in each energy bin after one time step is given by the number before, less those within the bin that react during the time step, plus the electrons that cascade into the bin from a reaction from above, plus those the number of secondary electrons created in that energy range:

$$n_{e_j}(t+dt) = n_{e_j}(t) - \nu_j(t) n_n dt + \sum_{i=i_\chi}^{i_{\max}} \nu_i(t) g_{ij} n_n dt$$

where g_{ij} is the function that gives the fraction of the cross section that results in an electron's kinetic energy landing in bin *j* after reacting out of bin *i*. Because the distribution is defined such that its integral over velocity space gives the electron density:

$$n_e \equiv \int_0^\infty 4\pi v^2 f(v)\, dv$$

or by bin:

$$n_{e_j} = \frac{4}{3}\pi f_j {v_{1j}}^3 \left(1 - \frac{{v_{0j}}^3}{{v_{1j}}^3}\right)$$

the new distribution can be calculated using the new number of electrons in each bin:

$$f_j(t+dt) = \frac{3n_{e_j}(t+dt)}{4\pi\left(v_{1j}{}^3 - v_{0j}{}^3\right)}$$

The new distribution function goes on to be the starting point for the next time step.

Before proceeding, we look further into the function g_{ij} that gives the fraction of electrons cascading from bin *i* to *j*. We try three algorithms for determining the division of energy between the primary and secondary electrons. The first is to assume the secondary electron has zero energy. Conserving energy, the primary electron loses just the ionization potential from its kinetic energy:

$$W = 0.$$
$$E = T - \chi$$

where T, E and W are the kinetic energy of the incident, the primary, and the secondary electrons, respectively. χ is the ionization potential. This keeps the number of reacting electrons about the same. The new electrons produced do not have enough energy to react so they do not need to be considered. The primary electron cascades down slowly with each reaction, reacting $T/\chi - 1$ times before falling below the threshold.

However, on the other extreme, one can divide the energy evenly between the two electrons. This turns out to have quite an interesting effect on the process. It speeds it up tremendously. Instead of having one electron slowly cascading down in energy as it reacts, there are two electrons that move from a region with a low cross section for reaction to an energy range where the cross section greatly increases. So once the first reaction occurs at high energies, the electrons react very quickly and multiply. The same net number of ionizations

occur and the same amount of energy is lost. However, the character of the spectrum is vastly different.

The truth lies somewhere in between the two extremes above. *Kim and Rudd* [1994] developed a model for the differential cross section, which is the cross section per energy of the secondary electron. Little has been done is measuring the differential cross for any electron impact reactions, except, *e.g.*, the experiment by *Shyn* [1992] on hydrogen. Their results indicate that the secondary electrons tend towards taking no energy from the primary electron, but some exchange does occur. Kim and Rudd's model reproduces these results quite nicely for hydrogen, especially at higher secondary electron energy. Unfortunately, their model relies on knowing the oscillator strengths for the neutral atom very well. So the model can only be applied so far as the oscillator strengths are known. Figure 5.4 contains the differential cross section they calculate for hydrogen for two different incident electron energies. The fractional cross section is the fraction of the total cross section for the incident electron's energy as a function of secondary electron energy. The example plotted in figure 5.4 is the fractional differential cross section for a 200 eV and 1 keV incident electron. Notice that the fractions are nearly identical at low energy regardless of the incident energy. Here, it is obvious that most secondary electrons take less than the ionization potential in kinetic energy.

The model has now calculated the EII reaction rate by neutral species by energy bin, the ion production by daughter species by electron energy bin, the total electron energy lost, and the electron distribution function by energy bin. Any of the parameters can be rebinned to the original 18 ER energy bins to compare with MGS data. However, at this point, the position of the spacecraft must be considered. The model calculates the effects of electron impact ionization on the distribution of electrons in energy along a flow line. We must

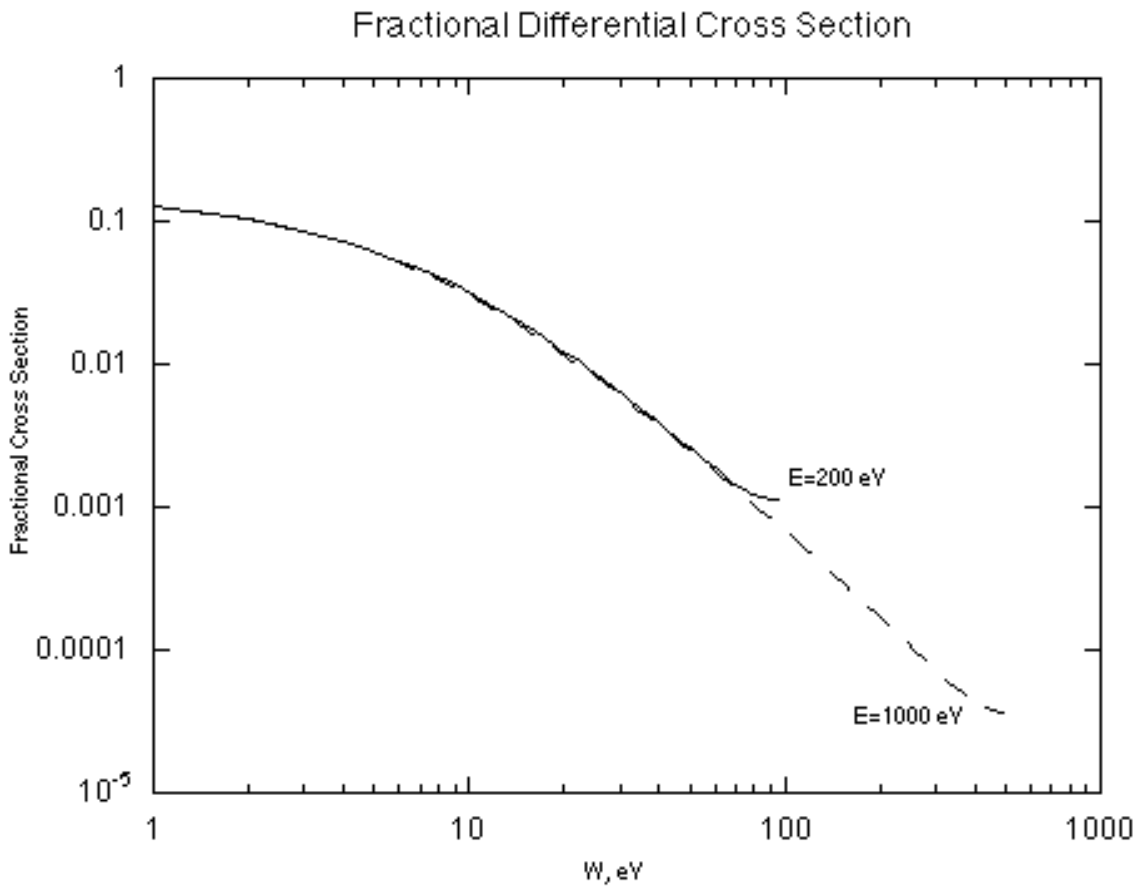

Figure 5.4 The fractional differential cross sections for *H* from *Kim and Rudd* [1994]. The two lines show the differential cross section for secondary electrons of energy *W* for two incident electron energies. The solid line is for E_i = 200 eV and the dashed line is for E_i = 1000 eV.

determine the correct flow line to inspect and what position along the streamline. It is in this step that we consider the geometry of the MPB.

The local flow speed is slow--in the range of tens to a few hundred km/s. However, the electron thermal velocity is much faster. A 10 eV electron has a thermal speed of 1325 km/s and a 1 keV electrons travels at 10 times that, 13,250 km/s. These electrons, having gyroradii of < 2 km in the typical magnetic field strengths of the sheath, travel along magnetic field lines at their thermal speed while the magnetic field lines move through the sheath at the flow speed. So the electrons travel a long way along a magnetic field line in the time the flow moves only a short distance. Therefore, the electron distribution measured at the

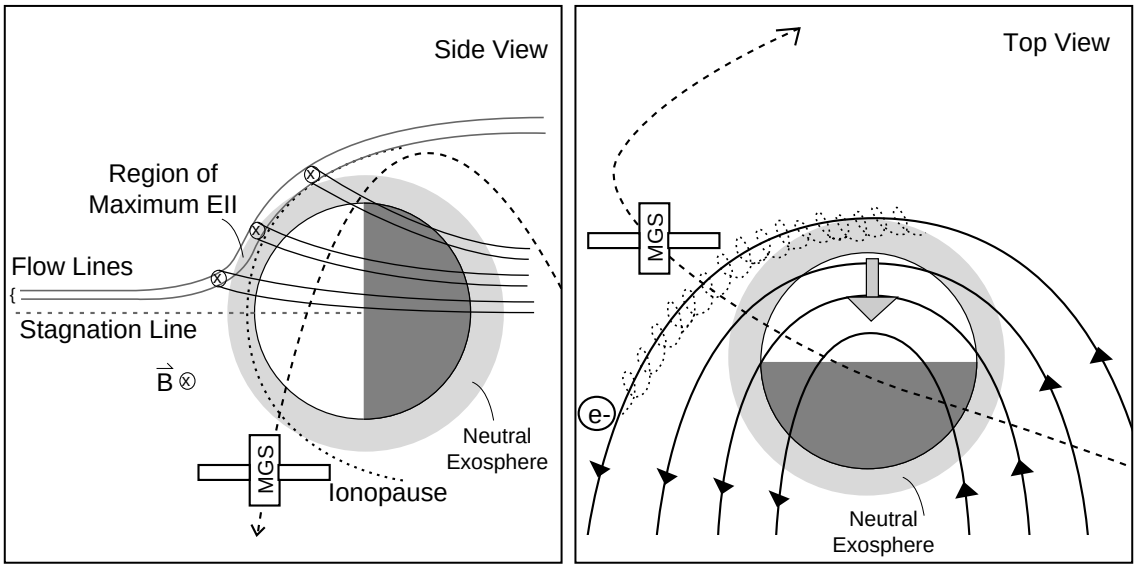

Figure 5.5 Cartoon of the how the spacecraft remotely measures electron impact ionization reactions at the magnetic noon line. Electrons are tied to the draped magnetic field lines. Their thermal speed is much faster than the flow speed. So the spacecraft is effectively measuring a composite distribution function of electrons all along the magnetic field line. Electron impact ionization reactions at the lowest altitude of the field line (and the highest neutral density) show up as an attenuation of electrons, especially at the energy range where the cross section for EII is a maximum. The flare of the ionopause is shown, demonstrating how a flow line can rise above the high neutral density at higher solar zenith angles.

spacecraft location results from processes occurring along the extent of the magnetic flux tube. The distribution is not necessarily a result of local flow parameters and phenomena.

Therefore, we consider the magnetic field geometry (see figure 5.5). If there is any net inclination to the draped magnetic field lines, then the electrons being sampled by the spacecraft have seen a range of altitudes, including down to the lowest altitude to which the magnetic field line is connected. Therefore, when looking at positions in the flow off of the magnetic noon line, it is not the

neutral density at the spacecraft position that one must use. Instead, an average neutral density over the traverse of the magnetic field line.

The model follows the flow element along the lowest altitude of the magnetic field line. The change in neutral density is exponential with altitude. Compared to the amount of time spent at the lowest altitude of the flow, the reactions along the field line at higher altitudes are inconsequential. Therefore, we compute the evolution of the spectrum due to reactions at the lowest altitude. The actual integral neutral density seen can be factored in by geometric considerations.

Finally, we assume that electron impact ionization is the only process affecting the spectrum of the electrons in the space covered. The density and distribution function are constant upstream and match the measured post-shock distribution from the ER. Therefore, any MHD effect that changes the electron pressure, temperature, and density is not included in this model.

6. Model Results

Now we present the results of several different runs of the model. We use the starting spectrum from several different orbits and attempt to reproduce the electron distribution observed by the ER. In addition, we isolate the effects of certain assumptions we make in the model. Six cases are described below with a summary of the results in the final section of this chapter.

6.1 Case 1--Investigating Effects of Differential Cross Sections

We run the model with several different parameters to more completely analyze the magnetic pileup boundary. Our first set of runs are at a constant neutral density to determine the effects of changing the differential cross section. In figure 6.1, the three panels display the results from the three cases described above. All cases are run at a constant altitude of 325 km.

The left hand panel shows the effect of a constant neutral density when the secondary electron emerges with no kinetic energy. The middle panel shows the evolution of the spectrum under the same neutral conditions, but when the primary and secondary electrons divide the kinetic energy up between them equally. The results are striking. Not only is the shape of the spectrum changed, but also the time of reaction. The left hand panel is the evolution of the spectrum over 212 s. In panel b, the lowest spectrum is achieved in only 42 s. The time cut by 1/5 to achieve the same level of attenuation as panel a. As discussed in section 5.2, the equal division of kinetic energy between the 2 electrons, as in panel b, increases the number of electrons in the energy range of highest reaction cross section, increasing the reaction rate.

In panel c, the *Kim and Rudd* [1994] distribution is used. There, the results show that there is not much of a difference from the W=0 approximation

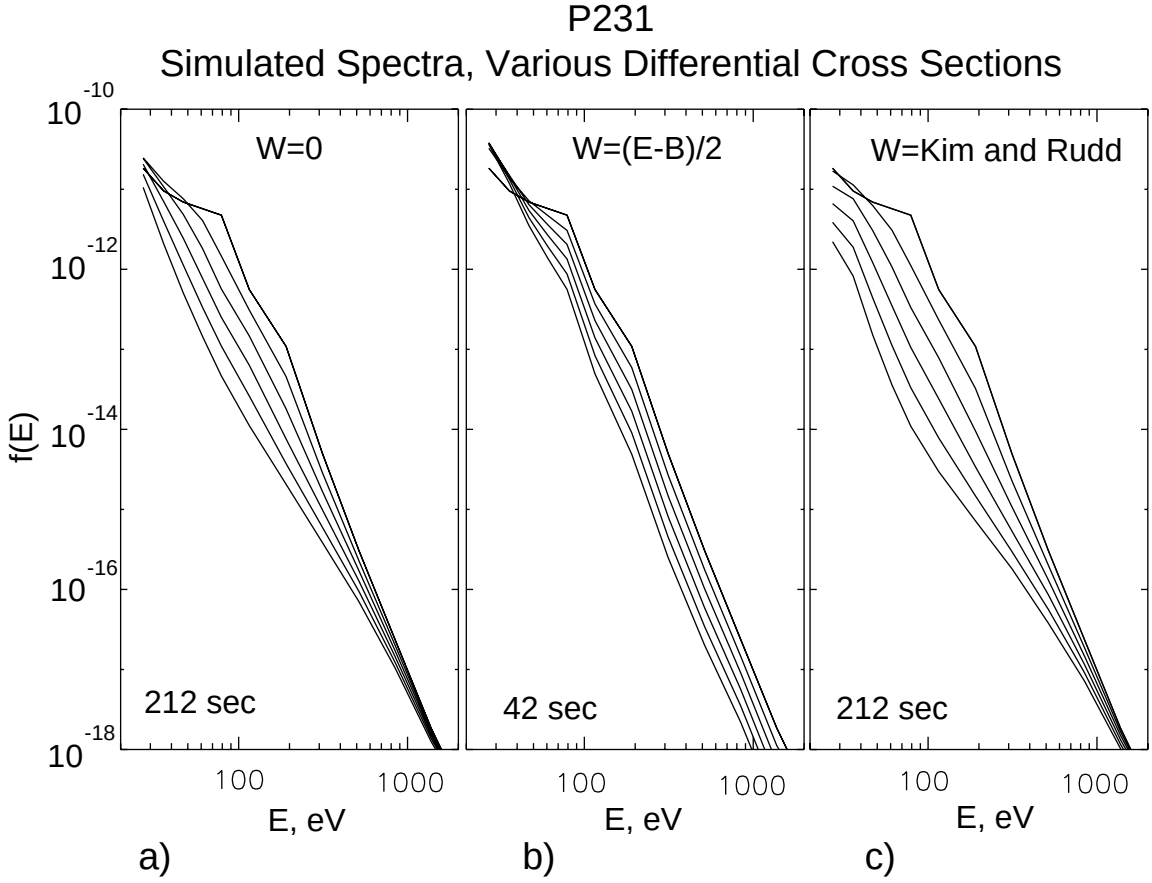

Figure 6. 1 The effects of different choices of energy division between the two resultant electrons from EII reactions on the evolution of the electron distribution function. The panels are: a) the primary electron retains all of its kinetic energy, except the energy that went into the ionization potential of the neutral; b) the kinetic energy is equally divided between primary and secondary electrons; c) the *Kim and Rudd* results are used.

except at low energy. Because the fraction of secondary electrons produced above the threshold energy is less than 30%, the secondary electrons do not contribute much to EII reactions. Further, the primary electrons retain close to their initial kinetic energy, less the ionization potential and 5 eV, on average. For this simulation, one cascading keV electron reacts a couple fewer times than the same electron in the panel a simulation. However, it completes its reactions faster than the keV electron in the panel a simulation, due to the same principle at work in the panel b simulation. Therefore, after the same time through the

same atmospheric conditions, the Kim and Rudd differential cross section causes a slight increase in attenuation and a change in spectral shape at $E < 40$ eV.

6.2 Case 2--Investigating Contributions from Individual Neutral Species

Now, we isolate the effects of the individual neutrals. Although finding the exact admixture of neutral particles is infeasible, we can deduce the dominant neutral constituent and an integral neutral density by investigating the individual effects of the different neutrals. Figure 6.2 shows the spectral evolution for a post-shock distribution due to H, O, and CO_2. Each panel uses only one constituent, begins with the same initial spectrum, and takes the same size time step through a constant neutral density. Each line shown is the result of reactions after passing through $\int n_n dt = 5 \times 10^7 \ {}^{s}\!/_{cm^3}$ of neutral particles. The bottom line for each panel is the result of $35 \times 10^7 \ {}^{s}\!/_{cm^3}$ neutrals.

In figure 6.2, the left panel shows the shape of the spectrum due solely to interactions with neutral hydrogen. Since hydrogen is the major neutral constituent at high altitudes (≥ 350 km), spectral evolution of this form would be indicative of reactions at a higher altitude. Most of the attenuation in this case is towards low energy. From figure 5. 2, ones sees that the peak cross section for hydrogen is near 50 eV. This is lower than the peaks for the other two neutrals. At high energy, the all H simulation does not decrease much from the original values.

There is a ~150 km altitude range in which atomic oxygen is the dominant constituent. The middle panel of figure 6.2 isolates the effects EII of oxygen has on the electron distribution function. The O simulation manifests some points of interest. First, the reaction rate has increased from H. The cross section for reaction is about twice that for H. Also, the energy at which the distribution is

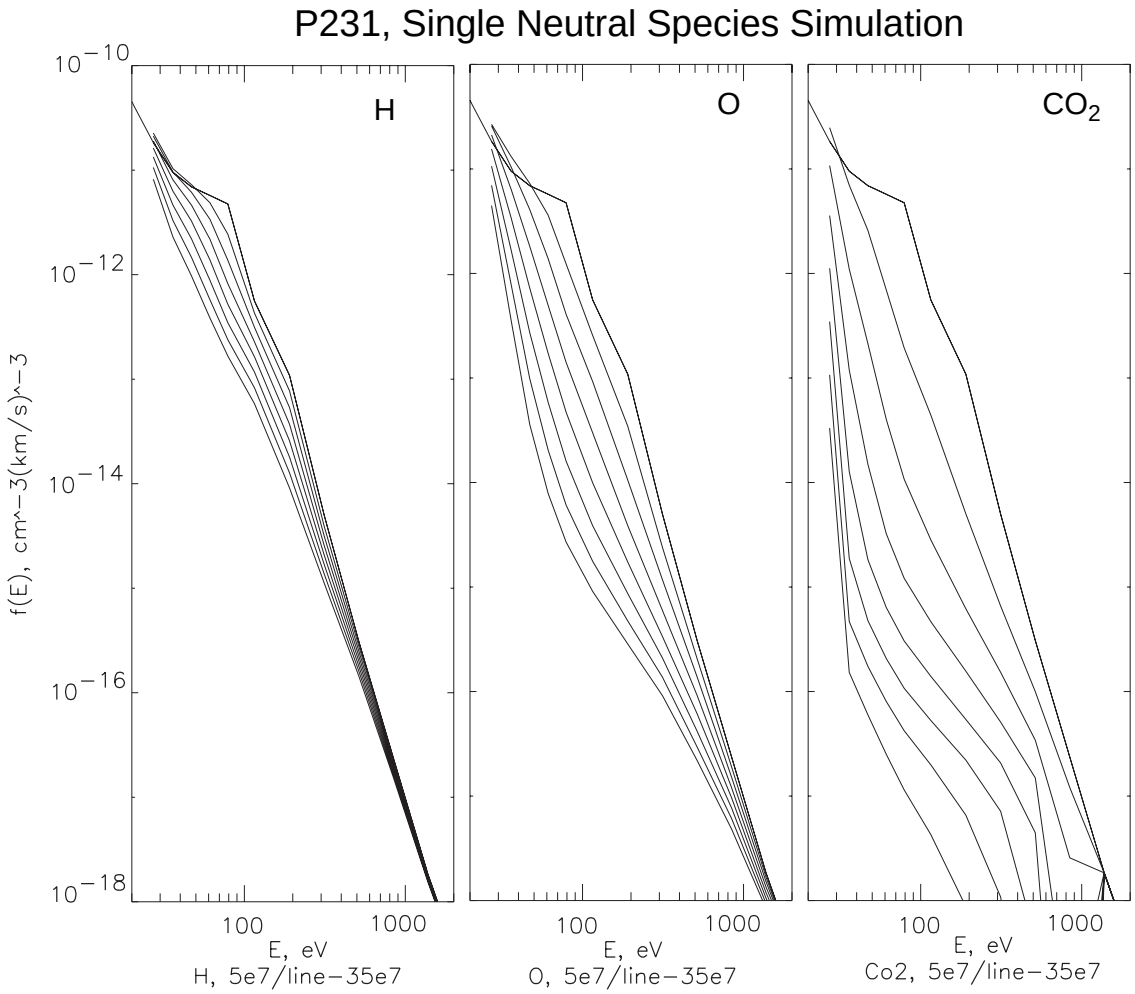

Figure 6.2 The individual effects of the 3 neutral constituents on the original post shock spectrum from P231 (from left to right--*H*, *O*, CO_2). Each simulation starts with the same spectrum. Each line represents the resulting distribution of electrons after passing through an integrated neutral density over time of 5 x 10^7 s/cm^3. There are 7 lines, showing the total after 35 x 10^7 s/cm^3 of each neutral constituent.

affected most increases from that of the *H* simulation. Here, attenuation is strong for $E < 300$ eV and is a maximum at 80 eV.

In contrast, CO_2 is the dominant neutral at low altitudes ($\leq$ 200 km). CO_2 has a cross section for electron impact ionization that is about 4 times that of *H*, so the neutral density does not need to be as high for this reaction to go at a comparable speed. The simulated spectra appear in figure 6.2 rightmost panel. The top three lines of figure 6.2 c are the signature of CO_2 at work on the

electron distribution. The rest is included to have equal time steps for the different simulations. The CO_2 spectrum does not deviate as much, relatively, at the lowest energies displayed here. However, the attenuation is drastic over the energy range of 50 - 1000 eV.

6.3 Case 3--Modeling the Spectra from P231

We finally attempt to reproduce the observed spectra from MGS data. First, we use the results from individual neutrals to get an idea of the altitude of the interaction region. In figure 6.3, we show that the post-MPB spectrum can be obtained by a simulation of only neutral hydrogen. The results of the simulation are the (❋) symbols on the plot. The simulation used the solid line as the input post-shock spectrum. It is an average post-shock spectrum for P231 taken from the data. The dashed line is the measured spectrum downstream of the magnetic pileup boundary. After $4.3\times10^{8}\ {}^{s}\!/_{cm^3}$ of *H*, the simulated spectrum matches the dashed line very well. This indicates that the interaction region is well above the CO_2 atmosphere.

This result implies that the integral of neutral hydrogen density along the flow line aver time is on the order of a few times 10^8. Using a flow speed from the sheath of 50 km/s and a neutral density of $6\times10^{6}\ {}/_{cm^3}$, we find that the flow has traveled 55° around the planet at an altitude of 350 km to achieve this integral measure. In magnetic coordinates, however, the MPB occurs very close to the magnetic equator in this orbit. So the requirement of 55° of travel contradicts the observations. However, if the flow speed is reduced to a speed much closer to the ionospheric flow speed, *e.g.* 10 km/s, the travel distance is reduced by a factor of 5 to 11°. That result is far more reasonable given the measured location of the boundary. Therefore, we conclude that the MPB, as

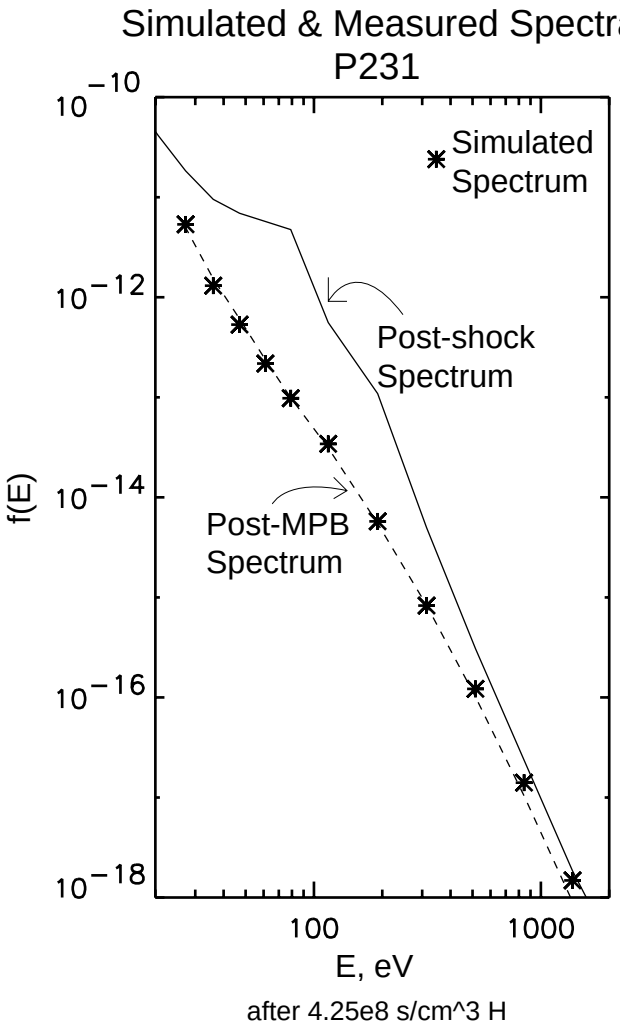

Figure 6.3 Simulation to determine the integral neutral density necessary to reproduce the attenuated spectrum at the bottom of the MPB. This simulation shows the measured pre-MPB spectrum which is the model input (top--solid), the measured post-MPB spectrum (bottom--dashed) and the model output (✳).

seen in the electron fluxes, is formed in the shear layer where flow velocities are reduced.

Now, we implement geometry considerations to trace spacecraft location to the magnetic noon flow line position. First, we run the model on several flow lines starting at 1000 km altitude at y=0 and various latitudes. The solar wind flow speed is assumed to be 300 km/s for the run. A simple velocity shear model slows the tangential component of the velocity in a layer 50 km thick to 5 km/s at

275 km. Then, we inspect the position of the spacecraft in magnetic coordinates. The MPB in P231 is at very low magnetic latitudes and solar zenith angle of near 45°. To map the coordinates of the spacecraft to where magnetic flux tubes cross the magnetic noon line we perform the following transformations. First, we assume the lowest altitude of the MPB maps to a subsolar altitude of 275 km. Then we scale the altitude of the other points in the MPB such that the thickness at noon is $\sqrt{2}/2$ of that at 45°. Further, to account for the spreading of magnetic field lines in latitude, the latitude of the coordinates along noon is twice the spacecraft latitude.

Finally, plotting the model results from the positions mapped from the spacecraft position, we obtain the simulated time series electron data in figure 6.4. The calculated electron distributions for 13 energy bins above the threshold energy of the reactions are plotted. The points beginning at 30 begin the points corresponding to the shaded region in figure 4.2. The lowest energy fluxes are barely affected by the model, like in the data. Here, a slight increase is seen in the counts in the 15.4 energy bin. This is the result of secondary electrons populating that energy bin. In the simulation, the attenuation in flux begins at later times with increasing electron energy, which also resembles the data. Further, the size of the drop from start to finish agrees very well with the measured values, for most energy ranges.

However, the simulations indicate that the electron distribution time series is concave down at all energies and times until the distribution reaches the post-MPB spectrum. In contrast, the data exhibit a concave down behavior at $E <$ 100 eV and concave up at higher energy. Also, even the low energy traces show a point of inflection, where at lower altitude (earlier time) the distribution turns to concave up. This difference appears to be the effect of our model lacking a flare to the ionopause shape. *Knudsen et al.* [1982] show that the ionopause at Venus

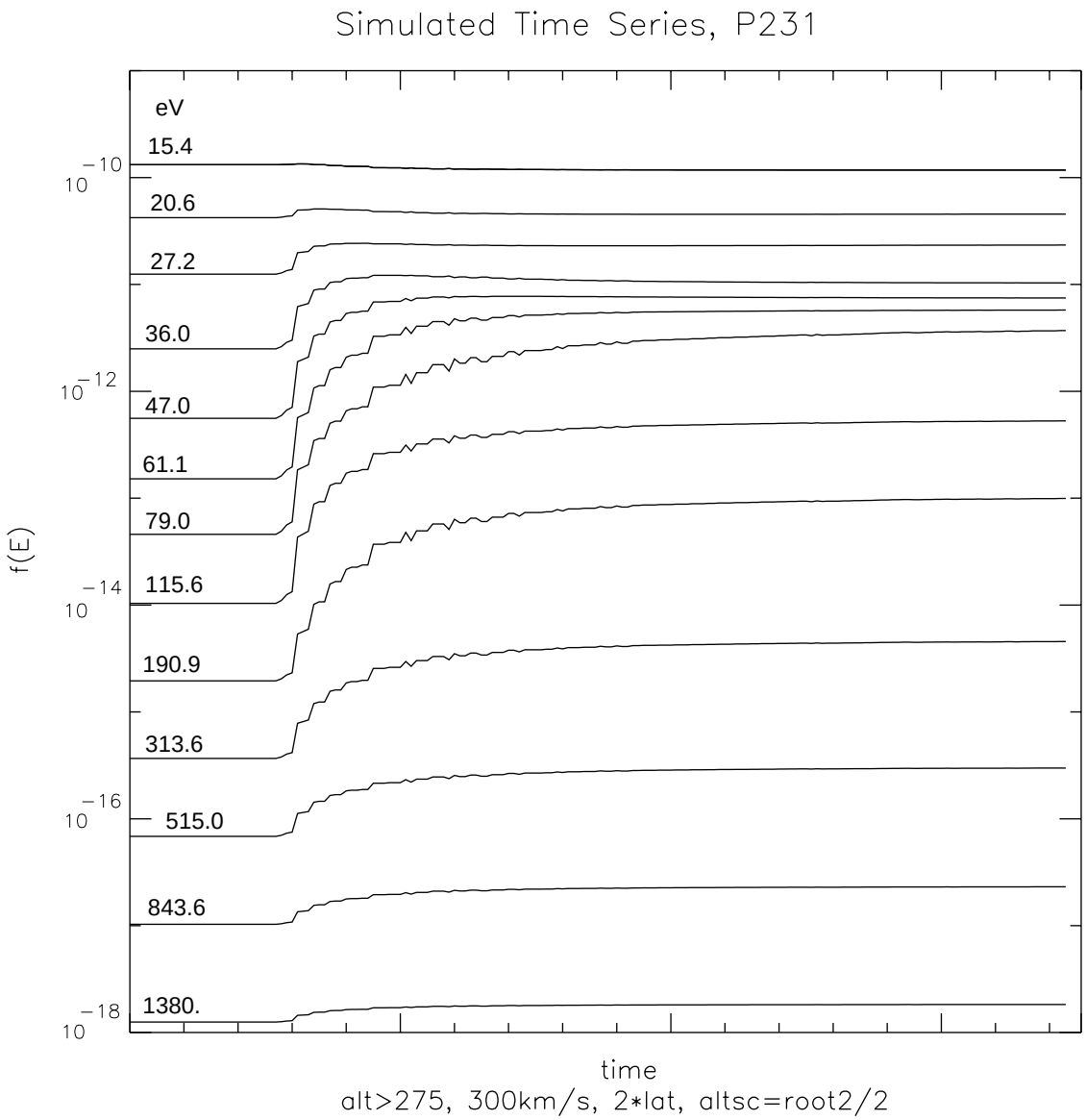

Figure 6.4 Simulation of the time series electron distribution function for P231. The model results are mapped to the spacecraft position throughout the MPB by scaling the latitude by a factor of two and scaling the altitude by .7. The minimum altidude for the flow is 275 km in this simulation with the solar wind speed at 300 km/s.

has a altitude at the terminator 3-5 times higher than at the subsolar point. If the lowest altitude magnetic field line is following along the top of the ionosphere, it would rise above the high density region as it goes to higher magnetic latitude. Increasing the altitude decreases the neutral density and decreases the production rate. The change in rate affects the slope of the time series.

Therefore, we conclude that the implementation of a flare to the velocity flow model that would reproduce the effects of a magnetic field line skipping along the ionopause would correct this difference.

Although the two traces are qualitatively the same, a direct comparison would show that the model does not provide a quantitative good fit to the data. It is possible to adjust all of the input parameters available to our model and all of the mapping parameters to get an exact fit. However, we do not do this because it would not provide any more information than our current results do. Our results are extremely model dependent. The error in the models is sometimes estimated to be an order of magnitude [*Nagy*, private communication]. Even so, we are able to make some reasonable assumptions about the parameters and qualitatively reproduce the data. With so much parameter space available, it is more an exercise in logistics than in science to pinpoint a combination that has a good fit. Further, with as dynamic of an interaction as the solar wind interaction with Mars, we expect the parameters to evolve continuously. Therefore, one cannot compare the parameters found for different orbits to establish a universal solution in the parameter space.

6.4 Case 4--P236 Simulation

For P236, we perform another simulation. This orbit has a very similar geometry in magnetic coordinates to our original example. Our input parameters for this simulation are the average post-shock spectrum of P236, a solar wind speed of 300 km/s and a subsolar ionopause altitude of 275 km. Then, we extrapolate the model results to the spacecraft position. Figure 6.5 contains the original time series data and two different mappings of the model results for 9 energy bins. The middle panel is the measured distribution. The two simulations are the same in every way except the altitude scaling factor. Both map the

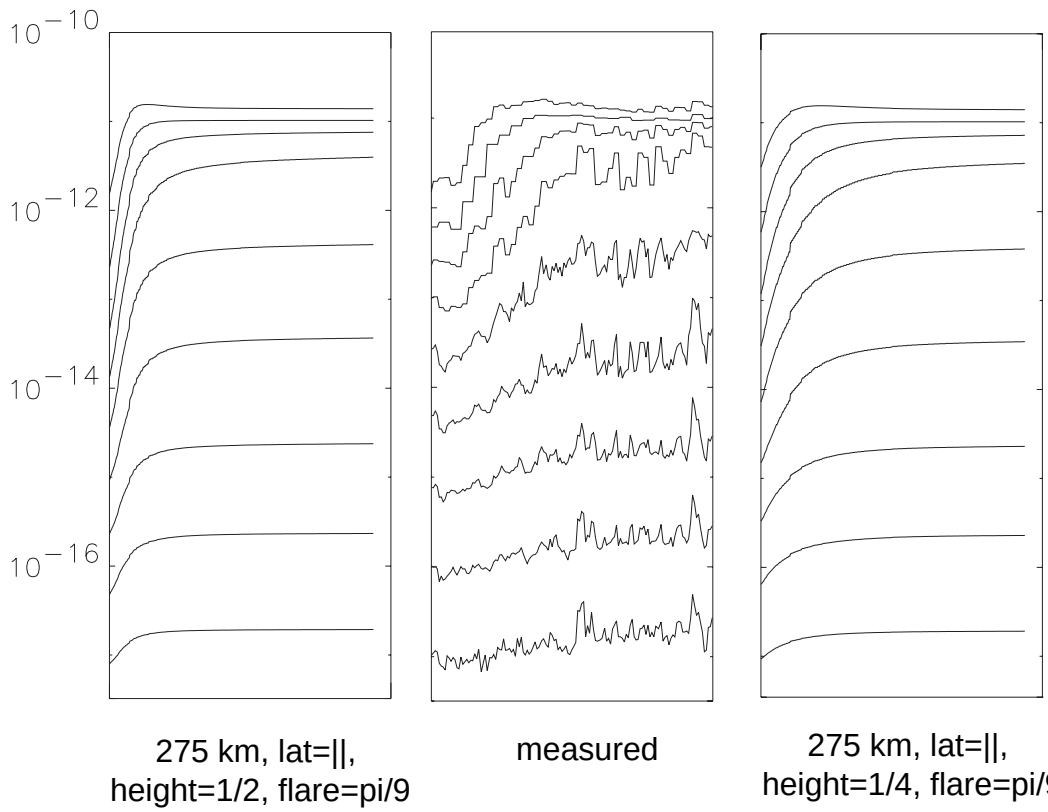

Figure 6.5. Simulated time series for P236. The center panel shows the measured distribution for energy bins 30 eV < E < 1 keV. The left and right panels show attempts to recreate the time series using the model and different geometric assumptions. The difference between the right and left panels is that the right panel scales the observed region to a smaller magnetic noon altitude range than the left panel.

latitude of the spacecraft exactly to latitude along noon. Also, both place the lowest altitude of the MPB at the ionopause height. However, the left panel shows the results of a realistic scaling of the thickness of the region. Using that the thickness at 45° scales as twice that at 0°, we obtain the results shown. Here the attenuation is far too steep. In order to get a better match to the slope, we assume a more extreme scale factor of 4. This still does not quite match the loss rate measured at the spacecraft position.

Although we are adjusting the thickness scale parameter in our mapping geometry to correct this problem, altering the neutral density scale height would have the same effect. If the region of high density were spread out over a larger region, we would not have to make such drastic assumptions on our scaling factors. Because the MPB appears to form near the altitude where the exospheric scale heights begin to dominate, it is very reasonable to assume the discrepancy comes from this term.

6.5 Case 5--P257 Simulation

The orbital geometry is somewhat different than the previous two examples for P257. Here the MPB is observed at latitudes of just less than 30°, which is higher than the previous two trials. Hence, there is more room for the MPB to develop than in our other examples. So we relax many of the input parameters. We run the model using a minimum altitude of 325 km and a solar wind speed of 400 km/s. To map the results to the spacecraft location, we maintain the same latitude, but scale the thickness of the region by 4. Note that choosing to scale the latitude by 1/2 is also an option. That even further relaxes the area needed to produce the attenuation because it allows the flow line to travel to latitudes of near 60°. However, we choose to scale by unity because a flared boundary forces the flow line to higher altitudes at higher latitudes.

We compare the model output for the P257 simulation to the measured distribution in figure 6.6. Here again, the model tries to make too steep of a slope in the distribution. Also, the magnitude of the attenuation in the simulation is higher than in reality at low energy. The data is quite wavy, making direct comparison troublesome. However, on average, the model does an excellent job of reproducing the data.

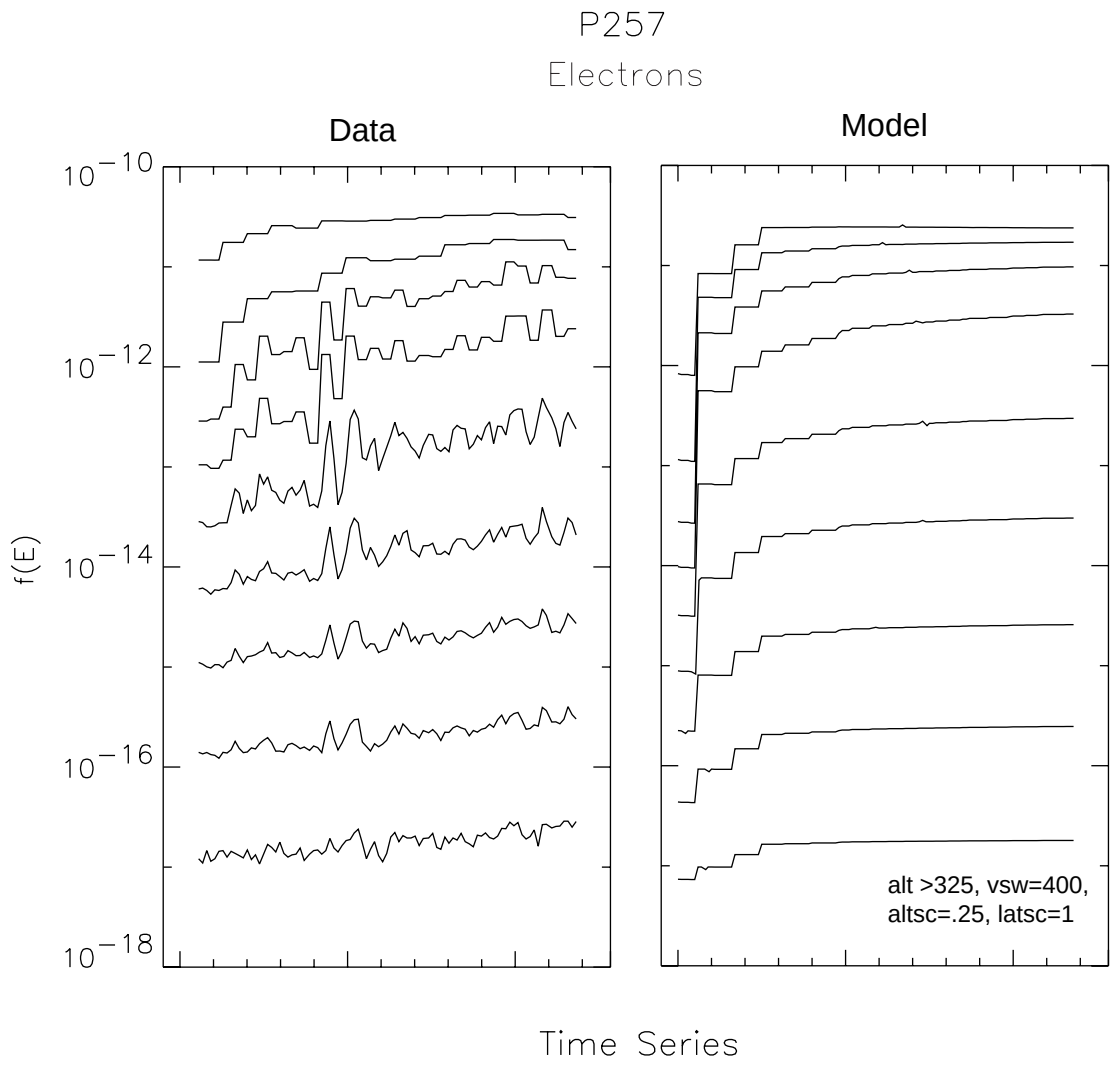

Figure 6.6. Simulated (right) and measured (left) electron distribution time series for energy bins 30 eV < *E* < 1 keV.

6.6 Case 6--P456 Simulation

Finally we attempt to reproduce the electron data for the high field case, P456. Recalling figure 4.9 from the previous chapter, the magnetic pileup boundary is quite spread out in this case. Due to the high incident solar wind pressure accompanied by a magnetic field strength 4 times the typical values, the electron fluxes are elevated at all energies. The elevated fluxes are magnified by the bow shock, increasing the post-shock distribution function by about an order

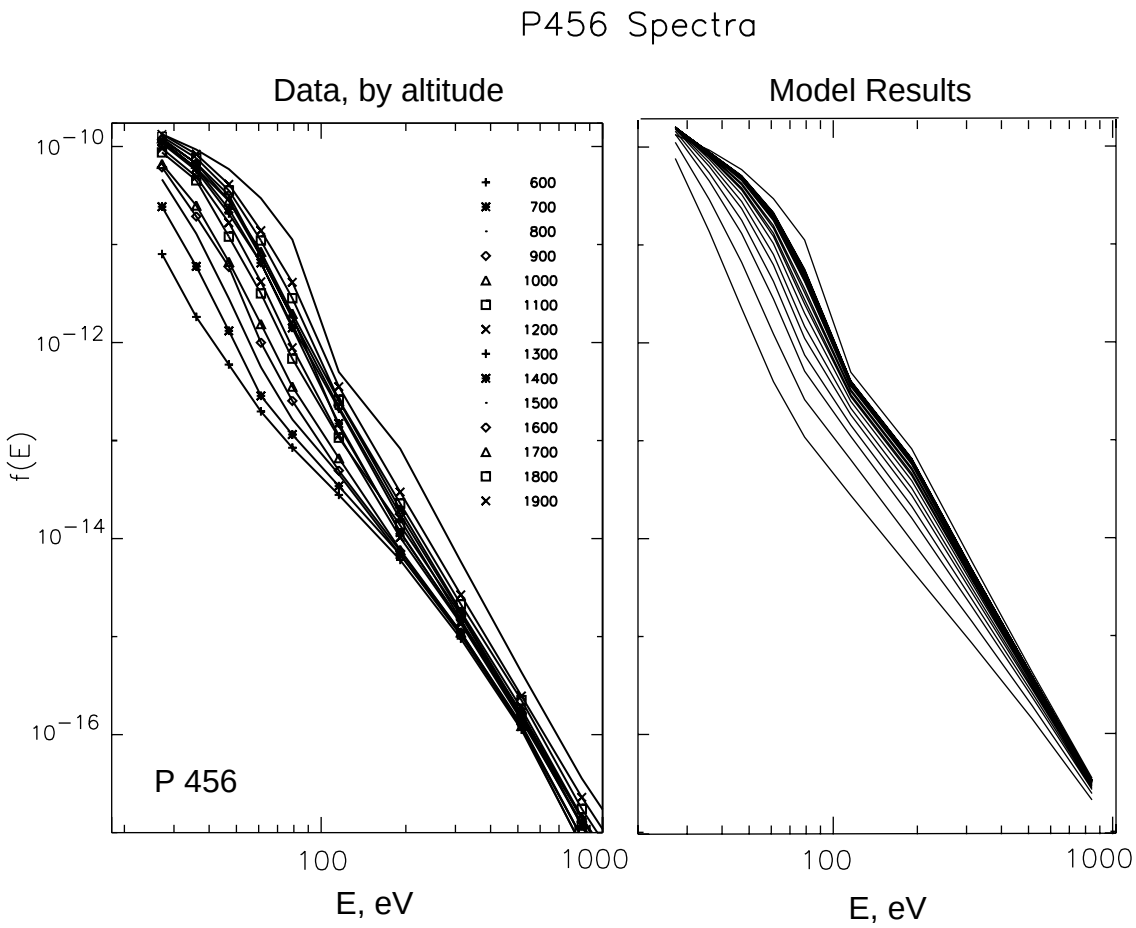

Figure 6.7. Measured (left) and simulated (right) spectra for P456.

of magnitude over normal values. The result is an increase in the reaction rate for electron impact ionization.

We model the electron distribution for this case using an average, measured post-shock spectrum. We then follow flow lines assuming an incident solar wind speed of 400 km/s and a minimum altitude of 300 km. We demonstrate the spectral evolution predicted by the model in figure 6.7. The measured spectra are shown for reference in the left panel. Clearly, the model is doing a good job of reproducing the data, especially at $E > 50$ eV. At $E < 50$ eV, the model does not reproduce enough attenuation in the distribution. Recall, however, the results from Case 1. Using different assumptions in the distribution

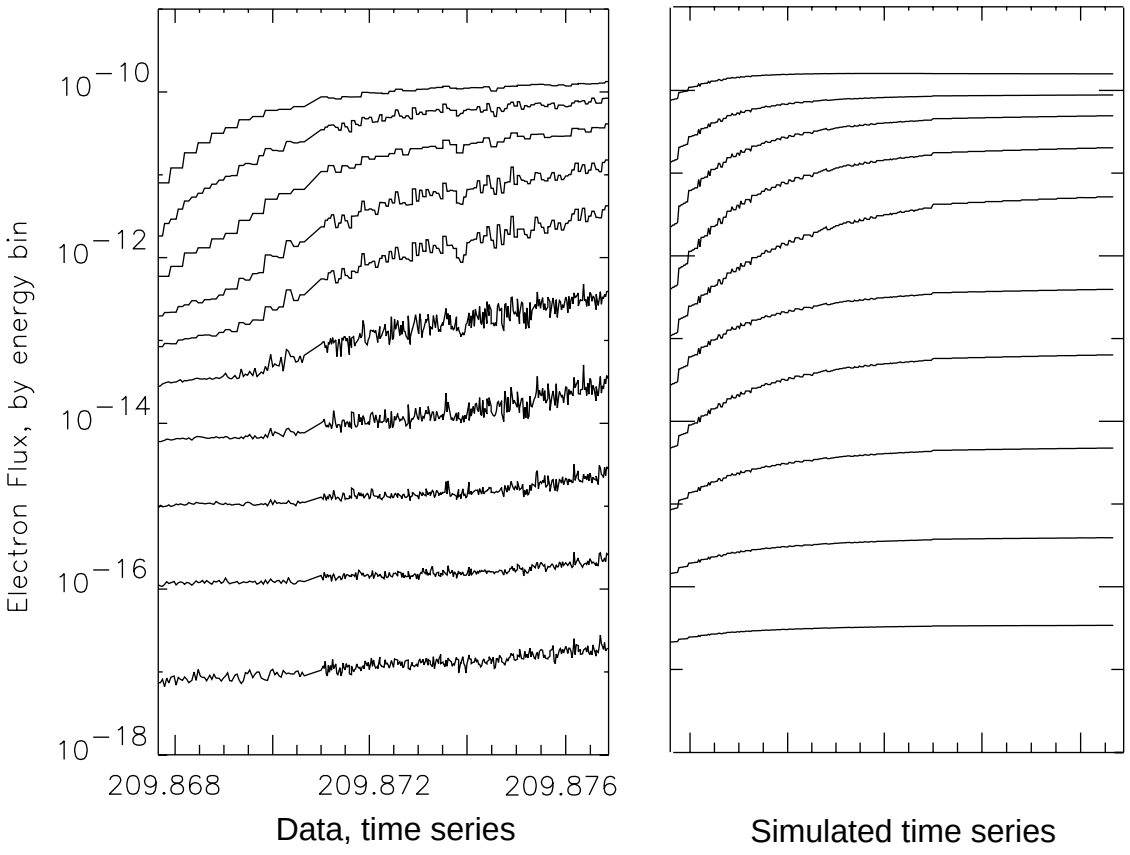

Figure 6.8. Measured (left) and simulated (right) time series for P456. Large compression of the MPB thickness from 7 a.m. to noon is required to reproduce the measured time series.

of electron energy after an EII reaction alters the shape of the resulting spectrum. In order to efficiently perform the simulations on enough flow lines to cover the region, we use the $W = 0$ assumption in our model. If we were to use the more realistic Kim and Rudd model, there would be more attenuation at lower energy, like in figure 6.1.

In addition, we show the model results for the time series in figure 6.8. The data is displayed in the left hand panel. Ignoring the discrepancy in the direction of curvature, we focus on the parameters needed to reproduce the qualitative form of the time series. Here, we know we must apply unrealistic

conditions to scale the interaction to the spacecraft location due to the extremely vast extent of the MPB in this case. Scaling the thickness of the interaction region to .1 of the measured thickness, we obtain the right hand panel. The timing is slightly off at higher energy. The data show that most of the higher energy attenuation is complete at altitudes higher than the attenuation at low energy begins. The model is unable to duplicate that effect. However, the shape of the distribution in the energy range between 50-100 eV is an extremely good match. The simulation mimics the total attenuation from post-shock to post-MPB levels very well at $E > 50$ eV.

6.7 Summary of Simulation Results

The cases presented above demonstrate the capability of this model to simulate the evolution of the electron distribution in the magnetic pileup boundary at Mars. Given the inherent errors in our model due to the model neutral atmosphere, velocity field, and magnetic field inputs, we are pleased with the degree to which we are able to match the data. Therefore, we have confidence that our hypothesis accurately describes the physics of the formation of the MPB.

Simulations indicate that the shape of the attenuation is a good indicator of neutral composition. Atomic oxygen and hydrogen are the primary contributors to the signature. As well, they show that the integrated neutral density encountered along a streamline over time is on the order of 10^8 s/cm^3. Also, we find that the scale heights in the neutral density can be revised to improve the model. Further, we find that the spectral evolution is impossible to recreate without including shear in the tangential velocity in a layer above the ionopause.

In addition, we conclude that further study must accompany future work on this topic on the geometry of interaction. The shape of the ionopause effects the altitude of the flow. Therefore, its shape must be included into the flow model to

raise the flux tubes out of the interaction region at high latitudes. Moreover, the issue of scale lengths figures in to the geometry issue in how magnetic flux tubes flare with increasing magnetic longitude.

Finally, we demonstrate the range of possible states of the MPB with simulations of different orbits with quite different initial distributions. Even in the high field case, the model performs adequately. So we feel that the model is accomplishing its intended purpose. It can calculate the evolution of the electron distribution function as a result of electron impact ionization reactions just above the ionopause of Mars.

7. Discussion

We have shown that our model is able to reproduce the evolution of the electron distribution function observed by the ER in the MPB. This invokes confidence that our approach includes the accurate physics of the evolution of the electron distribution in the MPB. Besides being an interesting exercise, our work has several implications for other research. Of obvious relation, our model defines an integral measure of neutral density along flow lines. We elaborate on the consequences this has on existing models in section 7.1. However, our work also provides tantalizing insight into Mars climate studies. We are able to use our results to estimate the water loss rate at Mars do to EII reactions. A discussion of our estimate and its ramifications appears in section 7.2.

7.1 Implications for Existing Mars Models

The data from MGS show that electron impact ionization is draining energy from the electrons in the shocked solar wind flow around Mars. Our simulations indicate that the electrons of a flow element pass through a time integrated neutral density of $4.3\times10^{8}\ {}^{s}/_{cm^3}$ of *H* or $1.5\times10^{8}\ {}^{s}/_{cm^3}$ of *O* to explain the level of attenuation in the electron flux. The all-hydrogen simulation did a much better job at reproducing the final spectral shape. Oxygen lacked the ability to reduce the distribution at E < 75 eV. In reality, there is some ratio of oxygen to hydrogen with on the order of $10^{8}\ {}^{s}/_{cm^3}$ of each atom present.

Also, the data suggest that the effects of EII are confined to a small range in altitude in the measurements. Considering that the electrons are tied very closely to magnetic field lines and have a thermal speed much faster than the flow speed, we conclude that the spacecraft can be measuring the effects of EII remotely. The electrons interact with exospheric neutrals where they are most

dense. The attenuation in the distribution function is then observed as the electrons follow the field line to higher altitudes. Due to the limited coverage of the SPO orbits, we are unable to verify this with data from the magnetic noon line. However, it is a reasonable hypothesis.

Next, divergence free conditions place strict limitations to the assumptions made about the geometry of magnetic field lines. The magnetic field drapes around the dayside sub-flow point. At angles off of magnetic noon, the magnetic field magnitude must decrease, widening the spacing between magnetic field lines. So, if we measure a scale height at a local time off of magnetic noon and assume that the feature originated close to magnetic noon, it must correspond to a much smaller altitude range at the noon line.

Combining the above ideas, one must conclude that the flow is either encountering a very high density of neutrals or spending a long time in a lower density. The existing flow velocity and neutral density models undershoot the time-density integral needed to explain the data. Therefore, either the flow model is too fast, the neutral exosphere is too sparse, or both. In fact, we know both of these to be true.

The velocity model of *Spreiter and Stahara* [1980] does not include a shear in the tangential velocity near the ionopause. The ionosphere is gravitationally bound to the planet. The escape speed at Mars is 5 km/s. In a layer near the ionopause, the flow speed must slow from the 50-200 km/s sheath speed to below the escape velocity. In fact, experiments on Phobos identified a boundary in the four ellipticlal orbits at a similar location to the MPB at which the composition of the plasma changed as well as the flow velocity [*Lundin et al.,* 1989]. The composition of the plasma changes to heavy ions while the flow speed slows dramatically. This boundary occurs above the ionopause and seems to coincide with the magnetic pileup boundary. This Phobos observation

confirms the need for a velocity shear in altitudes above the ionopause. A shear in the velocity flow is implemented into our calculation; however, a shear model based on physics must be developed for accuracy. Our work and the scale size of the interaction region can provide an estimate of the thickness of the shear layer.

Similarly, the martian atmosphere is known to be highly variable on a number of timescales [*Keating et al.*, 1998]. The MGS aerobraking data has shown that low altitude atmospheric density can change on the timescale of a day. Additionally, the neutral exosphere is modulated by the solar cycle, due to changing EUV flux. The neutral exosphere models [*Kim et al.*, 1998] do have different profiles for solar maximum verses solar minimum conditions. But even the higher density predictions at solar maximum are not enough to reproduce the data with the existing velocity models. Further, the interaction seems to be occurring very close to where the atmospheric scale heights turn from the cold to the hot scale height. The exospheric scale heights are not well known and hard to measure. Therefore, the scale size of the MPB can be used to determine the neutral scale height. There is a lot of room for improvement in the neutral models. They sufficed with the dearth of data available previously. However, with the addition of our integral measurement of neutral density, these models must be revised to fit the new constraints developed here.

In addition, we must ensure that the assumptions we make about inclination of the magnetic field lines are reasonable. Measurements of the electron spectra at altitudes ranging from 700-1500 km, varying with orbit, contain evidence of electron cooling. We hypothesize that this is the signature of EII reactions occurring just above the ionopause at the sub-flow point. The spacecraft crosses the ionopause at altitudes between 400-800 km at a solar zenith angle of 60°. Using model ionopause shapes developed for Venus

[*Knudsen et al.*, 1982; *Knudsen*, 1992], we find the 60° ionopause crossings map to sub-flow altitudes of 225-450 km. Somehow, we must reconcile the large inclination of the magnetic field needed to attach 800 km at 45° to 250 km at 0°. In addition, if we accept this large inclination, we must constrict the thickness of the interaction region even more. This requires even higher density and/or slower flow. If we reject the large inclination of the magnetic field, then we must raise the neutral density at high altitudes and explain the departure from the ionopause location.

7.2 Implications for Water Loss on Mars

There is copious geologic evidence that water once was bountiful on the surface of Mars. First of all, there is an extended network of channels on Mars. Although the channels could be formed by lava flows, ice, or wind erosion, studies of the erosion of the land indicate that water is the most likely cause of the features seen. Also, flood plains and outflows indicate that fluvial processes were once active at Mars. In fact, estimates of an equivalent depth of water, if the layer were spread across the entire surface range from 50-300 m [*Carr*, 1987]. This is troublesome because the present day Martian climate cannot provide the conditions necessary for such volumes of water on the surface. So the question arises, "where did the water go?"

Because Mars lacks an intrinsic magnetic field of significance, the solar wind comes into direct contact with the planetary exosphere. As shown by our model results, this translates into a mechanism in which the martian atmosphere is systematically ionized. Newly formed ions are picked up by the solar wind and carried away. The aggregate process leads to the erosion of the martian atmosphere over time. The exosphere is primarily populated by atomic hydrogen and oxygen. One can trace the loss rate of water on Mars by studying the loss of

these volatiles. When one couples this with the knowledge that the planetary dynamo seems to have stopped around 3.9 billion years ago [*Acuña et al.*, 1999], we now have a mechanism which can efficiently erode the atmosphere away that started at approximately the time that water on the planet disappeared.

Much of the evidence indicates that the greatest amount of water was present around 3.5 billion years ago. Channels occur most frequently in the old cratered terrain, with relatively few channels in the newer plains [*Pieri*, 1976]. Therefore, the water volume required to produce such channels vanished early in the planetary history. *Craddock and Maxwell* [1993] conclude from the degradation of impact craters that erosion was most efficient 3.5 billion years ago. In support is the evidence that volcanism has occurred since at least 3.9 x 10^9 years ago [*Greeley*, 1987]. Volcanism is a major source of outgassing, which is the release of volatiles into the planetary atmosphere. These volatiles are necessary to supply the surface water and atmosphere. Further, Greeley demonstrates that volcanism achieved a maximum for planetary outgassing around 3-4 billion years ago, releasing the equivalent of 46 m of water.

Early in the history of the solar system, the conditions pertinent to the solar wind interaction (and our results here) were quite different. The solar wind was stronger, having a particle flux that was much higher than present [*Heymann*, 1977]. Similarly, the intensity of solar EUV flux has decreased to the present day value. The effects of these changes on the solar wind interaction are as follows. The higher solar EUV radiation would have energized the atmosphere. Therefore, it would increase the height of the atmosphere and the spatial extent of the interaction region. The stronger solar wind creates a hotter electron distribution capable of ionizing more material. We examine our results to predict the contribution to the erosion of the martian atmosphere from electron impact ionization. We perform calculations for both the current conditions and the

assumed ancient conditions and compare our results to previous estimates and observed outflow rates.

Calculation of Present Day Volatile Loss from Electron Impact Ionization

A naive estimate can be made by calculating the number of EII reactions required to cool an 100 eV electron gas to 10 eV. Although the post-shock distribution is non-Maxwellian, 100 eV provides a zeroeth order approximation to the distribution observed. In this case, the reactions are assumed to carry on until the average energy of the electrons falls below the threshold of the reaction. The average electron participates in 5 EII reactions to lose 90 eV. Thus, the average electron is responsible for producing 5 new ions before it passes through the MPB, if the process is efficient.

We can investigate the efficiency of the process by calculating the extent to which the electrons ionize the neutral medium. Integrating the kinetic energy of the electrons over the measured distribution function before and after the MPB, we calculate the fraction of average kinetic energy lost by the electrons across the magnetic pileup boundary. The result is that the average electron energy decreases to 20% of the post-shock value. We conclude that the process is reaching saturation, meaning most of the energy that can go into ionizing neutrals is doing so. Thus, the average electron participates in 80% of the average reactions, reducing the electron multiplier to 4.

Then, to derive an ion loss rate, dN_i/dt, we find the product of the electron multiplier, dN_i/N_e, with the electron flux, $n_e v$, and the effective area of the interaction region, A:

$$\left\langle \frac{dN_i}{dt} \right\rangle = \left\langle \frac{dN_i}{N_e} n_e v A \right\rangle$$

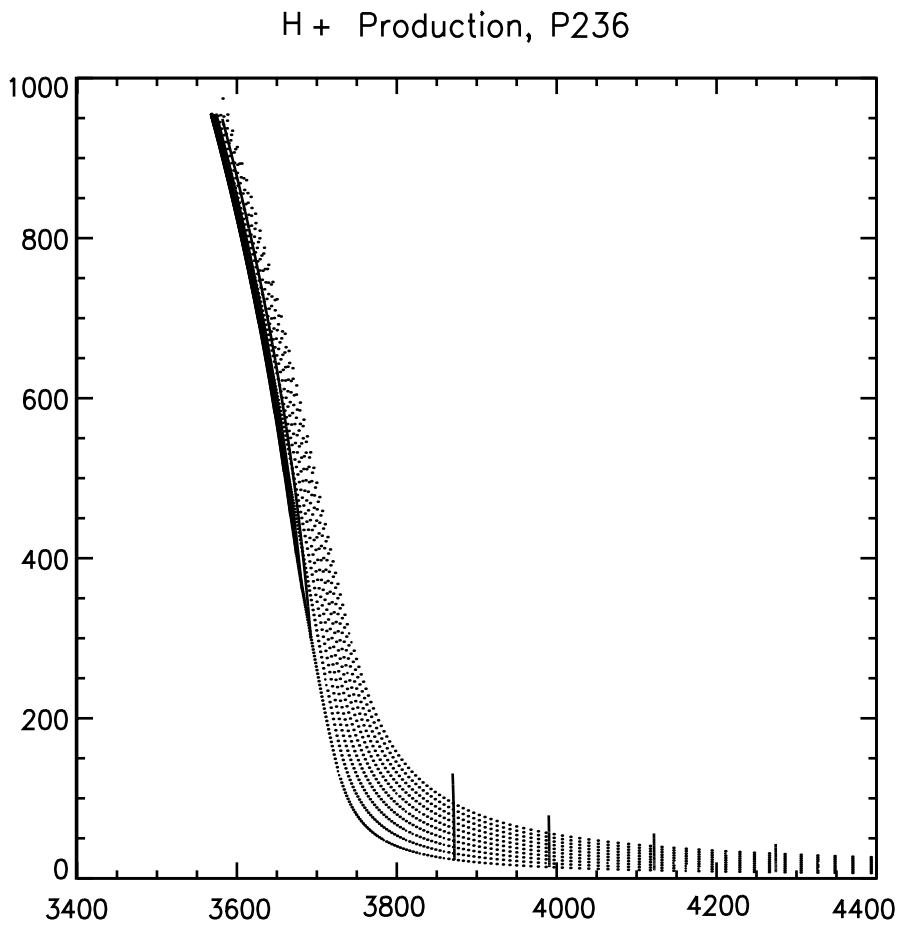

Figure 7.1. Contours of H^+ production rate from model output for P236. Computed production rates are along streamlines. Streamlines are indicated by the dotted lines.

Using 10 e^-/cm^3 electron density and 25 km/s flow and an area equal to the cross section of the planet at 400 km altitude and 45°, we get 2.3×10^{25} ions/s produced due to EII at Mars. They are presumably lost then to solar wind pick up.

We can refine this estimate, however, using our model. Our model calculates the number of ions produced due to EII reactions along a flow line using the observed distribution function. We perform calculations along several streamlines and find the density of ions produced at each point. Each flow line begins being separated by a constant angle off of the Mars-Sun line. Shown in figures 7.1 and 7.2 are the contours of hydrogen and oxygen ion production,

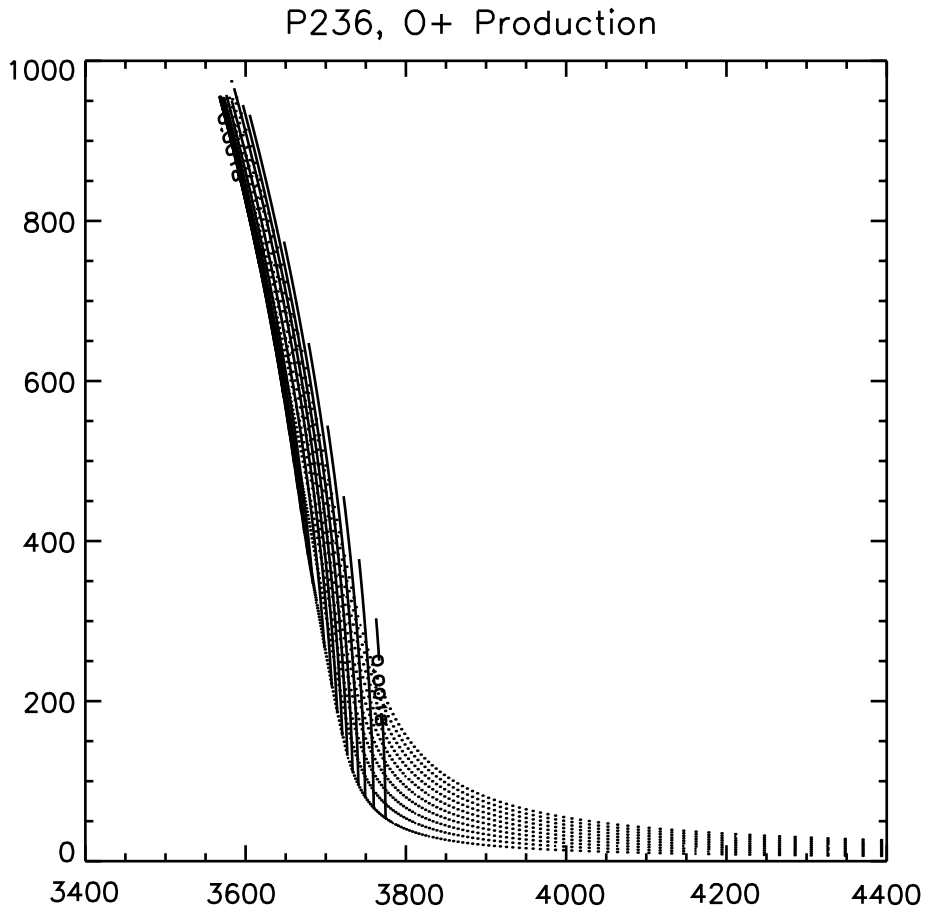

Figure 7.2. Contours of O^+ production rate from model output for P236. Computed production rates are along streamlines. Streamlines are indicated by the dotted lines.

respectively, for P236. The dotted lines show the geometry of the streamlines in our velocity model. Of obvious note, the production rates increase with decreasing altitude. However, as the electrons lose energy ionizing neutrals, the ionizing power of the electrons is reduced. When the product of the density and the reaction rate begins to decline, the flow has gone a distance of ~30° around the planet, in general. Likewise, in figures 7.3 and 7.4 the production rate contours for P456 are given. Here, because the interaction is spread out over a much larger altitude range, the contours are much easier to see.

Only the contours of H^+ and O^+ are shown because the CO_2 daughters are only found in trace amounts. We plot the production rates for H^+, O^+, and

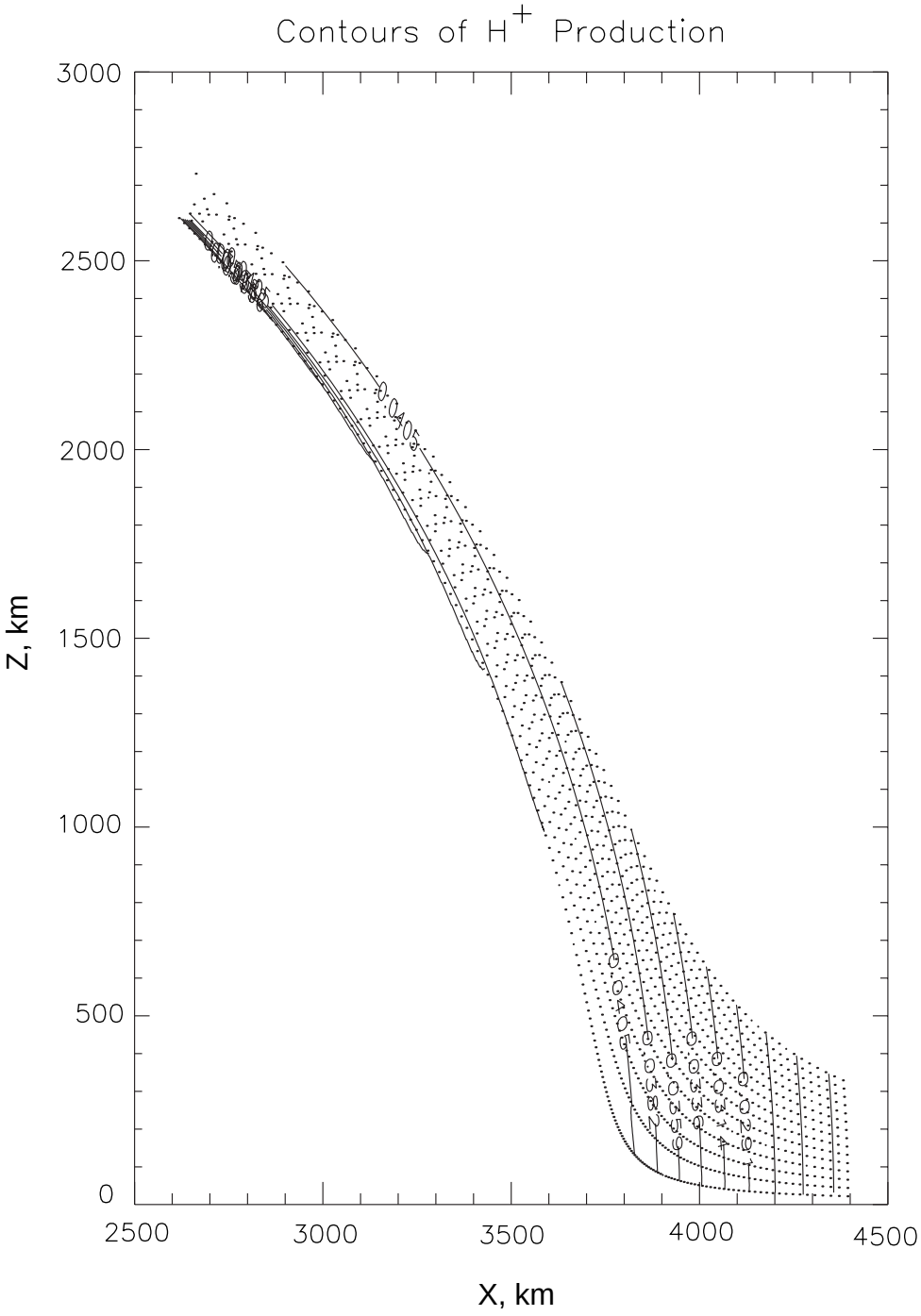

Figure 7.3. Contours of H^+ production rate from model output for P456. Computed production rates are along streamlines. Streamlines are indicated by the dotted lines.

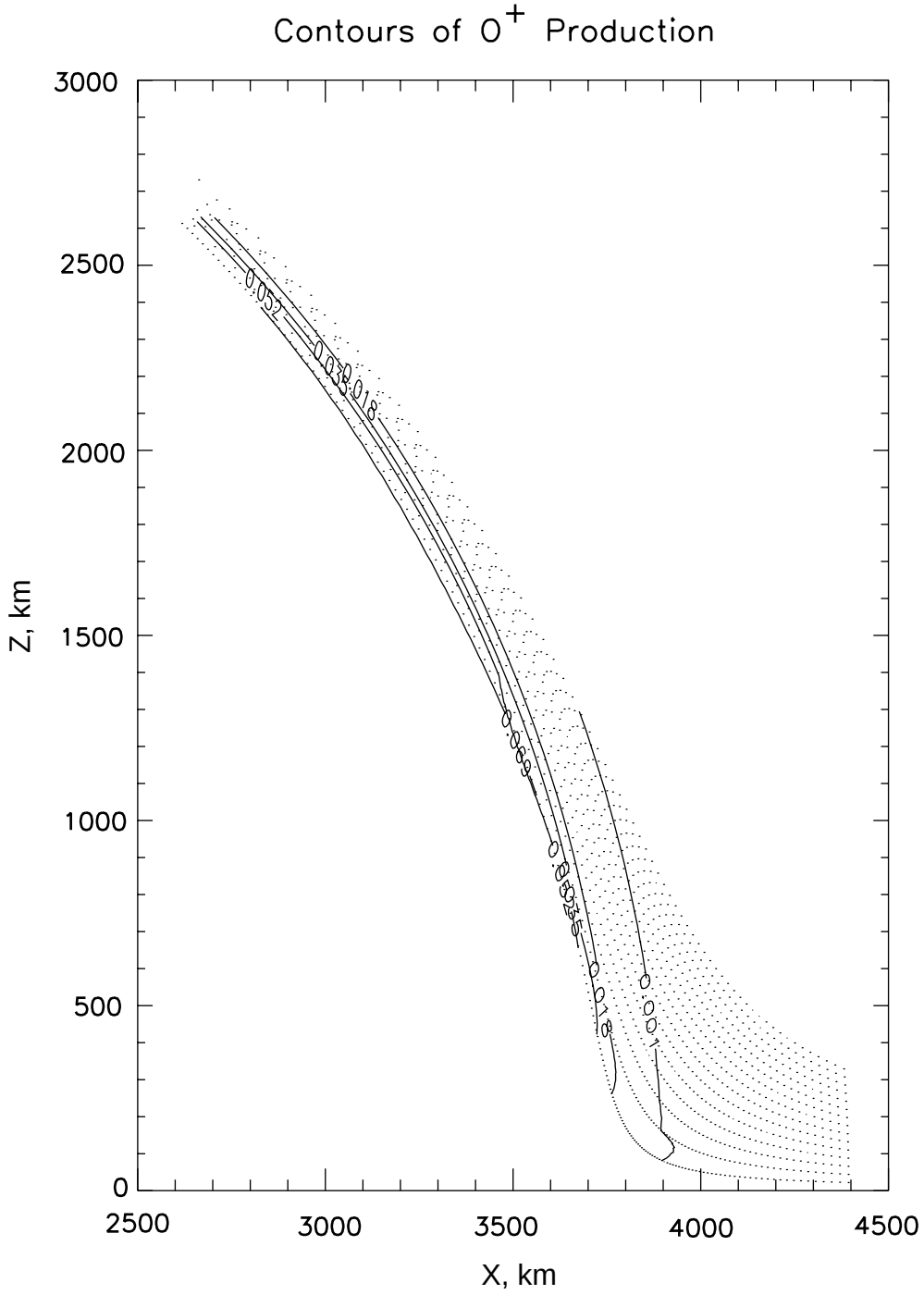

Figure 7.4. Contours of O^+ production rate from model output for P456. Computed production rates are along streamlines. Streamlines are indicated by the dotted lines.

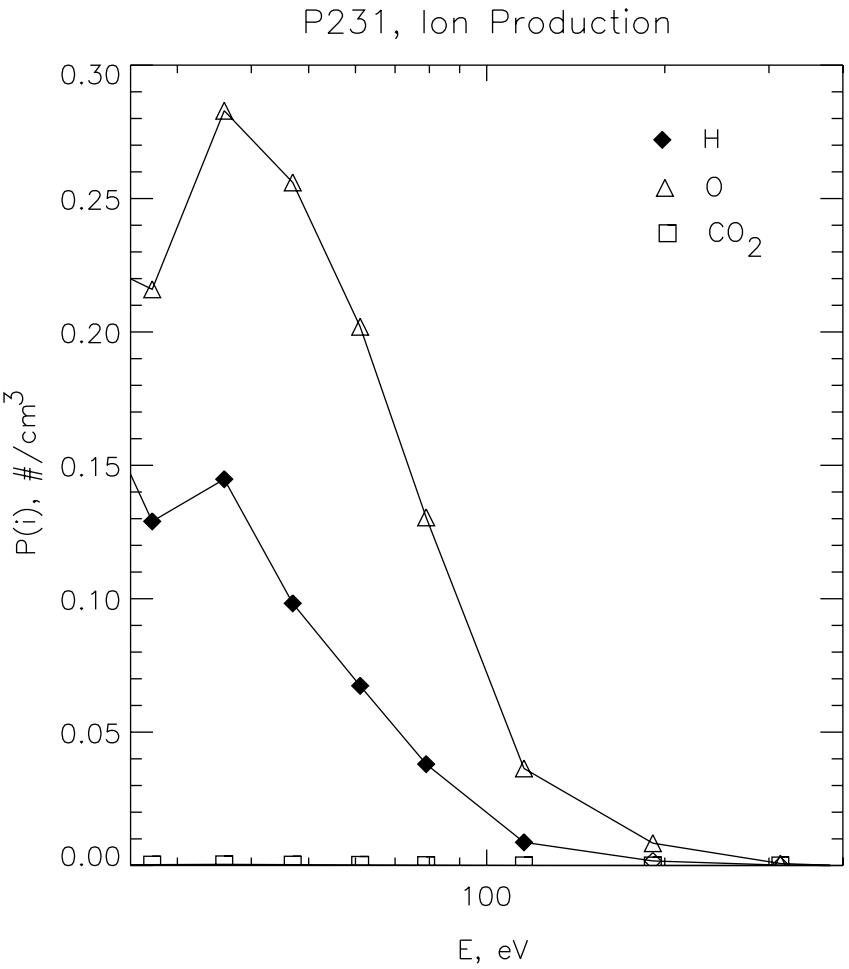

Figure 7.5. Ion production by electron energy. O^+ is the top line (Δ), H^+ is the middle line (♦), and CO_2^+ is the bottom line (❑).

CO_2^+ at a representative position as a function of electron energy in figure 7.5. CO_2^+, the daughter ion with the largest fractional cross section, is barely detectable as the partial squares along the bottom of the plot. O^+ (from both *e-* on *O* and *e-* on CO_2, although the CO_2 does not contribute much) is produced at about twice the rate of H^+. However, the proportionality of *H* to *O* production is highly dependent on neutral density. Therefore, the proportionality of the resulting ions is only as reliable as the model inputs, which have large margins for error.

Integrating the production rate over the extent of the flow line we get the column production rate of ions produced by the flow element. Summing over all flow lines and multiplying by the effective area of the interaction region we get:

$$\frac{dN_i}{dt} = \sum_{lines} H_{i,line}\, L \int P_{i,line}\, dl_{line}$$

where H_i is the distance between flow lines, L is the width of the interaction region, dl is the distance a flow element traverses in one time step, P_i and is the EII production rate integrated over energy for the time step. The result is ~2 x 10^{24} ions/s using our assumptions about the geometry of the flow. This is lower than our naive estimate by an order of magnitude. Naturally, the result is quite sensitive to the input models. The size of the flow element parameters H and dl are entirely dependent on the flow model. Recharacterizing the shear layer, as we expect is necessary, would effect this result. For instance, in our examples in the previous chapter, we made what bordered on unrealistic assumptions about the scaling height from noon to other local times. If the height were more realistic but the neutral density remained the same, we could gain another factor of 2-4 with that parameter. Also, with the relatively poor ability for the model to reproduce the spectrum in the lower energy bins without using the differential cross section assumption, we find that the production rate suffers. Therefore, we reserve the prerogative to modify this result as we attain a better grasp on those parameters.

Lundin et al. [1990] measured ion outflow rates from the tail of Mars with the PHOBOS ASPERA instrument. ASPERA measured ions from .5 eV/q - 24 keV/q in 10 angular sections. Data from the 4 elliptical orbits, indicate an outflow rate of $3 \times 10^{25}\, O^+/s$. This agrees with our naive estimate, but is higher than the predictions of our model. It is reasonable to surmise that electron impact ionization is a contributor to volatile loss at least the 10% level in the present solar wind interaction. Other mechanisms for mass removal of atmosphere also

contribute. One such process is the mass removal of ionospheric plasma through the formation and subsequent loss of high altitude ionospheric clouds [*Brace et al.*, 1982] perhaps analogous to the viscous layer proposed by *Perez-de-Tejeda* [1998]. Charge exchange and photoionization also produce ions above the ionopause, although their rates are lower than electron impact ionization above the magnetic pileup boundary. Atmospheric sputtering from these pickup ions can amplify the production rate [*Luhmann and Kozyra*, 1991] by producing secondary ions as energetic pick-up ions impact the cold atmosphere.

Estimate of Water Loss at Ancient Mars from Electron Impact Ionization

Now, we use the assumptions of higher solar EUV flux in the early history of Mars [*Zahnle and Walker*, 1982] to simulate EII in the solar wind interaction with Mars under the conditions of 3.5-4 billion years ago. The atmospheric density increases by a factor of at least an order of magnitude at the relevant altitudes [*Zhang et al.*, 1993]. Likewise, the solar wind velocity and density were higher in the ancient solar system. We use a solar wind flux that is a factor of 10 greater than the present value, estimated from Argon deposition in lunar soil [*Heymann*, 1977].

Our results are quite interesting. First of all, the neutrals are able to sap all of the available energy from the solar wind electrons. This, unfortunately, is a contingency the model is not prepared to deal with. In fact, as the slope of the distribution function tries to turn positive, the calculations blow up. A redistribution mechanism would have to be incorporated in order to effectively model the interaction under those conditions. So we revert to our "naive" estimate made above. To account for the different conditions in that era, we inflate the extent of the interaction region to 1200 km, add an order of magnitude

to the electron flux, up the average electron energy by 3 and use 100% of the ion production power of each electron. In depth of a surface layer water spread uniformly across the planet, this corresponds to $^{8\,m}/_{10^9\,yr}$. Over the .5 - 1 billion year period in which the magnetic field was absent and water was present on the surface of Mars, this mechanism can remove 4 - 8 m of the 50 m assumed surface water content of Mars. Although blow off from impacts is probably the major source of volatile loss at Mars, EII reactions contributed at the 10% level.

8. Conclusions

A detailed analysis of the magnetic field data and electron profiles measured by the MAG/ER instrument complement on MGS in the dayside post-shock region reveals that a magnetic pileup boundary does exist at Mars, like those observed at comets. We have demonstrated in this thesis that the MPB is marked by several features in the data. We have interpreted those features to be evidence of electron impact ionization producing an unstable population of hot planetary ions in the sheath while deflating the electron pressure in the flow. Careful consideration of the geometry of the interaction reveals that the spacecraft electron measurements are local measurements reflecting remote processes. Modeling has successfully reproduced the form of the electron spectrum in the MPB. Further, the modeling efforts have revealed some areas where existing Mars models are lacking, and thus should be reworked to fit the constraints we provide through this work.

8.1 Summary of Results

The MAG data indicates that, in the MPB, the magnetic field rises from the mean post-shock value to one usually higher than that predicted by the *Spreiter and Stahara* [1980] gasdynamic model. Therefore, the magnetic pressure is greater than that predicted by the gas dynamic models. Because overall pressure balance must be achieved at all stages of the flow, the excess magnetic pressure must be a result of lost pressure in one of the other components. Although there are no ion instruments on MGS, we suspect that the magnetic field is exchanging pressure with the shocked plasma's ion thermal pressure. Despite the fact that we observe a deflation in the electron spectrum, the electrons do not contain nearly enough thermal pressure to account for the build

up in magnetic field. At the stagnation point, where the flow velocity goes to zero by definition, a considerable portion of the ion thermal pressure must be lost to the magnetic field.

The exact region where the magnetic field piles up coincides with the location of the attenuation of electron flux as measured by the ER. The deflation of the electron spectrum exhibits evidence of electron impact ionization in that the fluxes are lost most readily in the energy ranges that match the peak in EII cross sections for neutral atoms indigenous to the martian exosphere. This provides a mechanism for producing the unstable population of planetary ions in the sheath which cause ion cyclotron waves to form.

An extremely important point we make is that the geometry and scale times for the interaction must be considered in order to develop a comprehensive picture of the formation of the MPB. Electron thermal speeds are very fast compared to the local flow velocity. In addition, electrons have very small cyclotron radii, keeping them closely bound to magnetic field lines. As the conducting ionosphere induces magnetic field draping in the incident flow, the flanks of the planet become magnetically connected to low altitudes. Then, electrons observed along a field line have a distribution that is the result of the combination of all processes affecting them along the entire traverse of the field line, as they bounce back and forth between the bow shock on both ends. Therefore, it is essential that all data be converted into a magnetic field aligned coordinate system to elucidate the geometric influence on the boundary. Specifically, in the case of the MPB, the region of interest is the lowest altitude attained along the field line and the distance to that position, where the neutral density is a maximum. There, the electrons ionize planetary neutrals at a fast rate, giving up the ionization potential from their kinetic energy with each reaction. The effects of this are observed elsewhere on the magnetic field line as

attenuation in the electron spectrum. The attenuation can exhibit a time delay in the slower, lower energy electrons.

We successfully model this pattern of attenuation observed in the electron spectra. The model calculates the cumulative effect of electron impact ionization reactions on the original post-shock electron distribution function along flow lines. For flow times of about 100 s. in a neutral density similar to that at ~300-325 km altitude at Mars, the electron spectrum deflates to the value of the spectrum observed at the end of the MPB. Further, we determine the dominant neutral constituent by studying the apparent neutral scale heights effecting the attenuation pattern. For the orbits we present here, CO_2 seems to play a negligible role while *H* and *O* dominate.

8.2 Future Directions

From here, the next step to understanding the magnetic pileup boundary is to collect more data. The Japanese spacecraft, Planet B, should reach Mars in 2003. If successful, Planet B is capable of measuring the quantities needed to verify our hypothesis of the formation of the MPB. In fact, our model predicts quantities such as heavy ion density that can be measured.

Further, compilations of several orbits can give a larger picture of the geometry of the MPB. Our model predicts that the MPB should be observed at low altitudes very close to the magnetic noon line. In contrast, it should be thicker and higher at local magnetic times off of noon because of the inclination of the magnetic field. Similarly, more of an effect should be observed at high magnetic latitudes, as the flow has had more time to react with the planetary neutrals. This effect dominates up to the point where the ionopause flare boosts the magnetic field line above the required neutral density. In contrast, the MPB

close to the equator should appear to be smaller. This effect is counterbalanced by the increased flow speed around the planet approaching the terminator.

Also, there are still some unanswered questions about the MPB at Mars. First of all, what causes the electron spectrum to stop evolving at the end of the MPB? Clearly, something is keeping the spectrum at a fairly constant power law after the MPB. This is seen to persist for several hundred kilometers in altitude on some orbits, until the spacecraft enters the ionopause. On other orbits, the ionopause or high altitude clouds occur immediately below the MPB along the spacecraft trajectory. Most likely, geometry plays the primary role in this effect. We suggest that the EII is occurring along magnetic field lines following the ionopause over the planet. As the altitude of the ionopause flares at greater solar zenith angles, our field lines are lifted out of the high density region. The spectrum is already deflated from its passage through the neutral atmosphere. However, at the higher altitude and the lower energy, further reactions occur at a reduced rate.

There is another solution to the problem. Perhaps, below the MPB, the electrons are tied to a thermalizing region. If the lowest altitude field line of the MPB skims above the ionopause, as we suggest, then at lower altitudes the field lines enter the ionosphere. As the electrons are magnetically connected to the ionosphere, they interact with a cold plasma at some point along their trajectory. The post-MPB spectrum, then, is a composite of the distributions. Therefore, it is not necessary that EII ceases below the MPB as long as there is a mechanism to redistribute the electrons to the observed distribution.

Finally, this work puts the onus on the modeling community to revise their models to fit the constraints we have determined. First, the cumulative neutral density seen by a magnetic field line during its traverse around the planet must increase by a factor of 10. So the neutral density must be increased, the flow

density must decrease, or most likely, both must occur. An accurate velocity shear must be adapted to flow models. Because the neutral atmosphere of Mars is highly variable, a factor of 10 difference in neutral density is not hard to imagine. However, exospheric neutral models need to include a wider range of possible configurations in order to span the range of atmospheric conditions observed. Further, the neutral scale heights need to be revamped to better fit the scale size of the interaction that is observed.

Another result of our work that pertains to the modeling community is that all models of flow in the sheath of Mars must include wave particle interactions in order to be accurate. The prevalence of waves and their effects on the particles in the flow demonstrate a non-negligible component to the interaction of the solar wind with Mars. Therefore any model that claims to be able to describe the interaction that cannot produce waves needs to be amended.

In conclusion, this work is the first effort to reproduce the electron distribution function in the magnetic pileup boundary at Mars. *Cravens et al.* [1987] use electron distributions to deduce the EII rate at comets Halley and Giacobini-Zinner. *Kar et al.* [1994] calculate ion density in the nightside ionopshere of Venus due to EII reactions from solar wind electrons crossing the terminator within the ionosphere. However, here we present the first simulation that actually reproduces the observed fluxes over a number of orbits. The theory seems to be consistent with all of the available observations. New observations form other spacecraft are anticipated to test our hypothesis.

References

Acuña, M.H., J.E.P. Connerney, P. Wasilewski, R.P. Lin, K.A. Anderson, C.W. Carlson, J. McFadden, D.W. Curtis, H. Rème, A. Cros, J.L. Medale, J.A. Savaud, C. d'Uston, S.J. Bauer, P. Cloutier, M. Mayhew, and N.F. Ness. Mars Observer Magnetic Fields Investigation, *J. Geophys. Res.*, **97**, 7799-7814, 1992.

Acuña, M.H., J.E.P. Connerney, P. Wasilewski, R.P. Lin, K.A. Anderson, C.W. Carlson, J. McFadden, D.W. Curtis, D. Mitchell, H. Rème, C. Mazelle, J.A. Savaud, C. d'Uston, A. Cros, J.L. Medale, S.J. Bauer, P. Cloutier, M. Mayhew, D. Winterhalter, and N.F. Ness. Magnetic Field and Plasma Observations at Mars: Initial Results of the Mars Global Surveyor Mission, *Science*, **279**, 1676-1680, 1998.

Acuña, M.H., J.E.P. Connerney, N.F. Ness, R.P. Lin, D.L. Mitchell, C.W. Carlson, J. McFadden, K.A. Anderson, H. Rème, C. Mazelle, D.Vignes, P. Wasilewski, and P. Cloutier. The History of Mars: Global Distribution of Crustal Magnetism Discovered by the Mars Global Surveyor MAG/ER Experiment, submitted to *Science*, 1999.

Albee, A.L., F.D. Palluconi, and R.E. Arvidson. Mars Global Surveyor Mission: Overview and Status, *Science*, **279**, 1671-1672, 1998.

Allen, C.W. *Astrophysical Quantities*, The Athlone Press: London, 1963.

Banks, P.M. and G. Kockarts. *Aeronomy*, Academic Press: New York, 1973.

Bauske, R., A.F. Nagy, T.I. Gombosi, D.L. Dezeeuw, K.G. Powell, and J.G. Luhmann. A 3-Dimensional MHD Study of Solar Wind Mass Loading Processes at Venus--Effects of Photionization, Electron Impact Ionoization and Charge Exchange, *J. Geophys. Res.*, **103**, 23625-23638, 1998.

Biermann, L. KomentenSchweife und Solare Korpuskularstrahlung, *Zeitschrifte für Astrophysik*, **29**, 274-286, 1951.

Brace, L.H., R. Theis, and W. Hoegy. Plasma Clouds Above the Ionopause of Venus and Their Implications, *Plan. Space Sci.*, **29**, 20, 1982.

Breus, T.K., A.M. Krymskii, R. Lundin, E.M. Dubinin, J.G. Luhmann, Ye. Yeroshenko, S.V. Barabash, V.Ya. Mitnitskii, N.F. Pissarenko, and V.A. Styashkin. The Solar Wind Interaction with Mars: Consideration of Phobos 2 Mission Observations of an Ion Composition Boundary on the Dayside, *J. Geophys. Res.*, **96**, 11165-11174, 1991.

Cable, S. and R.S. Steinolfson. Three-dimensional MHD Simulations of the Interaction between Venus and the Solar Wind, *J. Geophys. Res.*, **100**, 21645-21658, 1995.

Carr, M.H. Water on Mars, *Nature*, **326**, 30-37, 1987.

Cloutier, P.A., M.B. McElroy and F.C. Michel. Modification of the Martian Ionosphere by the Solar Wind, *J. Geophys. Res.*, **74**, 26, 6215-6228, 1969.

Cloutier et al. The Physics of the Magnetic Pileup Boundary at Mars, in progress.

Chapman, S. The Absorption and Dissociative or Ionizing Effect of Monochromatic Radiation in an Atmosphere on a Rotating Earth, *Proc. Phys. Soc.*, **43**, 484, 1931.

Coates, A.J. Ionospheres and magnetospheres of comets, *Adv. Space Res.*, **20**, 2, 255-266, 1997.

Colin, L. The Pioneer Venus Program, *J. Geophys. Res.*, **85**, 7575-7598, 1980.

Craddock, R.A. and T.A. Maxwell. Geomorphic Evolution of the Martian Highlands Through Ancient Fluvial Processes, *J. Geophys. Res.*, **98**, 3453-3468, 1993.

Cravens, T.E., J.U. Kozyra, A.F. Nagy, T.I. Gombosi, and M. Kurtz. Electron Impact Ionization in the Vicinity of Comets, *J. Geophys. Res.*, **92**, 7341-7353, 1987.

Dolginov, Sh.Sh. On the Magnetic Field of Mars: Mars 2 and 3 Evidence, *Geophys. Res. Let.*, **5**, 1, 89-93, 1978.

Dubinin, E., K. Sauer., R. Lundin, O. Norberg, J.-G. Trotignon, K. Schwingenschuh, M. Delva, and W. Riedler. Plasma Characteristics of the Boundary Layer in the Martian Magnetosphere, *J. Geophys. Res.*, **101**, 27061-27075, 1996.

Elphic, R.C., C.T. Russell, and J.A. Slavin. Observations of the Dayside Ionopause and Ionosphere of Venus, *J. Geophys. Res.*, **85**, 7679-7696, 1980.

Glassmeier, K.H., U. Motschmann, C. Mazelle, F.M. Neubauer, K. Sauer, S.A. Fuselier, and M.H. Acuña. Mirror Mode and Fast Magnetoacoustic Waves Near the Magnetic Pileup Boundary of Comet P/Halley, *J. Geophys. Res.*, **98**, 20955-20964, 1993.

Goldstein, B.E., M. Neugebauer, H. Balsiger, J. Drake, S.A. Fuselier, R. Goldstein, W.-H. Ip, U. Rettenmund, H. Rosenbauer, R. Schwenn, and E.G. Shelley. Giotto-IMS Observations of Ion-Flow Velocities and Temperatures outside the Magnetic Cavity of Comet P/Halley, *Astronomy & Astrophysics*, **187**, 174-178, 1987.

Golombek, M.P., R.A. Cook, T. Economou, W.M. Folkner, A.F.C. Haldemann, P.H. Kallemeyn, J.M. Knudsen, R.M. Manning, H.J. Moore, T.J. Parker, R. Rieder, J.T. Schofield, P.H. Smith, and R.M. Vaughan. Overview of the Mars

Pathfinder Mission and Assessment of Landing Site Predictions, *Science*, **278**, 1743-1748, 1997.

Grard, R., A. Pederson, S. Klimov, S. Savin, A. Skalsky, J.G. Trotignon, and C. Kennel. First Measurements of Plasma Waves near Mars, *Nature,* **341**, 607-609, 1989.

Greeley, R. Release of Juvenile Water on Mars: Estimated Amounts and Timing Associated with Volcanism, *Science*, **236**, 1653-1654, 1987.

Hanson, W.B., S. Sanatani, and D.R. Zuccaro. The Martian Ionosphere as Observed by the Viking Retarding Potential Analyzers, *J. Geophys. Res.*, **82**, 4351-4363, 1977.

Harel, M., R.A. Wolf, P.H. Reiff, R.W. Spiro, W.J. Burke, F.J. Rich, and M. Smiddy. Quantitative Simulation of a Magnetospheric Substorm--1. Model Logic and Overview, *J. Geophys. Res.*, **86**, 2217-2241, 1981.

Hastings, D. and H. Garrett. *Spacecraft-Environment Interactions*, Cambridge University Press: New York, 1996.

Heymann, D. Particle Output of the Sun in the Past,*The Solar Output and Its Variation*, O.R. White (ed.), Colorado Associated University Press, 405-427, 1997.

Hirao, K. and T. Itoh. The Planet A Halley Encounters, *Nature*, **321**, 294-297, 1986.

Hviid, S.F., M.B. Madsen, H.P. Gunnlaugsson, W. Goetz, J.M. Knudsen, R.B. Hargraves, P. Smith, D. Britt, A.R. Dinesen, C.T. Morgensen, M. Olsen, C.T. Pedersen, L. Vistisen. Magnetic Properties Experiments on the Mars Pathfinder Lander: Preliminary Results, *Science*, **278**, 1768-1770, 1997.

Hwang, W., Y.-K. Kim, and M. E. Rudd. New Model for Electron-Impact Ionization Cross Sections of Molecules, *J. Chemical Physics*, **104**, 8, 2956-2966, 1996.

Ip, W-H. On a Hot Oxygen Corona of Mars, *Icarus*, **76**, 135-145, 1988.

James, A. What Went Wrong with Mars-96? *Astronomy and Geophysics*, **38**, 1, 4, 1997.

Kallio, E. An Empirical Model of the Solar Wind Flow around Mars. *J. Geophys. Res.*, **101**, 11133-11147, 1996.

Keating, G.M., S.W. Bougher, R.W. Zurek, R.H. Tolson, G.J. Cancro, S.N. Noll, J.S. Parker, T.J. Schellenberg, R.W. Shane, B.L. Wilkerson, J.R. Murphy, J.L. Hollingsworth, R.M. Haberle, M. Joshi, J.C. Pearl, B.J. Conrath, M.D. Smith, R.T. Clancy, R.C. Blanchard, R.G. Wilmoth, D.F. Rault, T.Z. Martin, D.T.

Lyons, P.B. Esposito, M.D. Johnston, C.W. Whetzel, C.G. Justus, and J.M. Babicke. The Structure of the Upper Atmosphere of Mars: In Situ Accelerometer Measurements from Mars Global Surveyor, *Science*, **279**, 1672-1676, 1998.

Kennel, C.F. and H.E. Petschek. Limit on Stably Trapped Particle Fluxes, *J. Geophys. Res.*, **71**, 1-28, 1966.

Kim, J., A.F. Nagy, J.L. Fox, and T.E. Cravens. Solar Cycle Variability of Hot Oxygen Atoms at Mars, *J. Geophys. Res.*, **103**, 29339-29342, 1998.

Kim, Y-K and M. E. Rudd. Binary-Encounter-Dipole Model for Electron-Impact Ionization, *Physical Review A*, **50**, 5, 3954-3967, 1994.

Kliore, A.J., D.L. Cain, G. Fjeldbo, B.L. Seidel, M.J. Sykes, and S.I. Rasool. The Atmosphere of Mars from Mariner 9 Radio Occultaion Measurements, *Icarus*, **17**, 484-516, 1972.

Knudsen, W.C., K.L. Miller, and K. Spenner. Improved Venus Ionopause Altitude Calculation and Comparison with Measurement, *J. Geophys. Res.*, **87**, 2246, 1982.

Knudsen, W.C. The Venus Ionosphere from in Situ Measurements in *Venus and Mars: Atmospheres, Ionospheres, and Solar Wind Interactions*, Geophysical Monograph **66**, J.G. Luhmann, M. Tatrallyay, and R.O. Pepin, editors. American Geophysical Union, 237-263, 1992.

Krankowsky, D., P. Lämmerzahl, I Herrwerth, J. Woweries, P. Eberhardt, U. Dolder, U. Herrmann, W. Schulte, J.J. Berthelier, J.M. Illiano, R.R. Hodges, and J.H. Hoffman. In Situ Gas and Ion Measurements at Comet Halley, *Nature*, **321**, 326-329, 1986.

Larson, D.E. *Observations of Electron Distribution Functions near Halley's Comet*, Ph. D. Thesis, Department of Physics, University of California at Berkeley, 1993.

Law, C.C. *Currents and Magnetic Field Structures in the Dayside Solar Wind Interaction with Venus and Mars*, Ph.D. Thesis, Department of Space Physics & Astronomy, Rice University, 1995.

Law, C.C. and P.A. Cloutier. Observations of Magnetic Structure at the Dayside Ionopause of Venus, *J. Geophys. Res.*, **100**, 23973-23981, 1995.

Law, C.C. and P.A. Cloutier. Currents and Magnetic Field Structures in the Dayside Solar Wind Interaction with Venus, *J. Geophys. Res.*, **102**, 22199-22207, 1997.

Lichtenegger, H, E Dubinin and W-H Ip. The Depletion of the Solar Wind near Mars, *Adv. Space Res.*, **20** (2), 143-147, 1997.

Lindsay, B.G., D.R. Sieglaff, D.A. Schafer, C.L. Hakes, K.A. Smith, and R.F. Stebbings. Charge Transfer of 0.5-, 1.5-, and 5-keV Protons with Atomic Oxygen: Absolute Differential and Integral Cross Sections, *Physical Review A*, **53**, 1, 212-218, 1996.

Luhmann, J.G. and J.U. Kozyra. Dayside Pickup Oxygen Ion Precipitation at Venus and Mars: Spatial Distributions, Energy Deposition, and Consequences, *J. Geophys. Res.*, **96**, 5457, 1991.

Luhmann, J.G. and S.J. Bauer. Solar Wind Effects on Atmosphere Evolution at Venus and Mars, *Venus and Mars: Atmospheres, Ionospheres, and Solar Wind Interactions*, J.G. Luhmann, M .Tatrallyay, and R.O. Pepin, eds. Geophysical Monograph 66, 417-430, 1992.

Lundin, R., A. Zakharov, R. Pellinen, H. Borg, B. Hultqvist, N. Pissarenko, E.M. Dubinin, S.W. Barabash, I. Liede, and H. Koskinen. First Measurements of the Ionospheric Plasma Escape from Mars, *Nature*, **341**, 609-612, 1989.

Lundin, R., A. Zakharov, R. Pellinen, S.W. Barabash, H. Borg, E.M. Dubinin, B. Hultqvist, H. Koskinen, I. Liede, and N. Pissarenko. ASPERA/PHOBOS Measurements of the Ion Outflow from the Martian Ionosphere, *Geophys. Res. Let.*, **17**, 873-876, 1990.

Marubashi, K., J.M. Grebowsky, H.A. Taylor, J.G. Luhmann, C.T. Russell, and A. Barnes. Magnetic Field in the Wake of Venus and the Formation of Ionospheric Holes, *J. Geophys. Res.*, **90**, 1385-1398, 1985.

Mazelle, C., H. Rème, J.A. Sauvaud, C. d'Uston, C.W. Carlson, K.A. Anderson, D.W. Curtis, R.P. Lin, A. Korth, D.A. Mendis, F.M. Neubauer, K.-H. Glassmeier, and J. Raeder. Analysis of Suprathermal Electron Properties at the Magnetic Pile-up Boundary of Comet P/Halley, *Geophys. Res. Let.*, **16**, 9, 1035-1038, 1989.

Mazelle, C., H. Rème, F.M. Neubauer, and K.-H. Glassmeier. Comparison of the Main Magnetic and Plasma Features in the Environments of Comets Grigg-Skjellerup and Halley, *Adv. Space Res.*, **16**, 4, 41-45, 1995.

Michel, F.C. Solar-wind-Induced Mass Loss from Magnetic Field Free Planets, *Plan. Space Sci.*, **19**, 1580, 1971.

Nagy, A.F., J. Kim and T.E. Cravens. Hot Hydrogen and Oxygen in the Upper Atmosphere of Venus and Mars, *Ann. Geophysicae*, **8**, 251, 1990.

National Space Science Data Center (NSSDC). 1998
http://nssdc.gsfc.nasa.gov/planetary/planets/marspage.html

Neubauer, F.M., K.H. Glassmeier, M. Pohl, J. Raeder, M.H. Acuna, L.F. Burlage, N.F. Ness, G. Musmann, F. Mariani, M.K. Wallis, E. Ungstrup, and H.U.

Schmidt. First Results from the Giotto Magnetometer Experiment at Comet Halley, *Nature*, **321**, 352-355, 1986.

Neubauer, F.M. Giotto Magnetic-Field Results on the Boundaries of the Pile-up Region and the Magnetic Cavity, *Astronomy & Astrophysics*, **187**, 73-79, 1987.

Parker, E.N. Dynamics of the Interplanetary Gas and Magnetic Fields, *Astrophysical J.*, **128**, 664-676, 1958.

Pérez-de-Tejeda, H. Momentum Transport in the Solar Wind Erosion of the Mars Ionosphere, *J. Geophys. Res.*, **103**, 31499-31508, 1998.

Pieri, D. Distribution of Small Channels on the Martian Surface, *Icarus*, **27**, 25-50, 1976.

Raeder, J., F.M. Neubauer, N.F. Ness, and L.F. Burlaga. Macroscopic Perturbations of the IMF by P/Halley as Seen by the Giotto Magnetometer, *Astronomy & Astrophysics*, **187**, 61-64, 1987.

Reinhard, R. The Giotto Encounter with Comet Halley, *Nature*, **321**, 313-318, 1986.

Riedler, W., D. Möhlmann, V.N. Oraevsky, K. Schwingenschuh, Ye. Yeroshenko, J. Rutenback, Oe. Aydogar, G. Berghofer, H. Lichtenegger, M. Delva, G. Schelch, K. Pirsch, G. Fremuth, M. Steller, H. Arnold, T. Radisch, U. Auster, K.H. Fornacon, H.J. Schenk, H. Michaelis, U. Motschmann, T. Roatsch, K. Sauer, R. Schröter, J. Kurths, D. Lenners, J. Linthe, V. Kobezev, V. Styashkin, J. Achache, J. Slavin, J.G. Luhmann, and C.T. Russell. Magnetic Field near Mars, *Nature*, **341**, 604-607, 1989.

Rosenbauer, H., N. Shutte, I. Apáthy, A. Galeev, K. Gringauz, H. Grünwaldt, P. Hemmerich, K. Jockers, P. Király, G. Kotova, S. Livi, E. Marsch, A. Richter, W. Riedler, T. Remizov, R. Schwenn, K. Schingenschuh, M. Steller, K. Szegö, M. Verigin, and M. Witte. Ions of Martian Origin and Plasma Sheet in the Martian Magnetosphere: Initial Results of the TAUS Experiment, *Nature,* **341**, 612-614, 1989.

Russell, C.T., J.G. Luhmann, K. Schwingenschuh, W. Riedler, and Ye. Yeroshenko. Upstream Waves at Mars: Phobos Observations, *Geophys. Res. Let.*, **17**, 6, 897-900, 1990.

Sagdeev, R.Z., J. Blamont, A.A. Galeev, V.I. Moroz, V.D. Shapiro, V.I. Shevchenko, and K. Szego. Vega Spacecraft Encounters with Comet Halley, *Nature*, **321**, 259-262, 1986.

Sagdeev, R.Z., V.D. Shapiro, V.I. Shevchenko, A. Zacharov, P. Király, K. Szegö, A.F. Nagy, and R.J.L. Grard. Wave Activity in the Neighborhood of the Bowshock of Mars, *Geophys. Res. Let.*, **17**, 6, 893-896, 1990.

Sauer, K., T. Roatsch, U. Motschmann, K. Schwingenschuh, R. Lundin, H. Rosenbauer, and S. Livi. Observations of Plasma Boundaries and Phenomena around Mars with Phobos 2, *J. Geophys. Res.*, **97**, 6227-6233, 1992.

Sauer, K., A. Bogdanov and K. Baumgärtel. The Protonopause--An Ion Composition Boundary in the Magnetosheath of Comets, Venus and Mars, *Adv. Space Res.*, **16** (4), 153-158, 1995.

Shah, M.B., D.S. Elliott, and H.B. Gilbody. Pulsed Cross-Beam Study of the Ionisation of Atomic Hydrogen by Electron Impact, *J. Physics B*, **20**, 3501-3514, 1987.

Shinagawa, H. and T.E. Cravens. A One Dimensional Multispecies Magnetohydrodynamic Model of the Dayside Ionosphere of Mars, *J. Geophys. Res.*, **94**, 6506-6516, 1989.

Shyn, T.W. Doubly Differential Cross Sections of Secondary Electrons Ejected from Atomic Hydrogen by Electron Impact, *Physical Review A*, **45**, 2951-2956, 1992.

Slavin, J.A., K. Schwingenschuh, W. Riedler, and Ye. Yeroshenko. The Solar Wind Interaction with Mars: Mariner 4, Mars 2, Mars 3, Mars 5, and Phobos 2 Observations of Bow Shock Position and Shape, *J. Geophys. Res.*, **96**, 11235- 11241, 1991.

Smith, E.J. et al. *Science*, **232**, 382-385, 1986.

Snyder, C.W. and V.I. Moroz. Spacecraft Exploration of Mars, *Mars*, Kieffer et al. (eds.), University of Arizona Press: Tucson, 71-119, 1992.

Spreiter, J.R., A.L. Summers, and A.W. Rizzi. Solar Wind Flow Past Nonmagnetic Planets--Venus and Mars, *Plan. Space Sci.*, **18**, 1281-1298, 1970.

Spreiter, J.R. and S.S. Stahara. A New Predictive Model for Determining Solar Wind-Terrestrial Planet Interactions, *J. Geophys. Res.*, **85**, 6769-6777, 1980.

Spreiter, J.R. and S.S. Stahara. Computer Modeling of the Solar Wind Interaction with Venus and Mars, *Venus and Mars: Atmospheres, Ionospheres, and Solar Wind Interactions*, J.G. Luhmann, M. Tatrallyay, and R.O. Pepin, eds. Geophysical Monograph 66, 345, 1992.

Stebbings, R.F., A.C.H. Smith, and H. Ehrhardt. Charge Transfer between Oxygen Atoms and O^+ and H^+ Ions, *J. Geophys. Res.*, **69**, 11, 2349-2355, 1964.

Strangeway, R.J. and C.T. Russell. Plasma Waves and Field-Aligned Currents in the Venus Plasma Mantle, *J. Geophys. Res.*, **101**, 17313-17324, 1996.

Straub, H.C., B.G. Lindsay, K.A. Smith, and R. F. Stebbings. Absolute Partial Cross Sections for Electron-Impact Ionization of CO_2 from Threshold to 1000 eV, *J. Chemical Physics*, **105**, 10, 4015-4022, 1996.

Thompson, W.R., M.B. Shah, and H.B. Gilbody. Single and Double Ionization of Atomic Oxygen by Electron Impact, *J. Physics B: Atomic, Molecular and Optical Physics*, **28**, 1321-1330, 1995.

Travis, J. Mars Observer's Costly Solitude, *Science*, **261**, 1264-1267, 1993.

Trotignon, J.G., E. Dubinin, R. Grard, S. Barabash, and R. Lundin. Martian Planetopause as Seen by the Plasma Wave System onboard Phobos 2, *J. Geophys. Res.*, **101**, 24965-24977, 1996.

Trotignon, J.G., R. Grard, S. Barabash, R. Lundin, and E. Dubinin. Solar Wind Measurements near Mars and their Implication in the Red Planet Environment, *Plan. Space Sci.*, **44**, 2, 117- 127, 1996.

Tsurutani, B.T. Cometary Plasma Waves and Instabilities, *Comets in the Post-Halley Era*, **2**, R.L. Newburn et al., eds. Kluwer Academic Publishers: Netherlands, 1171-1210, 1991.

d'Uston, C. et al. Properties of Plasma in the Cometopause Magnetic Pile-up Region of Comet Halley, *Ann. Geophysicae*, **89**, 01, 91-96, 1989.

Vignes, D., C. Mazelle, H. Rème, M.H. Acuña, J.E.P. Connerney, R.P. Lin, D.L. Mitchell, P. Cloutier, and N.F. Ness. The Solar Wind Interaction with Mars: Locations and Shapes of the Bow Shock and the Magnetic Pile-up Boundary from the Observations of the MAG/ER Experiment Onboard Mars Global Surveyor, in progress, 1999.

Zahnle, K.J. and J.C.G. Walker, The Evolution of Solar Ultraviolet Luminosity, *Reviews of Geophysics and Space Physics*, **20**, 280, 1982.

Zakharov, A.V. The Plasma Environment of Mars: Phobos Mission Results, *Venus and Mars: Atmospheres, Ionospheres, and Solar Wind Interactions*, J.G. Luhmann, M .Tatrallyay, and R.O. Pepin, eds. Geophysical Monograph 66, 327-344, 1992.

Zhang, M.H.G., J.G. Luhmann, S.W. Bougher, and A.F. Nagy. The Ancient Oxygen Exosphere of Mars: Implications for Atmosphere Evolution, *J. Geophys. Res.*, **98**, 10915-10923, 1993.